

Thermodynamic Analysis of Ammonia and Urea fed Solid Oxide Fuel Cells

By

Fadi Ishak

A Thesis Submitted in Partial Fulfillment

of the Requirements for the Degree of

Masters of Applied Science in Mechanical Engineering

in

The Faculty of Engineering and Applied Science

University of Ontario Institute of Technology

April 2011

© Fadi Ishak, 2011

Abstract

This thesis is concerned with the thermodynamic analyses of ion and proton-conducting solid oxide fuel cells (SOFC) fed with ammonia and urea as fuels. A multi-level approach was used to determine the feasibility and the performance of the fuel cells. First, the cell-level thermodynamics were examined to capture the effect of various operating parameters on the cell voltage under open-circuit conditions. Second, electrochemical studies were conducted to characterize the cell-level performance under closed-circuit conditions. Third, the fuel cells were individually integrated in a combined-cycle power generation system and parametric studies were performed to assess the overall performance as well as the thermal and exergy efficiencies.

The findings of this study showed that the overall performance and efficiency of the ammonia fed SOFC is superior in comparison to that of the urea fed counterpart. In particular, the ammonia fed system combined with proton-conducting SOFC achieved a thermal efficiency as high as 85% and exergy efficiency as high as 75%. The respective efficiencies of the ammonia fed system combined with ion-conducting SOFC were lower by 5-10%. However, the urea fed system combined with ion or proton-conducting SOFC demonstrated much lower performance and efficiencies due to higher thermodynamic irreversibilities.

Keywords: Solid oxide fuel cell, ammonia, urea, energy efficiency, exergy efficiency, turbine.

Acknowledgements

“Whatever your hand finds to do, do it with all your might, for in the realm of the dead, where you are going, there is neither working nor planning nor knowledge nor wisdom.” - Ecclesiastes 9:10 NIV

First and foremost, I thank my Lord and Saviour Jesus Christ, through whom all endeavours are fruitful.

I would like to express my deep and sincere gratitude to my supervisor, Dr. Ibrahim Dincer, for his able guidance and support during the course of my research. Special thanks and appreciations go to Dr. Calin Zamfirescu for his valuable assistance and useful suggestions that helped me in completing this work.

I would also like to thank all the members of the examining committee for reviewing my thesis and providing helpful recommendations.

I am very grateful to my parents for their love, encouragement and sacrifices. Without them, none of this would be possible.

Last but not least, I fondly thank my wife, Aseel, for her love, patience and continuous support. It is a true blessing to have her in my life.

Table of Contents

Abstract	ii
Acknowledgements.....	iii
Table of Contents	iv
List of Tables.....	viii
List of Figures.....	x
Chapter One : Introduction	1
1.1 Ammonia and Urea as Hydrogen Carriers.....	2
1.2 Motivation and Objectives	4
Chapter Two : Literature Review	6
2.1 Ammonia-fed Solid Oxide Fuel Cells.....	6
2.1.1 Experimental Investigations.....	6
2.1.2 Theoretical Studies and Modelling.....	11
2.1.2.1 Thermodynamic Analysis and Performance Characterization	11
2.1.3 Evaluation of Integrated Systems	13
2.2 Urea-fed Solid Oxide Fuel Cells.....	14
Chapter Three : Background and Theory	18
3.1 Background of Fuel Cells.....	18
3.2 Types of Fuel Cells	19
3.2.1 Alkaline Fuel Cell (AFC)	20

3.2.2	Proton-Exchange Membrane Fuel Cell (PEMFC).....	20
3.2.3	Phosphoric Acid Fuel Cell (PAFC)	21
3.2.4	Molten Carbonate Fuel Cell (MCFC)	21
3.2.5	Solid Oxide Fuel Cell (SOFC).....	22
3.3	Thermodynamics of Fuel Cells.....	23
3.3.1	Reversible Cell Potential.....	23
3.3.2	Effect of Temperature on the Reversible Cell Potential	25
3.3.3	Effect of Pressure on Reversible Cell Potential.....	26
3.3.4	Effect of Concentration on Reversible Cell Potential.....	27
3.3.5	Thermodynamic Equilibrium of Fuel Cell Reactions.....	28
3.4	Operational Principles of Hydrogen-fed Solid Oxide Fuel Cells.....	29
3.4.1	Oxygen Ion-Conducting Solid Oxide Fuel Cells (SOFC-O)	29
3.4.2	Hydrogen Proton-Conducting Solid Oxide Fuel Cells (SOFC-H).....	31
Chapter Four : System Description.....		32
4.1	Description and Operational Principles of DA-SOFC Cells	32
4.1.1	Oxygen Ion-Conducting DA-SOFC	32
4.1.2	Hydrogen Proton-Conducting DA-SOFC	33
4.2	Description and Operational Principles of DU-SOFC Cells.....	34
4.2.1	Oxygen Ion-Conducting DU-SOFC	34
4.2.2	Hydrogen Proton-Conducting DU-SOFC.....	36

4.3	Description of Integrated SOFC-GT System	36
Chapter Five : Thermodynamic Analysis.....		40
5.1	Cell-level Thermodynamics.....	40
5.1.1	Thermolysis of Ammonia in DA-SOFC.....	40
5.2.1	Thermohydrolysis of Urea in DU-SOFC.....	41
5.1.3	Fuel and Oxidant Utilization.....	42
5.2	Electrochemical Analysis	42
5.2.1	Activation Overpotential	43
5.2.2	Ohmic Overpotential	44
5.2.3	Concentration Overpotential	44
5.3	Maximum Electrochemical Efficiency	48
5.4	Energy and Exergy Analyses of Integrated System.....	48
5.5	Energy and Exergy Analyses of System Components	50
Chapter Six : Results and Discussion.....		59
6.1	Thermodynamic Equilibrium of Ammonia and Urea.....	59
6.2	Reversible Cell Potential (Open Cell Voltage)	63
6.3	Maximum Electrochemical Efficiency	73
6.4	Operational Voltage and Performance.....	74
6.4.1	Model Validation.....	74
6.4.2	Ion and Proton-Conducting DA-SOFC.....	77

6.4.3	Ion and Proton-Conducting DU-SOFC.....	83
6.5	Integrated Systems.....	89
6.5.1	Ammonia-fed SOFC/GT system.....	89
6.5.2	Urea-fed SOFC/GT system.....	104
Chapter Seven : Conclusions and Recommendations.....		121
7.1	Conclusions.....	121
7.2	Recommendations.....	122
References.....		123

List of Tables

Table 1.1: Energy density of different energy carriers.	3
Table 2.1: Composition of the anode outlet gases of SOFC-O cell fuelled with ammonia.....	8
Table 2.2: Comparison of standard cell potential for the direct oxidation of ammonia and hydrogen.	9
Table 3.1: Summary of the main features of different types of fuel cells.....	19
Table 6.1: Parameters used in the validation of ion-conducting DA-SOFC.....	75
Table 6.2: Parameters used in modelling the polarization curve of DA-SOFC.....	77
Table 6.3: Parameters used in modelling the polarization curve of DU-SOFC.....	83
Table 6.4: Main parameters used for the base case study of DA-SOFC/GT system..	89
Table 6.5: Operating voltage and current density of DA-SOFC/GT system at different conditions.	91
Table 6.6: Specific power and exergy destruction in kJ/mol of fuel for DA-SOFC/GT system (base case).	93
Table 6.7: Energy and exergy efficiency of DA-SOFC/GT system (base case).....	95
Table 6.8: Effect of pressure ratio on the cooling performance of ammonia in DA-SOFC/GT system.	103
Table 6.9: Main parameters used for the base case study of DU-SOFC/GT system.	105
Table 6.10: Operating voltage and current density of DU-SOFC/GT system at different conditions.	107

Table 6.11: Specific power and exergy destruction in kJ/mol of fuel for DU-SOFC/GT system (base case).	111
Table 6.12: Energy and exergy efficiency of DA-SOFC/GT system (base case).....	111

List of Figures

Figure 3.1: Types of fuel cells (modified from [56]).	19
Figure 3.2: General configuration of solid oxide fuel cells.	22
Figure 3.3: The reversible fuel cell.	24
Figure 3.4: Hydrogen-fed Oxygen Ion-Conducting Solid Oxide Fuel Cell (SOFC-O).	30
Figure 3.5: Hydrogen-fed Proton-Conducting Solid Oxide Fuel Cell (SOFC-H).	31
Figure 4.1: Schematic representation of ion-conducting direct ammonia solid oxide fuel cell.	32
Figure 4.2: Schematic representation of proton-conducting direct ammonia solid oxide fuel cell.	33
Figure 4.3: Schematic representation of oxygen ion-conducting direct urea solid oxide fuel cell.	35
Figure 4.4: Schematic representation of hydrogen proton-conducting direct urea solid oxide fuel cell.	36
Figure 4.5: Schematic of integrated DA-SOFC/GT system.	37
Figure 4.6: Schematic of integrated DU-SOFC/GT system.	39
Figure 5.1: Thermodynamic processes of fuel cell stack.	51
Figure 6.1: Thermodynamic equilibrium of ammonia.	59
Figure 6.2: Conversion of ammonia as a function of reaction temperature.	60
Figure 6.3: Thermodynamic equilibrium of urea (SUR=1).	61
Figure 6.4: Thermodynamic equilibrium of urea (Pressure=101 kPa).	62
Figure 6.5: Molar fraction of hydrogen in DA-SOFC.	63
Figure 6.6: Molar fraction of hydrogen in DU-SOFC.	64

Figure 6.7: Molar fraction of water vapour in DA-SOFC.....	65
Figure 6.8: Molar fraction of water vapour in DU-SOFC.....	65
Figure 6.9: Open cell voltage of DA-SOFC at different temperatures.....	66
Figure 6.10: Comparison of predicted open cell voltage with experimental data (SOFC-O).....	67
Figure 6.11: Open cell voltage of DU-SOFC at different temperatures.....	68
Figure 6.12: Effect of pressure on the open cell voltage of DA-SOFC.....	69
Figure 6.13: Effect of pressure on the open cell voltage of DU-SOFC.....	69
Figure 6.14: Effect of oxidant (air) utilization on the open cell voltage of DA-SOFC.....	70
Figure 6.15: Effect of oxidant (air) utilization on the open cell voltage of DU-SOFC.	70
Figure 6.16: Effect of SUR on the open cell voltage of proton-conducting DU-SOFC.	71
Figure 6.17: Effect of SUR on the open cell voltage of ion-conducting DU-SOFC.....	72
Figure 6.18: Maximum electrochemical efficiency of DA-SOFC.....	73
Figure 6.19: Maximum electrochemical efficiency of DU-SOFC.....	74
Figure 6.20: Comparison of simulation and experimental results of ammonia-fed SOFC-O.....	76
Figure 6.21: Polarization curve of DA-SOFC at 1073K and atmospheric pressure...	78
Figure 6.22: Activation overpotential of anode-supported DA-SOFC.....	79
Figure 6.23: Ohmic overpotential of anode-supported DA-SOFC.....	80
Figure 6.24: Concentration overpotential of anode-supported DA-SOFC.....	81
Figure 6.25: Polarization curve of DA-SOFC at 1273K and atmospheric pressure...	81

Figure 6.26: Polarization curve of DA-SOFC at 1073K and pressure of 505 kPa.....	82
Figure 6.27: Polarization curve of DU-SOFC at 1073K and atmospheric pressure...	84
Figure 6.28: Activation overpotential of anode-supported DU-SOFC.....	85
Figure 6.29: Ohmic overpotential of anode-supported DU-SOFC.....	85
Figure 6.30: Concentration overpotential of anode-supported DU-SOFC.....	86
Figure 6.31: Polarization curve of DU-SOFC at 1273K and atmospheric pressure...	87
Figure 6.32: Polarization curve of DU-SOFC at 1073K and pressure of 505 kPa.....	88
Figure 6.33: Polarization curve of ion and proton-conducting DA-SOFC (base case).	90
Figure 6.34: Temperature distribution of ion and proton-conducting DA-SOFC/GT system (base case).	91
Figure 6.35: The distribution of exergy destruction of DA-SOFC/GT system by component (base case).....	94
Figure 6.36: Effect of reference temperature on the exergy efficiency of DA- SOFC/GT system (base case).....	96
Figure 6.37: Effect of ammonia utilization on the total specific power and back work ratio.....	97
Figure 6.38: Effect of ammonia utilization on the efficiency of the system.	98
Figure 6.39: Effect of the fuel cell temperature on the total specific power and back work ratio.	99
Figure 6.40: Effect of fuel cell temperature on the efficiency of the system.....	100
Figure 6.41: Effect of pressure ratio on the total specific power and back work ratio.	101

Figure 6.42: Effect of pressure ratio on the efficiency of the system.	102
Figure 6.43: Polarization curve of ion-conducting DU-SOFC (base case).....	105
Figure 6.44: Polarization curve of proton-conducting DU-SOFC (base case).	106
Figure 6.45: Temperature distribution of ion-conducting DU-SOFC/GT system (base case).....	107
Figure 6.46: Exergy destruction of ion-conducting DU-SOFC/GT system by component (base case).....	108
Figure 6.47: Temperature distribution of proton-conducting DU-SOFC/GT system (base case).....	109
Figure 6.48: Exergy destruction of proton-conducting DU-SOFC/GT system by component (base case).....	110
Figure 6.49: Effect of reference temperature on the exergy efficiency of DU-SOFC/GT system (base case).....	112
Figure 6.50: Effect of urea utilization on the specific power and back work ratio of ion-conducting DU-SOFC/GT system.....	113
Figure 6.51: Effect of urea utilization on the efficiency of ion-conducting DU-SOFC/GT system.	114
Figure 6.52: Effect of the fuel cell temperature on the total specific power and back work ratio of ion-conducting DU-SOFC/GT system.	115
Figure 6.53: Effect of the fuel cell temperature on the efficiency of ion-conducting DU-SOFC/GT system.....	115
Figure 6.54: Effect of pressure ratio on the total specific power and back work ratio of ion-conducting DU-SOFC/GT system.....	117

Figure 6.55: Effect of pressure ratio on the efficiency of ion-conducting DU-SOFC/GT system.	117
Figure 6.56: Effect of pressure ratio on the total specific power and back work ratio of proton-conducting DU-SOFC/GT system.	118
Figure 6.57: of pressure ratio on the efficiency of proton-conducting DU-SOFC/GT system.	119

Nomenclature

A	Area [m ²]
B ₀	Permeability [m ²]
c	Charge [Coulomb/mol]
\bar{c}_p	Specific molar heat capacity [J/mol.K]
dx	Depth of electrode layer [m]
D^{eff}	Effective binary diffusion [m ² /s]
D_k^{eff}	Effective Knudsen diffusion [m ² /s]
D _p	Difference between T _p and T _{sat} [K]
\bar{e}_x	Molar specific exergy [J/mol]
E	Reversible cell potential or voltage [V]
E ⁰	Standard cell potential or voltage [V]
\dot{E}_x	Exergy rate [W]
\dot{E}_{x_D}	Exergy destruction rate [W]
f	Fugacity of chemical species in system
f ⁰	Fugacity of chemical species at STP
F	Faraday's constant (96485 Coulombs/mol)
\bar{g}	Specific molar Gibbs energy [J/mol]
G	Gibbs energy [J]
\bar{g}^0	Specific molar Gibbs energy at STP [J/mol]
\bar{h}	Specific molar enthalpy [J/mol]
H	Enthalpy [J]
H ⁰	Standard Enthalpy at STP [J]
H _c	Heat capacity rate [W/K]
J	Current density [A/m ²]
J ₀	Exchange current density [A/m ²]
k	Ratio of specific molar heat
M	Molar mass [g/mol]
n	Number of moles [mol]
\dot{n}	Molar flow rate [mol/s]

N	Molar flux [mol/m ² .s]
p	Partial pressure [kPa]
P	Pressure, total pressure [kPa]
Q	Heat [J]
\dot{Q}	Rate of heat transfer [W]
r_p	Mean pore radius of electrode [m]
\bar{R}	Gas constant [J/mol.K]
R_Ω	Electrolyte resistivity [Ω .m]
\bar{s}	Molar specific entropy [J/mol.K]
S	Entropy [J/K]
T	Temperature [K]
U_f	Fuel utilization
U_o	Oxidant utilization
v	Specific molar volume [m ³ /mol]
V	Working potential or voltage [V]
W	Work [J]
\dot{W}	Work rate, power [W]
x	Molar ratio of produced hydrogen to consumed fuel
y	Molar fraction of chemical species
z	Number of electrons transferred per mole of fuel

Greek Letters

α	Charge transfer coefficient
Γ	Dimensionless temperature
δ	Electrolyte thickness [m]
Δ	Net change of quantity
ϵ	Porosity of electrode
ϵ/κ	Lennard-Jones temperature parameter [K]

η	Energy or thermal efficiency
μ	Viscosity [Pa.s]
ξ	Heat exchanger effectiveness
σ	Molecular collision diameter [\AA]
τ	Tortuosity of electrode
$\varphi_{\text{act,an}}$	Anode activation overpotential [V]
$\varphi_{\text{act,ca}}$	Cathode activation overpotential [V]
$\varphi_{\text{conc,an}}$	Anode concentration overpotential [V]
$\varphi_{\text{conc,ca}}$	Cathode concentration overpotential [V]
φ_{Ω}	Ohmic overpotential of electrolyte [V]
ψ	Exergy efficiency
Ω_D	Collision integral of diffusion

Subscripts

AC	Alternating current
amb	Ambient
aq	Aqueous urea
c	Cold
ch	Chemical
C	Compressor
CC	Combustion chamber
CL	Cooling load
cmp	Component
DC	Direct current
e	Electrical
eco	Economizer
elc	Electrochemical
evp	Evaporator
exh	Exhaust
f	Fuel

fg	Evaporation
FC	Fuel cell
G	Generator
h	Hot
hyd	Hydrolysis
HX	Heat exchanger
<i>i</i>	Chemical species
in	Inlet
INV	Inverter
<i>j</i>	Chemical species
max	Maximum
MC	Mixing chamber
min	Minimum
mix	Mixture
o	Oxidant
out	Outlet
p	Pinch
ph	physical
Q	Heat
r	Reactants
rev	Reversible
REC	Recovery, Recuperator
s	Isentropic
sat	Saturation
soln	Solution
T	Turbine

List of Acronyms and Definitions

BCGO	Barium Cerate Gadolinium Oxide
BCNO	Barium Cerate Neodymium Oxide
BCSm	Barium Cerate Samarium Oxide
BSCF	Barium Strontium Cobalt Ferrite
BSCF-CGO	Barium Strontium Cobalt Ferrite-Ceria Gadolinium Oxide
DA-SOFC	Direct Ammonia Solid Oxide Fuel Cell
DeNOx	Destruction of Nitrous Oxides
DGM	Dusty Gas Model
DU-SOFC	Direct Urea Solid Oxide Fuel Cell
EES	Engineering Equation Solver
GEM	Gibbs Energy Minimization
LHV	Lower Heating Value
LSCO-BCNO	Lanthanum Strontium Cobalt Oxide-Barium Cerate Neodymium Oxide
LSM	Lanthanum Strontium Manganite
MATLAB	Matrix Laboratory
Ni-CGO	Nickel-Ceria Gadolinium Oxide
NiO-BCNO	Nickel Oxide-Barium Cerate Neodymium Oxide
Ni-YSZ	Nickel-Yittria stabilized Zirconia
OCV	Open Cell Voltage
RWGS	Reverse Water-Gas Shift Reaction
SCR	Selective Catalytic Reduction
SDC	Samaria-doped Ceria
SNCR	Selective Non-Catalytic Reduction
SOFC-H	Solid oxide fuel cell with Hydrogen proton (H^+) conducting electrolyte
SOFC-O	Solid oxide fuel cell with Oxygen ion (O^{2-}) conducting electrolyte
STP	Standard temperature of 298K and pressure of 101.325 kPa

SUR	Steam-to-Urea Ratio
TPB	Triple-Phase Boundary
YSZ	Yttria-stabilized Zirconia

Chapter One : Introduction

Trade market fluctuations and periodic economic cycles like the recent global economic recession of 2008 have a significant near-term impact on the world energy demand. From a long-term perspective, there is no doubt that the continuous growth of the world population presents great challenges to energy resources and development. Therefore, it is evident that there is an ever growing need for sustainable and environmentally-benign energy supply as well as efficient power production and distribution.

Fuel cells have been identified as a promising technology of power production for stationary and mobile applications due to their high efficiency and small environmental footprint. As such, substantial research and development efforts are invested in advancing this technology. In particular, Solid oxide fuel cells remain at the forefront of this focus due to several advantages like the capability of directly operating on renewable and non-renewable energy carriers and fuels.

As the reserve of non-renewable resources depletes over time, hydrogen is expected to emerge and attain a major market share as a renewable energy carrier. The shift of energy paradigm initiated by the new hydrogen economy is expected to have dramatic impact on the environmental and economic sustainability of societies around the world. However, this progress is hindered by technical and economic challenges that must be overcome before the transition is realized. To that extent,

research communities have started investigating the use of suitable intermediate hydrogen carriers in effort to eliminate these challenges and shortcomings.

1.1 Ammonia and Urea as Hydrogen Carriers

The task of identifying the optimal hydrogen carrier is not trivial as it involves multi-criteria decision making and consideration of various technical and economical aspects like safety, energy density and cost of processing or recycling. This has led to the careful scrutiny of diverse spectrum of storage materials like metal hydrides, metal-organic framework and amide systems [1]. Despite extensive research and development efforts, these materials and compounds have major drawbacks revolving around the rate of hydrogen desorption, cyclability and high cost [2,3].

With this respect, ammonia has been regarded as an excellent hydrogen carrier for its several favourable attributes as shown in Table 1.1. Large quantities of ammonia are used worldwide for agricultural purposes. It is estimated that the global capacity of ammonia was about 153 million tonnes in 2009 [4]. The infrastructure and technology of ammonia production are also well established with existing industrial plants around the world to support the increasing demand for fertilizers [4,5]. Natural gas is the main feedstock for the synthesis of ammonia which using the steam reforming method. So from a life-cycle perspective, the production of one tonne of ammonia emits about 1.7 tonnes of carbon dioxide most of which can be easily recovered for use in downstream processes such as the production of urea or

other derivatives [6]. This figure excludes the potential amount of carbon dioxide emitted if carbon-based fuel is used to provide the energy required to drive the process of ammonia production.

Table 1.1: Energy density of different energy carriers.

Energy Carrier	Density (kg/m³)	Gravimetric Density (%H₂)	Volumetric Density (kgH₂/L)	Energy Density (MJ/L)
Gaseous H₂ (298K, 10MPa)	7.68	100	0.0077	0.92
Liquid H₂ (30K, 10MPa)	72.58	100	0.0726	8.71
Liquid NH₃ (298K, 1MPa)	603	17.76	0.1071	12.85
Aqueous Urea (76.92%wt-STP)	1200	7.74	0.0930	11.16

Sources: [7,8,9]. Energy density is based on LHV of hydrogen.

On the other hand, ammonia is corrosive, toxic and life-threatening when released at high concentrations [10]. To mitigate these risks, some focus has been directed towards stabilizing the ammonia by combining it in metal ammine complexes or ammonia-borane systems. This allows for the transportation and long-term storage of fuel in solid-state or liquid form and provides the means by which hydrogen can be released on demand [11]. However, such systems are also burdened with disadvantages like to those discussed earlier. Alternatively, urea is a non-toxic chemical which can be found in natural systems as well as human and animal waste (urine). On average, the concentration of urea in human urine is 9.3-23.3 g/L [12]. Pure urea is formed as white, odourless prills or granules when artificially synthesized. Owing to its stable nature, it can be easily and safely handled,

transported and stored at room temperature. Also, urea is the most widely used solid fertilizer worldwide. In 2009, the worldwide production of urea reached 146 million tonnes and it is anticipated to increase to 210 million tonnes by 2013 due to increasing global demand. This major increase is, in part, due to the growth of non-agricultural use of urea in emission control (DeNOx) systems for industrial and automotive applications [13].

As stated earlier, the process of ammonia production normally supplies the feedstock of ammonia and carbon dioxide for the synthesis of urea. Therefore, greenhouse gas is released only when fossil fuel is utilized to provide the required energy for this process. Finally, the processes of ammonia and urea production can be combined with clean hydrogen production methods like the Cu-Cl thermochemical cycle for the future development of carbon-neutral energy carriers.

1.2 Motivation and Objectives

This study is motivated by the technical challenges to the rapid development of hydrogen markets and infrastructure including the constraints of safe transportation, low temperature storage as well as the high pressure necessary to achieve the required energy density. In that aspect, storing the hydrogen molecules in liquid ammonia or solid urea can potentially eliminate the need for complex and perilous storage systems. The specific objectives of this study are:

1. Examine the operating principles of ammonia and urea-fed solid oxide fuel cells

2. Determine the thermodynamic equilibrium of the thermolysis of ammonia and thermohydrolysis of urea
3. Investigate the cell-level thermodynamic performance at open-circuit conditions
4. Characterize the cell-level electrochemical performance at closed-circuit conditions
5. Study the system-level thermodynamic performance by integrating the prescribed fuel cells with a gas-power cycle and perform parametric studies to identify the sources of energy and exergy losses

Chapter Two : Literature Review

2.1 Ammonia-fed Solid Oxide Fuel Cells

2.1.1 Experimental Investigations

Following the attempts of Vayenas et al. [14,15] to use ammonia in a solid electrolyte reactor to produce electricity and nitrogen monoxide as a useful chemical feedstock, Wojcik et al. [16] conducted an experiment to determine the viability of using ammonia as a source of hydrogen for SOFC operation. The experiment apparatus was comprised of tubular SOFC-O using YSZ electrolyte, silver and platinum electrodes along with iron catalyst for the decomposition of ammonia. The tests were performed at temperatures of 700-1000 °C. It was theoretically assumed that the anodic reaction proceeded as follows:



and the cathodic reaction of oxygen becomes



resulting in the direct oxidation reaction of ammonia:



They also suggested the possibility that nitrogen monoxide could be formed due to the following side reaction:



Nonetheless, no experimental validation has been carried out. They indicated that while platinum was more effective than silver as an electrode material, it is not feasible for commercial applications due to its higher cost. They also added that SOFC-O fuelled with ammonia offers comparable performance to that fuelled with hydrogen especially at higher temperatures.

A later study by Ma et al. [17] suggested the same oxidation reaction mechanism (direct oxidation of ammonia) as well as the likelihood of nitrogen monoxide formation due to the competition of nitrogen and hydrogen for the reaction with oxygen ions particularly at higher temperatures such that



In order to verify their theoretical predictions, they constructed an ion-conducting solid oxide fuel cell based on Ni-Ce_{1.8}Sm_{0.2}O_{1.9} (Ni-SDC) anode, SDC electrolyte and Sm_{0.5}Sr_{0.5}CoO_{3-δ} (SSC-SDC) cathode and used hydrogen and ammonia as fuels. It was found that the operating voltage of the ammonia-fed SOFC-O was very close to that fuelled with hydrogen whereas the maximum power density obtained was 271.2 and 252.8 mW/cm² at 700 °C for hydrogen and ammonia fuel respectively. Additionally, the gas composition at the anode outlet was measured at different temperatures and ammonia flow rates using gas chromatography to determine the concentration of nitrogen monoxide and unconverted ammonia. The results shown in Table 2.1 indicate that the concentration of ammonia was negligible (<1 ppm) while nitrogen oxide was not detectable at temperatures higher than 600 °C. A 50-

hour durability test was also conducted and demonstrated the stability of the anode materials in ammonia environment.

Table 2.1: Composition of the anode outlet gases of SOFC-O cell fuelled with ammonia.

Operating Temperature (°C)	Flow Rate (ml/min)	H₂ (%)	N₂ (%)	NH₃ (%)	NO (%)
500	30	51	28	21	Not detectable
	5	28	67	5	Not detectable
600	30	57	43	<1	Not detectable
	5	8	92	<1	Not detectable
700	30	55	45	<1	Not detectable
	5	8	92	<1 ppm	Not detectable

Source: [17].

Ma et al. [18] attributed the low performance of the fuel cell in the previous study to the poor material preparation and cell structure such as thick SDC electrolyte (50µm) and low catalytic activity of the cathode materials.

Fuerte et al. [19] carried out an experimental investigation to compare between the ammonia and hydrogen as suitable fuels for SOFC-O cells. They employed a commercial micro-tubular SOFC consisting of a Ni-YSZ anode, YSZ electrolyte and LSM-YSZ cathode. The OCV of the fuel cell running on ammonia was lower than running on hydrogen on the same temperature. Furthermore, the OCV of both cells showed a decreasing trend as the operating temperature increased. This is; however, different from the thermodynamic data of the direct oxidation of ammonia which suggest that the standard cell potential should increase as the temperature increases (see Table 2.2).

Table 2.2: Comparison of standard cell potential for the direct oxidation of ammonia and hydrogen.

Reaction	E°_{25°C} (V)	E°_{850°C} (V)
$2NH_3 + \frac{3}{2}O_2 \rightarrow N_2 + 3H_2O$	1.13	1.33
$H_2 + \frac{1}{2}O_2 \rightarrow H_2O$	1.19	0.93

Source: [19].

As such, it was concluded that the operation of ammonia-fed SOFC entails a two-stage process whereby the ammonia is first decomposed to nitrogen and hydrogen followed by the direct oxidation of hydrogen. This may be attributed to the fast rate of ammonia decomposition reaction in comparison to the rate of direct oxidation reaction of ammonia. This premise was also supported by the work of Ma et al. [8] who arrived at the same conclusion.

Few other studies were performed to investigate the possibility of using ammonia as a direct fuel in SOFC-H. Zhang and Yang [20] fabricated an anode-supported SOFC-H based on Ni-CGO|BCGO|BSCF-CGO arrangement using dry-pressing method and applied humidified hydrogen and ammonia as fuels. The peak power density obtained was 223 and 200 mW/cm² at 650 °C for hydrogen and ammonia, respectively. The difference between the two values was mainly due to the lower hydrogen partial pressure at the anode as a result of the ammonia decomposition to hydrogen and nitrogen. The OCV of the ammonia fuel cell decreased with increasing temperature and exhibited similar behaviour to that of the hydrogen fuel cell. As

such, it was concluded that only hydrogen produced from the decomposition process of ammonia was involved in the electrochemical reaction of the cell.

Xie et al. [21] were able to obtain higher performance by constructing an anode-supported cell based on NiO-BCNO anode, BCNO electrolyte and LSCO-BCNO cathode. The power density was 335 and 315 mW/cm² at 700 °C for the hydrogen and ammonia fuel respectively. The polarization curve was nearly linear which implied low activation losses. They concluded that the reasonable performance attained was due to the suitability of the materials used and the uniformity of the structure of the cell except for the dense anode layer (650µm). However, the performance could be improved further by increasing the porosity of the anode layer to allow for the complete reduction of the NiO to Ni metal.

More recently, Lin et al. [22] reported the successful use of ammonia as a fuel for anode-supported SOFC-H based on Ni-BZCY anode, BZCY electrolyte and BSCF cathode. The peak power density was 465 and 390 mW/cm² at 750 °C when hydrogen and ammonia were respectively supplied to the cell. The electrochemical reaction of the fuel cell was also investigated and it was determined that the ammonia was first decomposed to nitrogen and hydrogen while only the latter participated in the fuel cell reaction. Moreover, the ammonia-fed fuel cell experienced a drop of 30-65 °C in operating temperature due to the endothermic nature of the ammonia decomposition reaction.

2.1.2 Theoretical Studies and Modelling

2.1.2.1 Thermodynamic Analysis and Performance Characterization

An extensive literature survey returned a study conducted by Ni et al. [23] who compared the thermodynamic performance of SOFC-O and SOFC-H operating under temperatures between 873K and 1273K. The study also assumed an indirect reaction mechanism whereby ammonia was first decomposed to nitrogen and hydrogen while the latter was oxidized to produce electrical power. The stoichiometric method was used to determine the ammonia decomposition at a given temperature [24,25]. Comparing the OCV of both fuel cell types over a wide range of fuel and oxidant utilizations signified the superiority of SOFC-H over SOFC-O mainly due to the higher partial pressure of hydrogen at the SOFC-H anode. The maximum theoretical (electrochemical) efficiency was found to increase with the increase of fuel utilization which is consistent with thermodynamic studies on the hydrogen-fed SOFC given by Demin and Tsiakaras [26].

Furthermore, Ni et al. [27] used an electrochemical macro-model to compare the operating voltage and power density of ammonia-fed SOFC-O and SOFC-H at a temperature of 1073K and atmospheric pressure only. The anode supported fuel cells were based on YSZ and BCSm electrolytes for SOFC-O and SOFC-H, respectively. The analysis assumed a leak-free construction, negligible interfacial resistance and no fuel cross-over or electronic conductivity through the electrolyte layer. Thus, only the most significant types of overpotentials, namely activation, ohmic and concentration, were addressed. The Butler-Volmer equation was used to describe

the activation overpotential while Ohm's law was used to represent the ohmic losses through electrolyte since the resistance of the electrodes was negligible. Moreover, DGM and equimolar gas flux conditions were employed to describe the effects of diffusion and permeation on the concentration overpotential of the fuel cells. The main finding of their work is the higher performance of SOFC-O over SOFC-H. This was explained by the high ohmic overpotential of BCSm electrolyte and the high concentration overpotential at the SOFC-H cathode as the water vapour formation obstructed the oxygen transport to the reaction sites. The results were quite different from those presented by Assabumrungrat et al. [28] and Biesheuvel et al. [29] which advocated the superior performance of SOFC-H over that of the SOFC-O using methanol or methane fuel at the same operating conditions.

With the focus on SOFC-H, another study was conducted by Ni et al. [30] to examine the difference between the electrolyte-supported and anode-supported cell arrangement and the corresponding impact on performance. It was found that higher power density can be achieved by the anode-supported cell primarily because of the thinner electrolyte material which greatly reduced the ohmic polarization. Later, their electrochemical model was improved [31] by incorporating a first-order model of the kinetic rate of ammonia decomposition which was previously developed by Chellappa et al. [32]. The kinetic model was coupled with DGM to obtain the molar fraction of ammonia across the anode thickness at various temperatures. The model showed that the ammonia was fully decomposed at an approximate anode depth of 25 μ m and 300 μ m at 1073K and 873K, respectively. However, the ammonia may not fully decompose at

temperatures below 873K resulting in a lower partial pressure of hydrogen at the anode-electrolyte interface leading to deteriorated performance of the fuel cell.

2.1.3 Evaluation of Integrated Systems

Extensive research and development is underway to integrate fuel cell stacks with other thermal and thermomechanical cycles to reap the benefits of higher synergistic efficiency. Because of their fuel flexibility and wide range of operating temperature, solid oxide fuel cells are highly suitable for integration with a wide variety of system or bottoming cycles. There are no reports in the open literature of any theoretical investigation or experimental demonstration related to the integration strategies of ammonia-fed SOFC. Nonetheless, a recent review by Zhang et al. [33] presented many schemes for coupling pressurized or naturally-aspirated SOFC stacks fuelled with hydrogen or carbon-based fuels with other power and thermal cycles depending on the application of use. An interesting hybrid system is a result of the combination of SOFC and absorption refrigeration cycle for the simultaneous delivery of power, heating and cooling. However, the main setbacks of such system include large volume and high cost due to large number of components.

SOFC-GT systems are of particular importance for power generation applications as they have demonstrated high efficiency and reliability based on continuous steady-state operation. For example, Zamfirescu and Dincer [34] proposed a hydrogen-fed integrated SOFC-GT system for vehicular applications. The performance of the system was assessed based on the optimization objective of maximum efficiency or

maximum power density. Furthermore, an exergy analysis was carried out to outline the major sources of exergy destruction in the system. They found that the fuel cell stack can occupy about 75% of the total system volume and reduce the compactness of the system by 40% when the maximum system efficiency is achieved. They also concluded that the largest exergy destruction occurred at the fuel cell stack and accounted for 60% of the total exergy destruction in the system. Finally, another study by Dincer et al. [35] focused on the exergy analysis of an elaborate SOFC-GT system fuelled with methane. The study highlighted the positive impact of higher operating voltage on the thermal and exergy efficiency of the system. It was also identified that the highest thermodynamic irreversibilities emerged from the electrochemical oxidation and combustion processes. In essence, the exergy destruction in the fuel cell stack accounted for 37.1% while the combustion chamber accounted for 34.8% of the total exergy destruction in the system.

2.2 Urea-fed Solid Oxide Fuel Cells

There are very few studies on the use of urea in power and energy-related applications. For instance, Botte et al. [36,37] conducted experimental investigations on the electrolysis of urea for the purpose of hydrogen production. The findings suggested that hydrogen production by the electrolysis of urea requires 30% less energy than the electrolysis of water. On the other hand, there has been a widespread interest in utilizing urea instead of ammonia in SCR, SNCR

and DeNO_x applications to eliminate the drawbacks associated with the toxicity and handling of ammonia. Koebel et al. [38,39] proposed that urea can be delivered from a storage medium to the reaction site as solid granules or in aqueous form. When solid urea is heated at STP conditions, it melts at a temperature near 133 °C and subsequently decomposes to gaseous ammonia and isocyanic acid. In their study, Hauck et al. [40] indicated that isocyanic acid is stable in the gaseous phase but it can be easily and rapidly hydrolyzed over a suitable catalyst like titanium oxide anatase to yield ammonia and carbon dioxide. However, some experimental studies like the one conducted by Lundstrom et al. [41] showed that the mechanism of urea thermolysis is highly dependent on the conditions under which the experiments are carried out. Consequently, careful control of the thermolysis process and its condition is essential for avoiding the formation of intermediate compounds with high molecular weight.

In addition, the direct use of solid urea is more problematic in practical applications as it may require special and bulky equipments for delivery as suggested by Gentemann and Caton [42]. For these reasons, several investigations as presented by Yim et al. [43] and Birkhold et al. [44] have focused on the delivery of aqueous urea to DeNO_x systems by spraying or injection. Their works showed that heating the mixture during spraying or injection results in a momentary conversion of urea from aqueous to solid state through the evaporation of water from the spray droplets. Solid urea is then decomposed by thermolysis into ammonia and isocyanic acid while the water vapour is used for the simultaneous hydrolysis process. The final reaction is similar to the direct hydrolysis of solid urea. Subsequently, the

ammonia reacts with the nitrous oxides in the exhaust stream to neutralize their harmful effects by producing nitrogen gas and water vapour.

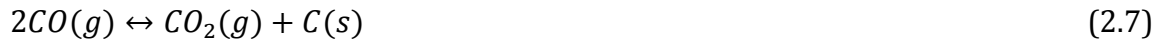
Alternatively, the process of thermohydrolysis of urea can be directly combined with SOFC in a novel system to benefit from the high operating temperature in a fashion similar to that applied for the internal reforming of methane fuel. When this is done, the generated ammonia is thermally decomposed over a catalyst like nickel to inert nitrogen and hydrogen which can be electrochemically oxidized in the fuel cell to produce electric power. As such, different chemical species like hydrogen and carbon dioxide are simultaneously present in the anode side of the fuel cell which may lead to competing side reactions like the RWGS reaction [45]



that dilutes the concentration of hydrogen with carbon monoxide and water vapour. Although carbon monoxide can also be electrochemically oxidized in SOFC-O to produce electricity, it has a higher overpotentials than that of the hydrogen as discussed by Singhal and Kendall [46]. There are some ambiguities and disagreements on the ratio of hydrogen to carbon monoxide oxidation rates. Matsuzaki and Yasuda [47] experimentally found that the ratio is 1.9-2.3 at 1023K and 2.3-3.1 at 1273K which is consistent with the model developed by Suwanwarangkul et al. [48] while Bessette et al. [49] assumed a ratio of 3:1 in their mathematical model. Nonetheless, other researchers like Haberman and Young [50] and Ni et al. [51] have completely ignored the electrochemical oxidation of carbon monoxide. Karcz [52] have shown that introducing carbon monoxide as a fuel along

with hydrogen can reduce the cell voltage by 0.03-0.05 V when operating under a range of current density equal to 1800-3000 A/m² due to the competition of the fuels for the reaction sites. Moreover, the experimental and numerical study performed by Anderassi et al. [53] demonstrated that an error of about 3-4% (based on power) is introduced when the electrochemical oxidation of carbon monoxide is ignored.

Furthermore, other complications and detrimental side reactions can also develop under certain conditions such as carbon deposition (coking) on the surface of the anode due to the Boudouard or the carbon monoxide reduction reactions [46,54,55]:



In light of the foregoing discussion, the electrochemical oxidation of carbon monoxide will not be considered. Furthermore, a performance assessment of urea-fed SOFC can be carried out by taking an approach similar to that used for the ammonia-fed SOFC.

Chapter Three : Background and Theory

3.1 Background of Fuel Cells

Fuel cells are energy conversion devices capable of transforming the chemical energy of the fuel to electrical energy directly through electrochemical reaction. The direct energy conversion path eliminates the need for intermediate thermodynamic processes and results in higher conversion efficiency in comparison to conventional electric power generation systems. Such devices also have a low environmental impact due to the absence of fuel combustion processes and the associated harmful products. The basic building block of a fuel cell is comprised of an assembly of a positive electrode (anode), an electrolyte and a negative electrode (cathode). The fuel cell produces useful power through a redox reaction between a suitable type of fuel such as hydrogen and an oxidant such as oxygen. While hydrogen fuel is oxidized at the anode, the electrolyte acts as electronic insulator and ionic conductor forcing the electrons to flow to an external circuit and return to the cathode. The type of ion (anion or cation) transported between the anode and the cathode is dictated by the type of electrolyte used. For this reason, the fuel cell is normally classified by the electrolyte used or the type of ion transported. The overall reaction of the hydrogen fuel cell is



Electricity is the desired product while heat is generated due to irreversibilities and losses associated with the operation of the fuel cell.

3.2 Types of Fuel Cells

Many types of fuel cells have been proposed since the first invention in the early 19th century. Those depicted in the figure and summarized in the table below have survived the scientific and technical scrutiny and will be discussed next.

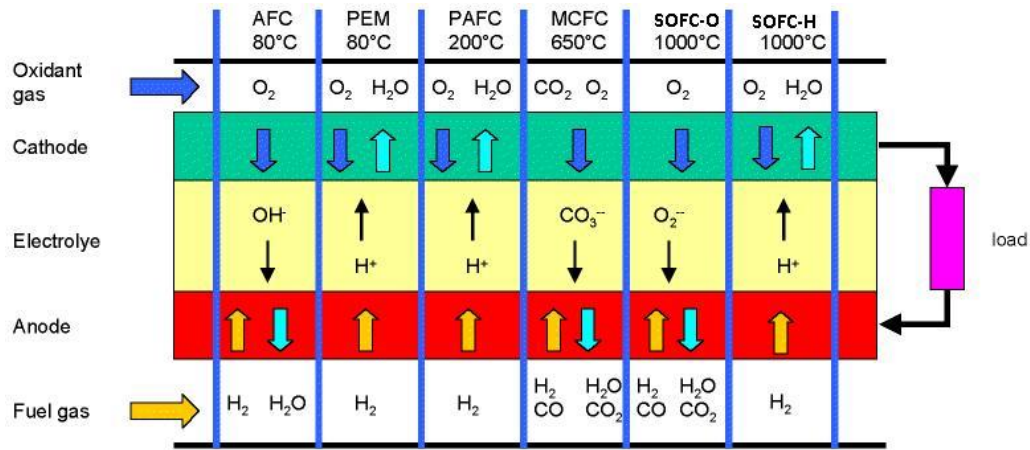


Figure 3.1: Types of fuel cells (modified from [56]).

Table 3.1: Summary of the main features of different types of fuel cells.

	AFC	PEM	PAFC	MCFC	SOFC
Electrolyte	Mobilized or Immobilized Potassium Hydroxide	Hydrated Polymeric Ion exchange membrane	Immobilized Liquid Phosphoric Acid	Immobilized Liquid Molten Carbonate	Perovskite (Ceramics)
Operating Temperature (°C)	50-200	30-100	150-220	650-700	500-1000
Charge Carrier	OH ⁻	H ⁺	H ⁺	CO ₃ ²⁻	H ⁺ or O ²⁻
External Fuel Reforming	Required	Required	Required	Optional	Optional
Carbon-based Fuel	No	No	No	Yes	Yes
Product Water Management	Evaporative	Evaporative	Evaporative	Gaseous	Gaseous
Primary Cell Components	Carbon based	Carbon based	Graphite based	Stainless Steel	Ceramics

Sources: [46,57,58,59,60,61,62].

3.2.1 Alkaline Fuel Cell (AFC)

The Alkaline fuel cell, also called the Bacon cell, was invented by Francis Thomas Bacon. The working temperature of this fuel cell is 50-200 °C [57] and the electrolyte material is usually made of aqueous alkaline solution, such as potassium hydroxide (KOH). In the mid-sixties, NASA decided to heavily invest in its development to provide on-board electric power for the Apollo spacecraft missions. The Alkaline fuel cell has enjoyed much success ever since and it is now considered to be one of the most developed fuel cell technologies. This fuel cell is also known for its exceptional performance on hydrogen and oxygen in comparison to other types of fuel cell; nevertheless, the sensitivity of the electrolyte to the presence of carbon dioxide and carbon monoxide is known to be a major disadvantage. Though it is possible to create high purity hydrogen and oxygen using current technology, this normally adds to the complexity and cost of the alkaline fuel cell system [58,62].

3.2.2 Proton-Exchange Membrane Fuel Cell (PEMFC)

PEMFC has been envisaged by many to be the most feasible alternative to combustion engines and battery systems especially for mobile and automotive applications due to its low working temperature (30-100 °C) and fast start-up time [57,60]. It is also referred to as polymer electrolyte fuel cell (PEFC) owing to the solid polymer membrane used as electrolyte. While the use of solid electrolyte mitigates the problems of sealing and assembly, it gives rise to other issues such as water and thermal management in the cell membrane. Some other disadvantages

include the risk of electrolyte poisoning by carbon monoxide trace in the fuel mixture and the use of expensive electrode materials [60].

3.2.3 Phosphoric Acid Fuel Cell (PAFC)

The PAFC was originally developed for large-scale commercial applications. It employs concentrated phosphoric acid as a mobile electrolyte and capable of working at temperatures of 150-220 °C [57]. The desirable features of the PAFC include its moderate efficiency, tolerance to carbon monoxide and simple requirements for water management system in comparison to AFC and PEMFC. The technical shortcomings of this technology are large size requirements, relatively long warm-up time and the need for precious-metal catalysts for the electrochemical reaction at the electrodes [57,62].

3.2.4 Molten Carbonate Fuel Cell (MCFC)

An interesting feature of this technology is the need for the presence of carbon dioxide gas in the oxidant steam for proper operation. The high operating temperature (650-700 °C) [61] of the fuel cell means that good reaction rates can be achieved using inexpensive electrode and catalysts materials which greatly reduce the system cost. Additionally, the use of immobilized molten carbonate suspended in lithium aluminum oxide as electrolyte allows for the direct use of fuel mixtures with high concentrations of carbon monoxide and carbon dioxide. However, the corrosive nature of the electrolyte calls for the use of special construction materials

such as stainless steel and graphite. Another trade-off of this technology is the long start-up time due to the high working temperature which makes the MCFC more suitable for stationary and continuous operation applications [58,61].

3.2.5 Solid Oxide Fuel Cell (SOFC)

As the name suggests, this fuel cell employs dense metal oxide or ceramic as the electrolyte material. The SOFC technology encompasses a wide range of configuration but can be classified as shown in Figure 3.2.

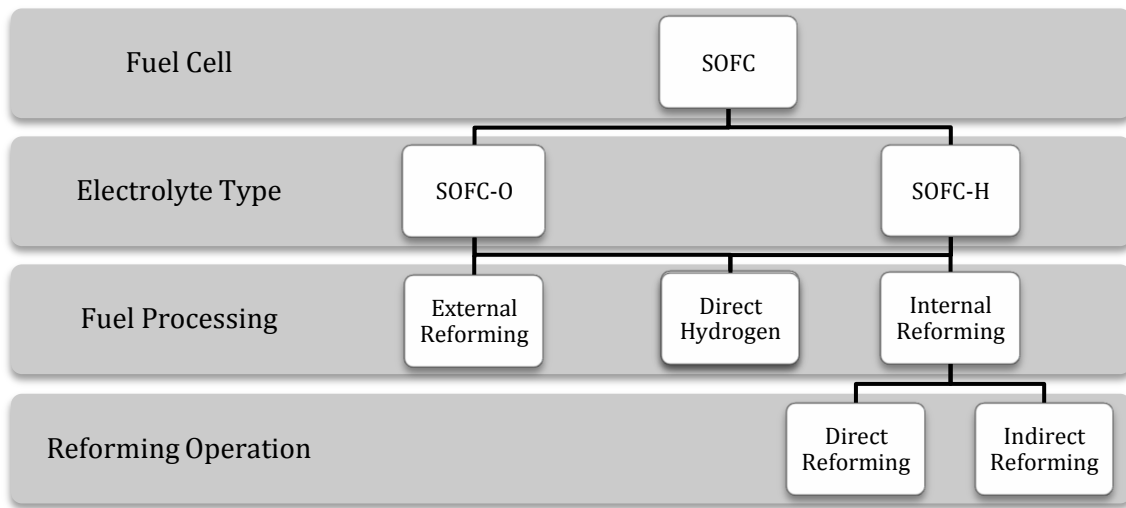


Figure 3.2: General configuration of solid oxide fuel cells.

Certain types of solid electrolyte facilitate the transport of oxygen ions hence the name oxygen ion-conducting solid oxide fuel cell (SOFC-O) while other types of electrolyte transport hydrogen ions (protons) hence the name hydrogen proton-conducting solid oxide fuel cell (SOFC-H). Owing to their high operating

temperature which is between 500 and 1000 °C [46], solid oxide fuel cells enjoy a high degree of fuel processing flexibility as they can operate directly on hydrogen fuel or reform different fuel mixtures to extract the hydrogen. The process of reforming can take place outside or inside the cell. In the latter case, direct internal reforming has been studied extensively; however, indirect internal reforming is also under investigation in efforts to circumvent carbon deposition (coking) on the surface of the anode when carbon-based fuels are used as it can greatly deteriorates the performance of the fuel cell [46,63].

In addition, the fuel flexibility and the high operating temperature are favourable attributes that lead to higher operating efficiency and reduced cost due to system compactness and elimination of expensive materials for construction. The associated drawbacks of these features include very long start-up time and other technical problems like thermally-induced stresses due to thermal expansion mismatch of the cell components [46]. Research is currently very active to develop specific electrode and electrolyte materials to further lower the operating temperature and improve the cell performance.

3.3 Thermodynamics of Fuel Cells

3.3.1 Reversible Cell Potential

The maximum possible potential of a reversible fuel cell can be described using the laws of thermodynamics. As depicted in Figure 3.3, the total enthalpy of reactants is delivered to the fuel cell while the total enthalpy of products is leaving out of the

cell; therefore, the difference of both quantities is the net change of enthalpy inside the fuel cell. From the first law of thermodynamics

$$\Delta H = Q_{rev} - W_{rev} \quad (3.2)$$

The generated heat and work are the products of the electrochemical reaction inside the fuel cell. For a reversible process, the second law of thermodynamics gives

$$Q_{rev} = T_{FC}\Delta S \quad (3.3)$$

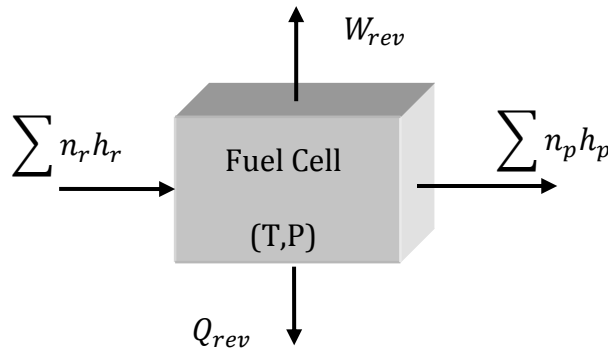


Figure 3.3: The reversible fuel cell.

From Equations (3.2) and (3.3), the reversible work produced can be described as

$$W_{rev} = \Delta H - T_{FC}\Delta S \quad (3.4)$$

The right-hand side of the above equation is also equal to the net change in Gibbs energy. Therefore, it is clear that the maximum possible work output from a reversible fuel cell is

$$W_{max} = -\Delta G \quad (3.5)$$

Moreover, the electrical work output from the fuel cell can be defined as the product of the electrical charge and the potential as

$$W = cE^0 \quad (3.6)$$

While the total charge transferred per mole of consumed fuel is

$$c = zF \quad (3.7)$$

From Equations (3.6) and (3.7), the work output is

$$W_{max} = zFE^0 \quad (3.8)$$

Thus, the final expression of the reversible (maximum) cell potential is obtained by combining Equations (3.5) and (3.8) and re-arranging to yield

$$E^0 = \frac{-\Delta G}{zF} \quad (3.9)$$

This is also referred to as the standard cell voltage.

3.3.2 Effect of Temperature on the Reversible Cell Potential

Differentiating Equation (3.4) with respect to the temperature while holding the pressure constant, yields

$$\left(\frac{\partial \Delta G}{\partial T}\right)_P = -\Delta S \quad (3.10)$$

incorporating Equation (3.10) into (3.9) and re-arranging gives

$$\left(\frac{\partial E^0}{\partial T}\right)_P = \frac{\Delta S}{zF} \quad (3.11)$$

The above equation clearly shows the dependency of the open cell voltage on the entropy of the fuel cell reaction. It follows that in the case of the oxidation reaction of hydrogen which has a negative entropy change, the standard cell potential decreases as the reaction temperature increases.

3.3.3 Effect of Pressure on Reversible Cell Potential

Differentiating Equation (3.4) above with respect to pressure while holding the temperature constant results in

$$\left(\frac{\partial \Delta G}{\partial P}\right)_T = \Delta v \quad (3.12)$$

substituting Equation (3.12) into (3.9) and re-arranging yields

$$\left(\frac{\partial E^0}{\partial P}\right)_T = \frac{-\Delta v}{zF} \quad (3.13)$$

For ideal gas reactions

$$\Delta v = \frac{\Delta n \bar{R} T}{P} \quad (3.14)$$

Finally, the combination of Equations (3.13) and (3.14) gives

$$\left(\frac{\partial E^0}{\partial P}\right)_T = \frac{-\Delta n \bar{R} T}{zFP} \quad (3.15)$$

The above equation indicates that when the reactants contain more moles of

gaseous species than the products, as in the case for the oxidation of hydrogen, the standard cell potential increases when the pressure is increased.

3.3.4 Effect of Concentration on Reversible Cell Potential

The analysis presented in the previous section applies strictly to pure reactants and products streams. In practical fuel cell systems, the reactants and products may be diluted by different chemical species depending on the type of fuel and oxidant used as well as the operating conditions. The effect of concentration reduction on the reversible cell potential can be captured by considering the partial pressure of the species involved in the electrochemical reaction of the fuel cell.

For a general fuel cell reaction



the Gibbs energy can be defined as

$$\Delta G = \Delta G^0 + \bar{R}T \ln \left[\frac{(p_C)^c (p_D)^d}{(p_A)^a (p_B)^b} \right] \quad (3.17)$$

substituting Equations (3.5) and (3.9) in (3.17) yields

$$E = E^0 + \frac{\bar{R}T}{zF} \ln \left[\frac{(p_C)^c (p_D)^d}{(p_A)^a (p_B)^b} \right] \quad (3.18)$$

When hydrogen and oxygen are electrochemically reacted, water is formed as a product. In this case, the open cell voltage can be written as

$$E = E^0 + \frac{\bar{R}T}{2F} \ln \left[\frac{p_{H_2} (p_{O_2})^{1/2}}{p_{H_2O}} \right] \quad (3.19)$$

The partial pressure can be expressed in terms of the concentration (molar fraction) of chemical species such that

$$p_i = y_i P \quad (3.20)$$

The molar fractions of all reactants and products can be obtained from the thermodynamic equilibrium of the fuel cells reactions which will be discussed next.

3.3.5 Thermodynamic Equilibrium of Fuel Cell Reactions

Thermodynamic equilibrium is the state at which the chemical activities or concentrations of the reactants and products have no net change at a given time. The stoichiometric method [24,25] and the method of Gibbs energy minimization (GEM) [64,65] are normally used to arrive at the equilibrium of reactions. The latter is a technique that is particularly useful for determining the thermodynamic equilibrium of systems having a large number of simultaneous reactions. The equilibrium composition can be directly obtained by minimizing the total Gibbs energy

$$(\Delta G_{system})_{T,P} = 0 \quad (3.21)$$

where the Gibbs energy of the system can be defined as the sum of moles of chemical species i multiplied by the respective specific Gibbs energy at constant temperature and pressure

$$G_{system} = \sum n_i \bar{g}_i \quad (3.22)$$

The specific Gibbs energy can be described as the sum of the standard Gibbs function of formation and the chemical activity of species i . For real gases, the activity of species is defined as the ratio of its fugacity in the system to that at STP.

$$\bar{g}_i = \bar{g}_{fi}^0 + RT \ln \frac{f_i}{f_i^0} \quad (3.23)$$

If ideal or perfect gas condition is assumed, the activity of the gaseous species is equal to its partial pressure in the system. For condensed matter (solid or liquid), the activity is equal to unity [66]. Therefore, the total Gibbs energy of the system is

$$G_{system} = \left(\sum n_i [\bar{g}_{fi}^0 + \bar{R}T \ln(y_i P)] \right)_{gas} + \left(\sum n_i \bar{g}_{fi}^0 \right)_{condensed} \quad (3.24)$$

As an advantage of this method, chemical reactions need not to be specified. Instead, GEM requires data of the standard Gibbs function of formation of all chemical species which are expected to be involved or contribute to the global reaction under consideration. The data were obtained from the JANAF tables [67]. The minimization of Equation (3.24) was performed using the optimization function in MATLAB [68].

3.4 Operational Principles of Hydrogen-fed Solid Oxide Fuel Cells

3.4.1 Oxygen Ion-Conducting Solid Oxide Fuel Cells (SOFC-O)

The first solid-state oxygen ion conductor, $(ZrO_2)_{0.85}(Y_2O_3)_{0.15}$ or (YSZ), was discovered accidentally by Walther Nernst in 1899 but it was not until 1954 when Westinghouse Electric Corporation embarked on the development of solid oxide fuel

cells for practical applications [69]. The basic operational principle is illustrated in Figure 3.4. When oxygen from air is used as an oxidant in SOFC-O, it enters the cathode channel and crosses the porous cathode reaching the cathode-electrolyte interface to react with electrons returning from the external circuit such that

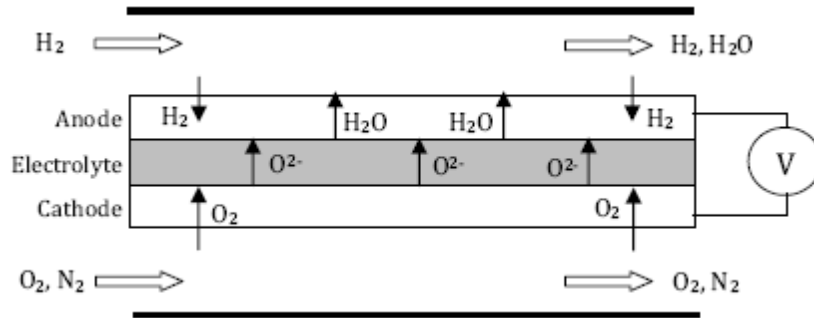


Figure 3.4: Hydrogen-fed Oxygen Ion-Conducting Solid Oxide Fuel Cell (SOFC-O).

The products of the reaction, the oxygen ions, are then transported across the oxygen ion conductor to reach the anode-electrolyte interface. The pure hydrogen fuel entering through the anode channel is transported through the porous anode to react with the oxygen ions at the anode-electrolyte interface such that



which forms water vapour and releases electrons to the external circuit. The overall reaction produces electrical energy, heat energy and water vapour



3.4.2 Hydrogen Proton-Conducting Solid Oxide Fuel Cells (SOFC-H)

The solid-state electrolyte used in SOFC-H exhibits high proton conductivity at moderate to high temperatures. The cell is depicted in Figure 3.5. As the hydrogen gas flows through the anode channel, its molecules traverse through the porous anode layer to reach the anode-electrolyte interface where the following reaction occurs

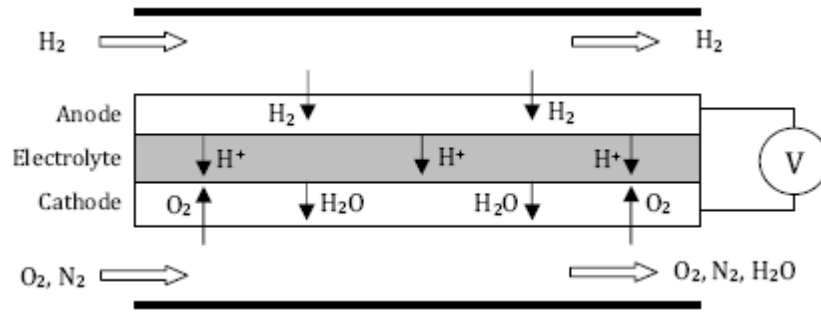
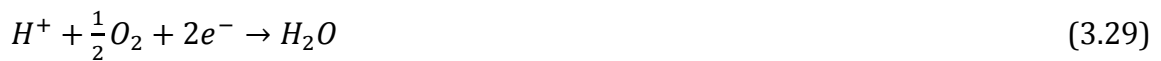


Figure 3.5: Hydrogen-fed Proton-Conducting Solid Oxide Fuel Cell (SOFC-H).

The protons are then transported through the electrolyte while the electrons create a separate current that can be utilized (load) before they return to the cathode, to be reunited with the hydrogen and oxygen in a molecule of water



The overall reaction is similar to that of the SOFC-O



Chapter Four : System Description

4.1 Description and Operational Principles of DA-SOFC Cells

4.1.1 Oxygen Ion-Conducting DA-SOFC

The operating principle of the ammonia-fed SOFC-O is assumed to take an indirect path to the oxidation of the fuel by thermally decomposing the ammonia to extract the hydrogen which will then be directly oxidized in the fuel cell as described earlier. Using pure and dry hydrogen directly as a fuel eliminates the negative impact of concentration polarization on the reversible cell potential but as shown in Figure 4.1, this is not the case for the ammonia-fed SOFC-O. Depending on the thermodynamic equilibrium of the ammonia decomposition reaction at a given temperature and pressure, nitrogen gas can be produced in high concentration that dilutes the hydrogen and reduces the cell potential. Furthermore, the inert nitrogen does not participate in any detrimental side reaction. As such, only hydrogen gas molecules will be traversing through the anode and catalyst layers to reach the anode-electrolyte interface.

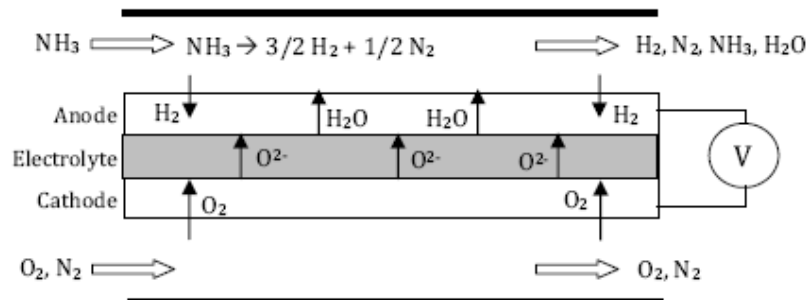


Figure 4.1: Schematic representation of ion-conducting direct ammonia solid oxide fuel cell.

On the cathode side, nitrogen is considered as an inert diluent to the oxidant while oxygen is transported through the catalyst and cathode layers to the cathode-electrolyte interface where it is reduced to oxygen ion. The oxygen ions are then transported through the electrolyte to electrochemically react with hydrogen at the anode-electrolyte interface. The water vapour produced by the reaction is transported to the anode channel in which case can also dilute the fuel. The water vapour then exits the cell with unreacted fuel and other effluents.

4.1.2 Hydrogen Proton-Conducting DA-SOFC

Analogous to the assumption of indirect electrochemical oxidation reaction path in the case of ion-conducting DA-SOFC, the underlying difference between SOFC-H fuelled with ammonia and that fuelled with pure hydrogen is the process of ammonia decomposition at the anode side of the cell. A schematic diagram of the ammonia-fed SOFC-H is depicted in Figure 4.2.

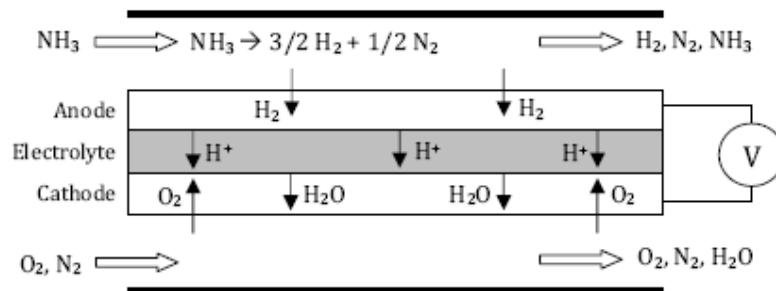


Figure 4.2: Schematic representation of proton-conducting direct ammonia solid oxide fuel cell.

Ammonia is decomposed on the anode side to produce hydrogen and nitrogen in proportions governed by the thermodynamic equilibrium of the decomposition reaction at a given temperature and pressure. While nitrogen acts as an inert diluent, hydrogen is transported to the anode-electrolyte interface where it is oxidized to hydrogen proton. Subsequently, hydrogen protons are transported through the electrolyte layer to the cathode-electrolyte interface where they are electrochemically reacted with oxygen from the cathode. The water vapour produced by the fuel cell reaction is then transported to the bulk gas in the cathode channel where it exits the cell along with other effluents. This is a major advantage of the SOFC-H over the SOFC-O counterpart since hydrogen is not diluted by the water vapour generated from the fuel cell reaction.

4.2 Description and Operational Principles of DU-SOFC Cells

4.2.1 Oxygen Ion-Conducting DU-SOFC

The operation of urea-fed SOFC-O is assumed analogous to ammonia-fed SOFC-O. A schematic diagram of the fuel cell is shown in Figure 4.3. The thermohydrolysis of urea results in the production of hydrogen, nitrogen and carbon dioxide. As discussed earlier, carbon dioxide may be involved in other intermediate reactions that can lead to the production of chemical species like carbon monoxide. Although carbon monoxide can be oxidized in SOFC-O, it has been shown in the literature review that its contribution is usually small and can be neglected without sacrificing

the accuracy of the calculations. Therefore, only hydrogen is directly oxidized and consumed in the urea-fed SOFC-O.

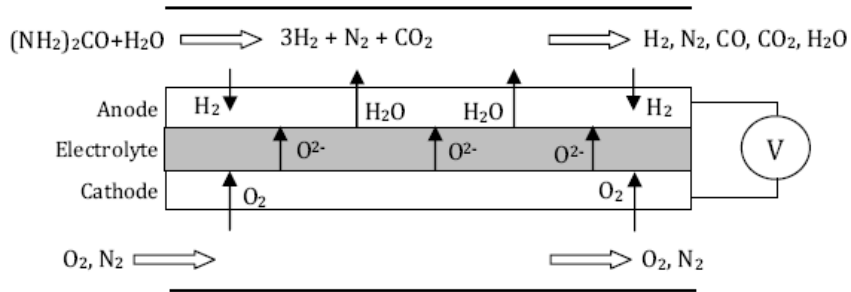


Figure 4.3: Schematic representation of oxygen ion-conducting direct urea solid oxide fuel cell.

Complications may also arise from other side reactions causing carbon formation and deposition on the anode surface which impedes the diffusion of gases and block the reaction site resulting in deteriorating performance of the fuel cell. To evade this irreversible damage, certain operating conditions like the temperature, pressure and steam-to-urea ratio (SUR) can be adjusted to reach an optimal performance. An alternative technique is the use of internal anode barrier which separates the bulk of reactions from the anode surface to mitigate the carbon deposition problem. On the cathode side, oxygen is reduced to oxygen ions and transported through the dense electrolyte to the anode side to react with the hydrogen and form water vapour.

4.2.2 Hydrogen Proton-Conducting DU-SOFC

The thermohydrolysis of urea in SOFC-H is essentially identical to that in SOFC-O. However, the hydrogen produced is oxidized to protons at the electrode-electrolyte interface and the electrons take a separate path to an external circuit (load). The protons transported through the electrolyte recombine with electrons and oxygen to form water vapour at the cathode side as shown in Figure 4.4. Difficulties may also arise from the formation of carbon (coking) and carbon monoxide on anode which can be treated in ways similar to that adopted for SOFC-O.

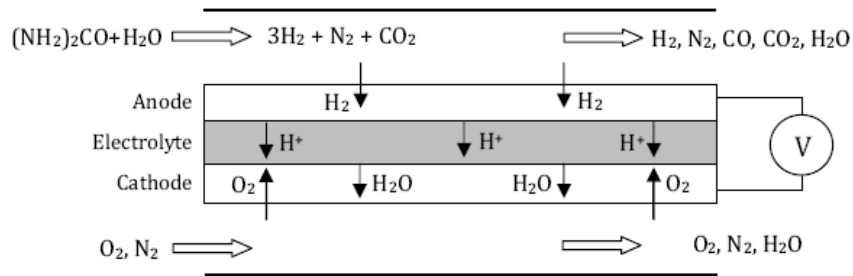


Figure 4.4: Schematic representation of hydrogen proton-conducting direct urea solid oxide fuel cell.

4.3 Description of Integrated SOFC-GT System

DA-SOFC can be integrated with a bottoming cycle such as the one shown in Figure 4.5. The solid oxide fuel cell is incorporated into a gas power cycle in a combined heat and power system. When ammonia fuel is used, it is stored under a moderate pressure in the tank to be delivered to the system as required. As the ammonia vapour is extracted during the operation of the system, the pressure and temperature inside the tank decrease by an amount proportional to the enthalpy of

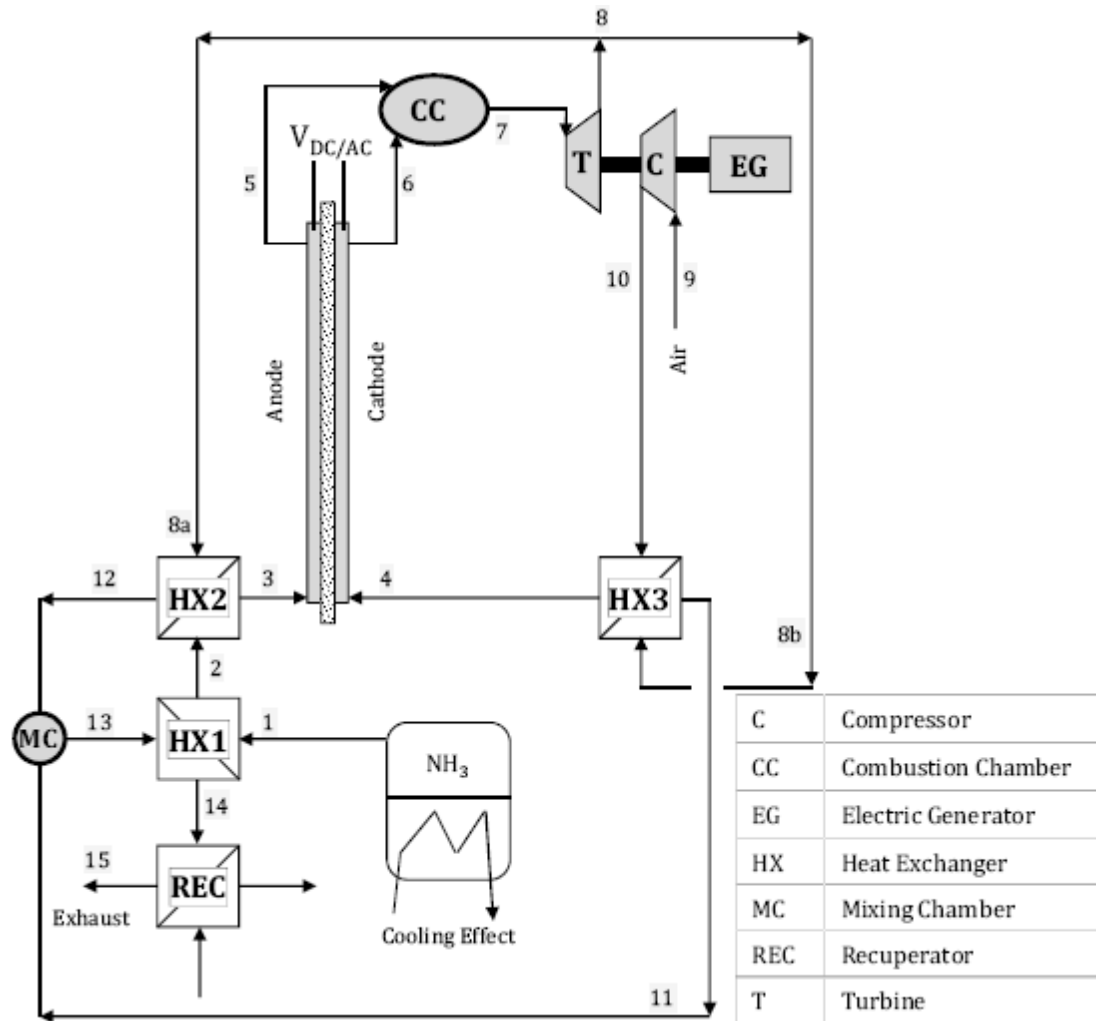


Figure 4.5: Schematic of integrated DA-SOFC/GT system.

ammonia leaving the pressurized tank. This can negatively impact the performance of the system. In order to correct it, heat can be added to the tank contents by means of a closed loop coil to maintain the pressure of the tank at a desired level. Moreover, a cooling effect is created by exploiting the refrigeration properties of ammonia which can be effectively utilized to cool the fluid inside the closed loop coil. This arrangement provides a simple and cost effective alternative to combined

SOFC-Absorption refrigeration cycles. The extracted ammonia is then heated in a two-stage heat exchanger arrangement (HX1 and HX2) to achieve a reasonable temperature before entering the fuel cell stacks. At this point, air is drawn into the compressor unit to be compressed to the desired pressure and further heated in a heat exchanger (HX3) to raise its temperature before entering the fuel cell stacks at the cathode side. The fuel and oxidant are electrochemically reacted inside the fuel cell stacks to produce electrical power. The heat generated inside the fuel cell due to thermodynamic irreversibilities is used for the thermal decomposition of ammonia and further heating of the reactants and products. Governed by the fuel utilization factor, a fraction of the hydrogen dissociated from ammonia exits the fuel cell stacks along with other gaseous effluents to be burned in the adiabatic combustion chamber. The temperature of the gas mixture leaving the combustion chamber is now higher and can be fed to the gas turbine to be expanded and produce useful mechanical power. Some of the work produced is used to drive the compressor while the remainder is used to drive an electric generator. The gas mixture leaving the turbine is split to two separate branches directed to the heat exchangers discussed earlier. Furthermore, heat can be recovered from the exhaust gas which is leaving the system at a moderate temperature.

When DU-SOFC is employed as shown in Figure 4.6, solid urea is delivered by means of a screw feeder to the heat exchanger/mixer (HXM) unit. Water is delivered from the atmospheric storage tank to the same unit via liquid pump. In this case, no cooling effect can be directly extracted from the system. The process of thermohydrolysis of urea is initiated in HXM where the reactants are heated before

Chapter Five : Thermodynamic Analysis

5.1 Cell-level Thermodynamics

5.1.1 Thermolysis of Ammonia in DA-SOFC

When heated, ammonia is decomposed to hydrogen and nitrogen according to the following reaction:



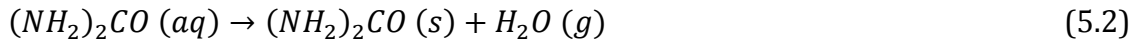
The above reaction is endothermic and depends on the temperature and pressure of the system. The reaction proceeds to the right as the temperature increases or to the right as the pressure increases thus producing less hydrogen. For the purpose of this analysis, it is assumed that the ammonia is directly fed to the fuel cell where it will be consumed and the only species involved in the decomposition process are NH_3 , H_2 and N_2 .

Catalysts are used to lower the activation energy and speed up the rate of ammonia decomposition reaction within the fuel cell. Much effort has been focused on finding a suitable catalyst to promote the decomposition of ammonia at low temperature and high kinetic rate. Although ruthenium-based catalysts are expensive, they can achieve near complete decomposition of ammonia at temperatures around 600K [70]. More attractive alternatives include nickel-based catalysts which are relatively cheaper and can achieve the same task at about 700-800K [59]. Since the operating temperature of an average SOFC ranges between 900-1400K [58], it is safe to

neglect the kinetic rate of reaction and assume that full decomposition of ammonia is attained within the porous anode layer.

5.2.1 Thermohydrolysis of Urea in DU-SOFC

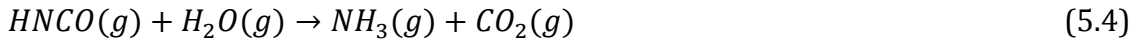
An aqueous solution composed of equimolar amounts of urea and water (76.92% urea by weight) can be heated and injected into the system resulting in a transitory evaporation of water from the spray droplets such that



The rapid thermolysis of solid urea can be initiated at a relatively low temperature of 406K [39] to yield ammonia and isocyanic acid as



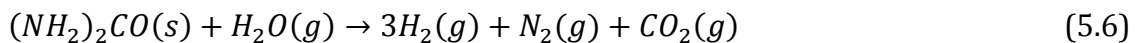
while the simultaneous hydrolysis of isocyanic acid over a catalyst like titanium oxide anatase gives



resulting in the following reaction:



Further heating of the products over a suitable catalyst like nickel will initiate the decomposition of ammonia to hydrogen and nitrogen to yield the final reaction



Furthermore, other chemical species like carbon (graphite) and carbon monoxide formed during intermediate or side reactions are considered for determining the thermodynamic equilibrium of the thermohydrolysis of urea.

5.1.3 Fuel and Oxidant Utilization

The utilization of ammonia or urea can be defined in terms of the actual supply and consumption of the fuel or its hydrogen equivalent such that

$$U_f = \frac{(Fuel)_{consumed}}{(Fuel)_{supplied}} = \frac{(H_2)_{consumed}}{(H_2)_{supplied}} \quad (5.7)$$

Similarly, the utilization of air as an oxidant can be expressed as a function of the air supply and usage or its oxygen equivalent since air can be assumed to be composed of 79% nitrogen and 21% oxygen by volume

$$U_o = \frac{(Air)_{consumed}}{(Air)_{supplied}} = \frac{(O_2)_{consumed}}{(O_2)_{supplied}} \quad (5.8)$$

This is applicable to ion-conducting and proton-conducting cells.

5.2 Electrochemical Analysis

The examination of solid oxide fuel cells at closed circuit conditions requires the characterization of the overpotentials affecting the cell operation. The working potential or voltage of SOFC can be determined as

$$V = E - \varphi_{act,an} - \varphi_{act,ca} - \varphi_{\Omega} - \varphi_{conc,an} - \varphi_{conc,ca} \quad (5.9)$$

The models described below are applicable to all types of SOFC under investigation in this study.

5.2.1 Activation Overpotential

This type of irreversible loss is related to the electrode kinetics and represents the difference between the actual potential (closed-circuit conditions) and the reversible potential (open-circuit conditions). The implicit relationship between the current density and the activation overpotential can be described using the Butler-Volmer expression [60,61]:

$$J = J_0 \left[\exp\left(\frac{\alpha z F \varphi_{act}}{\bar{R}T}\right) - \exp\left(-\frac{(1-\alpha)z F \varphi_{act}}{\bar{R}T}\right) \right] \quad (5.10)$$

The exchange current density (J_0) is a measure of the magnitude of electron activity at the equilibrium potential of the electrode. Its value is highly influenced by the electrode material, structure and other factors such as the temperature of the reaction and the length of TPB [51]. The charge transfer coefficient (α) describes the effect of the electrical potential on the ratio of the forward to the reverse activation barrier. For most electrochemical reactions in fuel cells, this value is assumed as 0.5 [63,71]. In addition, the parameter (z) refers to the number of electron transferred per mole of fuel. Therefore, the explicit relationship of the activation overpotential is

$$\varphi_{act,\gamma} = \frac{\bar{R}T}{F} \sinh^{-1}\left(\frac{J}{zJ_{0,\gamma}}\right), \quad \gamma = anode, cathode \quad (5.11)$$

5.2.2 Ohmic Overpotential

The electronic resistance of the fuel cell electrode and interconnect is usually very small and is considered negligible when compared to the ionic resistance of the electrolyte which can be described by Ohm's law [46,71]

$$\varphi_{\Omega} = J\delta R_{\Omega} \quad (5.12)$$

The electrolyte resistance (R_{Ω}) is a function of the electrolyte properties and is highly dependent on the operating temperature.

5.2.3 Concentration Overpotential

The concentration overpotential accounts for losses incurred by the resistance of the porous electrode to the transport of gaseous species between the gas channel and the reaction sites at TPB. The mass transport in the electrodes is driven by the diffusion of reacting species due to concentration gradient as well as the permeation caused by pressure gradient [72,73]. Several mass transport models with varying accuracies have been used to capture the effects of concentration overpotential on the performance of fuel cells. It has been demonstrated that the highest accuracy can be achieved by using the dusty-gas model (DGM) [73] and the mean transport pore model (MTPM) [74]. The one-dimensional multi-component mass transport model using DGM can be written as

$$\frac{N_i}{D_{i,k}^{eff}} + \sum_{j=1, j \neq i} \frac{y_j N_i - y_i N_j}{D_{ij}^{eff}} = -\frac{1}{RT} \left[P \frac{dy_i}{dx} + y_i \frac{dP}{dx} \left(1 + \frac{B_0 P}{\mu_{mix} D_{i,k}^{eff}} \right) \right] \quad (5.13)$$

where the effective Knudsen diffusion accounts for the porosity and tortuosity of the electrode such that [72]

$$D_{i,k}^{eff} = \frac{2}{3} \frac{\epsilon}{\tau} \sqrt{\frac{8RT}{\pi M_i}} r_p \quad (5.14)$$

The effective binary diffusion of chemical species can be obtained using the Chapman-Enskog equation [75]

$$D_{ij}^{eff} = 0.0018583 \frac{\epsilon}{\tau} \sqrt{T^3 \left(\frac{1}{M_i} + \frac{1}{M_j} \right)} \frac{1}{P \sigma_{ij}^2 \Omega_{D,ij}} \quad (5.15)$$

and the mean characteristic length (σ_{ij}) of the molecular collision diameter of species i and j is given by

$$\sigma_{ij} = \frac{(\sigma_i + \sigma_j)}{2} \quad (5.16)$$

The collision integral ($\Omega_{D,ij}$) is a function of temperature and the Lennard-Jones parameter (k/ϵ_{ij})

$$\Omega_{D,ij} = \frac{1.06036}{\Gamma^{0.15610}} + \frac{0.19300}{\exp(0.47635\Gamma)} + \frac{1.03587}{\exp(1.52996\Gamma)} + \frac{1.76474}{\exp(3.89411\Gamma)} \quad (5.17)$$

where

$$\Gamma = \frac{kT}{\epsilon_{ij}} \quad (5.18)$$

and

$$\epsilon_{ij} = \sqrt{\epsilon_i \epsilon_j} \quad (5.19)$$

The values of the parameter in Equations (5.14) to (5.19) have been obtained from references [75] and [76]. The permeability of the porous electrode is estimated using the Kozeny-Carman relationship [77]

$$B_0 = \frac{4\epsilon^3 r_p^2}{72\tau(1-\epsilon)^2} \quad (5.20)$$

Furthermore, the viscosity of gas mixture can be calculated using the following semi-empirical equation [78]

$$\mu_{mix} = \frac{\sum y_i \mu_i \sqrt{M_i}}{\sum y_i \sqrt{M_i}} \quad (5.21)$$

The gas viscosities are obtained from reference [75]. As presented by Zhu and Kee [79], the summation of Equation (5.13) allows for the evaluation of the pressure gradient (dP/dx) across the electrode as

$$\frac{dP}{dx} = - \frac{\sum_{i=1} \left(\frac{N_i}{D_{i,k}^{eff}} \right)}{\left(\frac{1}{RT} \right) + \left(\frac{B_0 P}{\mu RT} \right) \sum_{i=1} \left(\frac{y_i}{D_{i,k}^{eff}} \right)} \quad (5.22)$$

At TPB, the molar flux of the gaseous reactants involved in the electrochemical reaction, namely hydrogen and oxygen, can be related to the current density as [31]

$$N_i = \frac{J}{zF} \quad (5.23)$$

where z is equal to two for hydrogen and four for oxygen. Depending on the type of electrolyte (SOFC-O or SOFC-H), the molar flux of water vapour can be calculated using Graham's law of diffusion which governs the diffusion in gas mixtures [73]:

$$\sum_i N_i \sqrt{M_i} = 0 \quad (5.24)$$

The molar fluxes of all other non-reacting species are equal to zero [27,31]. The set of simultaneous differential equations represented by Equation (5.13) is solved numerically using the function (ode45) in MATLAB [68] to obtain the molar fractions and partial pressures of the reacting species at TPB. Finally, the relationship between the concentration overpotential and the partial pressures can be written as [63,80]

For SOFC-O:

$$\varphi_{conc,an} = \frac{\bar{R}T}{2F} \ln \left(\frac{p_{H_2}^{TPB} p_{H_2O}}{p_{H_2} p_{H_2O}^{TPB}} \right) \quad (5.25)$$

$$\varphi_{conc,ca} = \frac{\bar{R}T}{4F} \ln \left(\frac{p_{O_2}}{p_{O_2}^{TPB}} \right) \quad (5.26)$$

For SOFC-H:

$$\varphi_{conc,an} = \frac{\bar{R}T}{2F} \ln \left(\frac{p_{H_2}}{p_{H_2}^{TPB}} \right) \quad (5.27)$$

$$\varphi_{conc,ca} = \frac{\bar{R}T}{2F} \ln \left(\frac{p_{H_2O}^{TPB} \sqrt{p_{O_2}}}{p_{H_2O} \sqrt{p_{O_2}^{TPB}}} \right) \quad (5.28)$$

5.3 Maximum Electrochemical Efficiency

The maximum electrochemical efficiency of SOFC can be defined as [26]

$$\eta_{elc} = \frac{zFEU_f}{-\Delta H^0} \quad (5.29)$$

Since only hydrogen is oxidized in the fuel cell, its lower heating value is used in this particular calculation.

5.4 Energy and Exergy Analyses of Integrated System

At steady state operation, the energy balance of the system or any of its components can be written as

$$\dot{Q} - \dot{W} + \sum_i (\dot{n}_i \bar{h}_i)_{in} - \sum_i (\dot{n}_i \bar{h}_i)_{out} = 0 \quad (5.30)$$

Furthermore, the exergy associated with material flow is the sum of physical exergy and chemical exergy

$$\dot{E}x = \dot{E}x_{ph} + \dot{E}x_{ch} \quad (5.31)$$

where

$$\dot{E}x_{ph} = \sum_i \dot{n}_i [(\bar{h}_i - \bar{h}_0) - T_0(\bar{s}_i - \bar{s}_0)] \quad (5.32)$$

$$\dot{E}x_{ch} = \dot{n} [\sum_i y_i \bar{e}x_{ch,i}^0 + \bar{R}T_0 \sum_i y_i \ln y_i] \quad (5.33)$$

The previous expressions assume negligible change in kinetic and potential energies. In addition, the exergy of work is work itself; however, exergy delivered by heat transfer is governed by the Carnot efficiency such that

$$\dot{E}x_Q = \dot{Q}_j \left[1 - \frac{T_0}{T} \right] \quad (5.34)$$

In this study, the exergy is evaluated against a reference temperature and pressure at STP conditions. The exergy destruction due to thermodynamic irreversibilities in any component can be written as

$$\dot{E}x_{D,cmp} = \sum_j \dot{Q}_j \left[1 - \frac{T_0}{T} \right] - \dot{W} + \sum_i (\dot{E}x_i)_{in} - \sum_i (\dot{E}x_i)_{out} \quad (5.35)$$

and the total exergy destruction in the system is

$$\dot{E}x_{D,total} = \sum \dot{E}x_{D,cmp} \quad (5.36)$$

For DA-SOFC/GT and DU-SOFC/GT systems, the electrical energy efficiency is dependent on the lower heating value of the respective fuel

$$\eta_{e,fuel} = \frac{\dot{W}_{AC} + \dot{W}_G}{\dot{n}_{LHV}} \quad (5.37)$$

and the electrical exergy efficiency can be written as

$$\psi_{e,fuel} = \frac{\dot{W}_{AC} + \dot{W}_G}{\dot{n} \bar{e} x_{ch}^0} \quad (5.38)$$

The total energy efficiency of the DA-SOFC/GT system is

$$\eta_{total,NH_3} = \frac{\dot{W}_{AC} + \dot{W}_G + \dot{Q}_{REC}}{\dot{n}_{LHV} + \dot{Q}_{CL}} \quad (5.39)$$

and the total exergy efficiency of the DA-SOFC/GT system is

$$\psi_{total,NH_3} = \frac{\dot{W}_{AC} + \dot{W}_G + \dot{E}x_{Q_{REC}}}{\dot{n}\bar{e}x_{ch}^0 + \dot{E}x_{Q_{CL}}} \quad (5.40)$$

As for the DU-SOFC/GT system, the total energy efficiency is

$$\eta_{total,urea} = \frac{\dot{W}_{AC} + \dot{W}_G + \dot{Q}_{REC}}{\dot{n}LHV} \quad (5.41)$$

Finally, the total exergy efficiency of the DU-SOFC/GT system can be written as

$$\psi_{total,urea} = \frac{\dot{W}_{AC} + \dot{W}_G + \dot{E}x_{Q_{REC}}}{\dot{n}\bar{e}x_{ch}^0} \quad (5.42)$$

The lower heating values and standard chemical exergy values are obtained from references [59,81]. All numerical calculations are performed using EES software [82].

5.5 Energy and Exergy Analyses of System Components

In this section, ideal gas conditions are assumed. Unless otherwise stated, all components and devices are considered to be well insulated to minimize heat losses to negligible levels. Furthermore, the pressure losses have been ignored by virtue of component design.

- **Fuel Cell Stack**

The thermodynamic processes taking place inside the fuel cell module are depicted in Figure 5.1. Heat is generated by the isothermal electrochemical reaction of hydrogen and oxygen inside the fuel cell. The ratio of hydrogen to ammonia or urea entering the fuel cell is determined by the thermodynamic equilibrium and depends on the temperature and pressure of the corresponding reaction. Therefore, the heat generated and transferred based on the molar flow of hydrogen carrier is

$$\dot{Q} = x\dot{n}U_f T_{FC} \Delta \bar{s} + I(\varphi_{act,an} + \varphi_{act,ca} + \varphi_{ohm} + \varphi_{conc,an} + \varphi_{conc,an}) \quad (5.43)$$

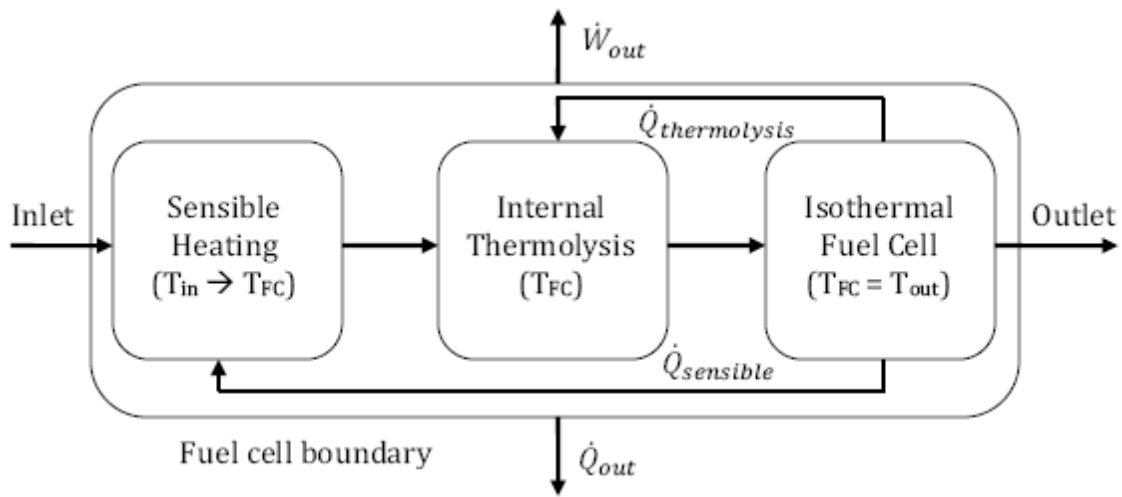


Figure 5.1: Thermodynamic processes of fuel cell stack.

This is partially used to supply sensible heat to the reactants, products as well as provide sufficient heat for the thermolysis of fuel. Furthermore, the temperature of all effluents is assumed uniform and equal to the fuel cell temperature. All surplus heat is rejected outside the fuel cell stacks. The thermal efficiency of the fuel cell stack can be written as

$$\eta_{FC} = \frac{W_e}{\Delta H} \quad (5.44)$$

and the exergy efficiency is

$$\psi_{FC} = 1 - \frac{\dot{E}x_{D,FC}}{\sum_i(\dot{n}_i \bar{e}x_i)_{in} - \sum_i(\dot{n}_i \bar{e}x_i)_{out}} \quad (5.45)$$

Finally, the actual AC power produced by the fuel cell stack is

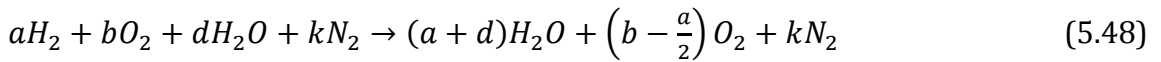
$$\dot{W}_{AC} = \eta_{INV} \dot{W}_{FC} \quad (5.46)$$

▪ **Combustion Chamber**

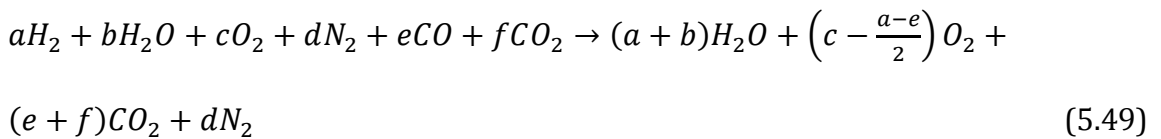
Unreacted hydrogen and other effluents including excess air leave the fuel cell stacks and enter the combustion chamber where no work is done. It is also assumed that excess air ensures complete combustion. Applying the principles of energy conservation and mass conservation on the component, yields

$$\sum_i(\dot{n}_i \bar{h}_i)_{in} = \sum_i(\dot{n}_i \bar{h}_i)_{out} \quad (5.47)$$

For DA-SOFC/GT, this translates to



and for DU-SOFC/GT



Knowing the molar flow rate and the chemical composition of the combustion reactants and products, the adiabatic combustion temperature can be iteratively determined. Finally, the exergy efficiency of the combustion chamber is

$$\psi_{CC} = 1 - \frac{\dot{E}x_{D,CC}}{\sum_i(\dot{E}x)_{in}} \quad (5.50)$$

▪ Gas Turbine

When the hot gas mixture leaves the combustion chamber and enters the gas turbine, it expands inside the gas turbine to deliver useful energy in the form of mechanical power. With the knowledge of the inlet temperature, the outlet temperature can be determined by

$$T_{out} = T_{in} \left(\frac{1}{PR} \right)^{(k-1)/k} \quad (5.51)$$

where

$$PR = \frac{P_{in}}{P_{out}} \quad (5.52)$$

$$k = \frac{\sum_i y_i \bar{c}_{p,i}}{\sum_i y_i \bar{c}_{v,i}} \quad (5.53)$$

Due to the effects of thermodynamic irreversibilities in the turbine, the actual outlet temperature is higher. To correct this, the isentropic efficiency of the turbine can be applied such that

$$\eta_{s,T} = \frac{\sum_i(\dot{n}_i \bar{h}_i)_{in} - \sum_i(\dot{n}_i \bar{h}_i)_{out}}{\sum_i(\dot{n}_i \bar{h}_i)_{in} - \sum_i(\dot{n}_i \bar{h}_i)_{s,out}} \quad (5.54)$$

The actual temperature of gas mixture leaving the turbine can be iteratively determined from the actual enthalpy obtained. The exergy efficiency of the turbine can be written as

$$\psi_T = \frac{W_T}{\sum_i(\dot{n}_i \bar{e}x_i)_{in} - \sum_i(\dot{n}_i \bar{e}x_i)_{out}} \quad (5.55)$$

▪ **Air Compressor**

This component receives air at the ambient temperature and pressure and compresses it to the desired pressure. This also results in an increase in the air temperature at the outlet of the compressor:

$$T_{out} = T_{in} (PR)^{(k-1)/k} \quad (5.56)$$

where

$$PR = \frac{P_{out}}{P_{in}} \quad (5.57)$$

$$k = \frac{\sum_i y_i \bar{c}_{p,i}}{\sum_i y_i \bar{c}_{v,i}} \quad (5.58)$$

Similar to the gas turbine, the isentropic efficiency of the compressor can relate the enthalpy of air at isentropic conditions to its actual enthalpy as

$$\eta_{s,C} = \frac{\sum_i(\dot{n}_i \bar{h}_i)_{s,out} - \sum_i(\dot{n}_i \bar{h}_i)_{in}}{\sum_i(\dot{n}_i \bar{h}_i)_{out} - \sum_i(\dot{n}_i \bar{h}_i)_{in}} \quad (5.59)$$

from which the actual outlet temperature of air is iteratively obtained. The exergy efficiency of the compressor is

$$\psi_C = \frac{\sum_i(\dot{n}_i \bar{e}_{x_i})_{out} - \sum_i(\dot{n}_i \bar{e}_{x_i})_{in}}{\dot{W}_C} \quad (5.60)$$

- **Electric Generator**

As indicated earlier, the surplus power representing the difference between the mechanical power generated by the turbine and that consumed by compressor can be captured using the back work ratio

$$bwr = \frac{\dot{W}_C}{\dot{W}_T} \quad (5.61)$$

It is definitely desired to maintain this ratio as low as possible. The surplus power is used to drive an electric generator such that

$$\dot{W}_G = \eta_G (\dot{W}_T - \dot{W}_C) \quad (5.62)$$

- **Heat Exchangers**

Multiple gas-to-gas heat exchangers are utilized in these systems. The effectiveness method [83] is used to determine the outlet temperature of the respective gaseous stream such that

$$\dot{Q} = \xi H_{C,min} (T_{h,in} - T_{c,in}) \quad (5.63)$$

where $H_{c,min}$ is the smaller of the heat capacity rate of the hot or the cold stream. As such, the outlet temperature of the hot stream is given as

$$\dot{Q} = \sum_i(\dot{n}_i \bar{c}_{p,i})_h (T_{h,in} - T_{h,out}) \quad (5.64)$$

and the cold stream

$$\dot{Q} = \sum_i (\dot{n}_i \bar{c}_{p,i})_c (T_{c,out} - T_{c,in}) \quad (5.65)$$

In the case of DU-SOFC/GT system, heat exchanger (HX2) is removed and heat exchanger (HX1) is replaced with a heater exchanger-mixer assembly (HXM) which is used to heat and vaporize the aqueous urea. The Pinch Method [58] is used for the analysis. First, solid urea and water are mixed in equimolar amounts and heated to the saturation temperature of water at a constant pressure dictated by the operating pressure of the fuel cell. The sensible heat required to raise the temperature of aqueous urea in the economizer section is approximated as

$$\dot{Q}_{eco} = \dot{n}_{aq} \bar{c}_{p,aq} (T_{sat} - T_{in}) \quad (5.66)$$

where the molar heat capacity of aqueous urea is estimated at 176 J/mol.K [9]. At a constant saturation temperature, the enthalpy of evaporation of water, the latent heat of solution and hydrolysis of urea add up to the total heat required per mole of aqueous urea in the evaporator section

$$\dot{Q}_{evp} = \dot{n}_{aq} (\Delta \bar{h}_{fg} + \Delta \bar{h}_{soln} + \Delta \bar{h}_{hyd}) \quad (5.67)$$

The values of the latent heat of solution and hydrolysis of urea are obtained from reference [84]. By assuming a pinch temperature difference, it is possible to determine the temperature of the exhaust gas at the beginning of the evaporator section such that

$$\dot{Q}_{evp} = \sum_i (\dot{n}_i \bar{c}_{p,i})_{exh} (T_{exh,in} - T_p) \quad (5.68)$$

where

$$T_p = D_p + T_{sat} \quad (5.69)$$

In addition, the final temperature of the exhaust gas exiting heat exchanger (HXM) can be determined from the heat flow rate required in the economizer section

$$\dot{Q}_{eco} = \sum_i (\dot{n}_i \bar{c}_{p,i})_{exh} (T_p - T_{exh,out}) \quad (5.70)$$

Finally, the exergy efficiency of any heat exchanger in the system can be written as

$$\psi_{HX} = \frac{(\sum_i (\dot{n}_i \bar{e}_{x_i})_{out} - \sum_i (\dot{n}_i \bar{e}_{x_i})_{in})_c}{(\sum_i (\dot{n}_i \bar{e}_{x_i})_{in} - \sum_i (\dot{n}_i \bar{e}_{x_i})_{out})_h} \quad (5.71)$$

- **Mixing Chamber**

Gas streams of different molar flow rates and temperatures flowing through different branches are mixed at a mixing chamber before entering the heat exchanger. Under the assumption of adiabatic mixing of gases, the temperature of the gaseous mixture exiting the mixing chamber can be obtained from

$$\sum_i (\dot{n}_i \bar{h}_i)_{in} = \sum_i (\dot{n}_i \bar{h}_i)_{out} \quad (5.72)$$

The exergy destruction can be determined from Equation (5.35) and the exergy efficiency can be written as

$$\psi_{MC} = 1 - \frac{\dot{E}x_{D,MC}}{\sum_i (\dot{n}_i \bar{e}_{x_i})_{in}} \quad (5.73)$$

- **Liquid Pump (DU-SOFC/GT System)**

The power drawn by the water pump is negligible in comparison to the power produced by the system; therefore, the analysis of pump is ignored in this study.

Chapter Six : Results and Discussion

6.1 Thermodynamic Equilibrium of Ammonia and Urea

Using the GEM method described earlier, the thermodynamic equilibrium of ammonia is obtained as depicted in Figure 6.1. It can be seen that the decomposition of ammonia is favoured at higher temperatures and low pressures. Nonetheless, it is well known that the reaction kinetics is rather slow and often requires the use of catalyst to promote faster conversion of ammonia.

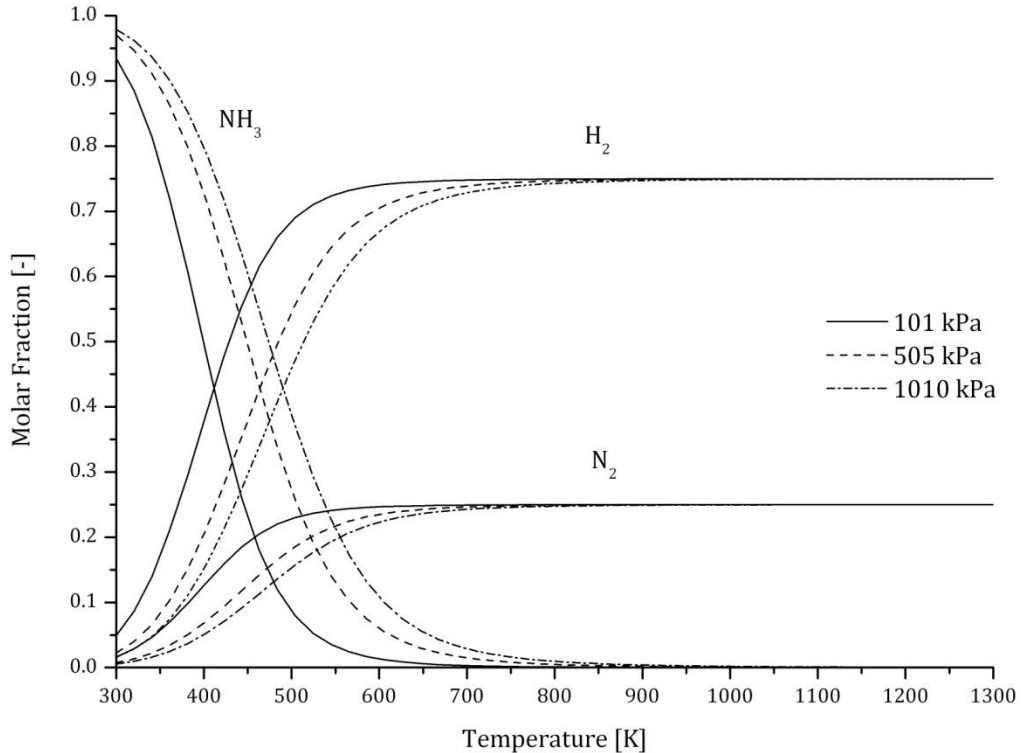


Figure 6.1: Thermodynamic equilibrium of ammonia.

Complete conversion of ammonia may be achieved over expensive metal catalysts such as ruthenium and platinum at temperatures around 600-650K [70]; however,

more economic alternatives include iron, nickel or nickel-based catalysts. Figure 6.2 contrasts between the conversion of ammonia based on the thermodynamic equilibrium and that based on the time-dependent kinetics of the same conversion reaction using nickel as a catalyst. Despite the large difference at lower temperatures, the figure shows that complete conversion of ammonia is possible at a temperature of 700K and atmospheric pressure at which the molar fraction of hydrogen reaches 0.75.

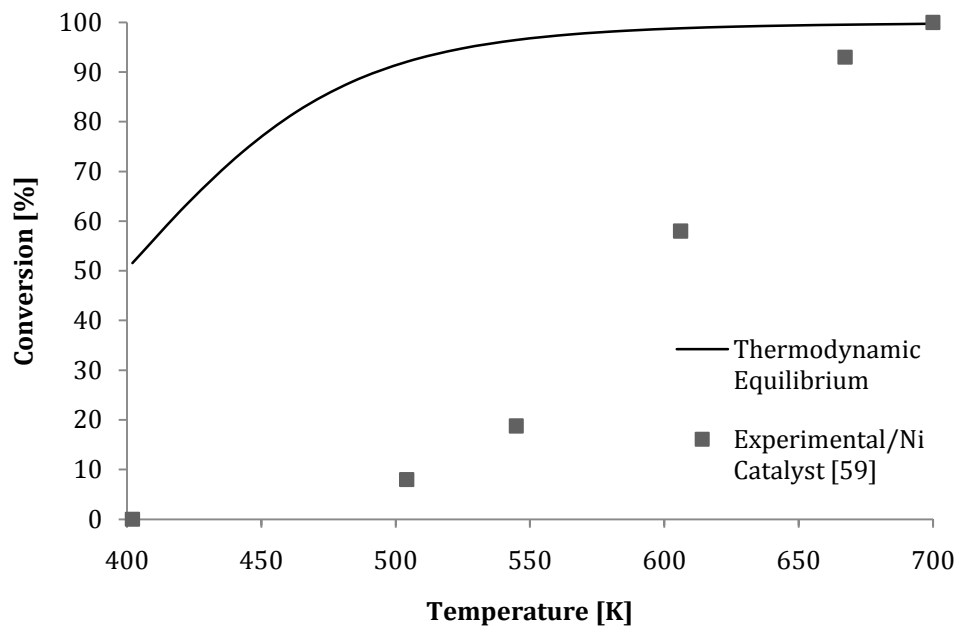


Figure 6.2: Conversion of ammonia as a function of reaction temperature.

The case is different and more complicated for the thermodynamic equilibrium of the thermohydrolysis of urea. Equimolar amounts of urea and steam are considered at two different pressures as shown in Figure 6.3. For the case of atmospheric pressure, carbon formation and deposition is dominant at temperatures up to 923K

while increasing the pressure to 505kPa causes a shift of the carbon formation boundary to 1023K.

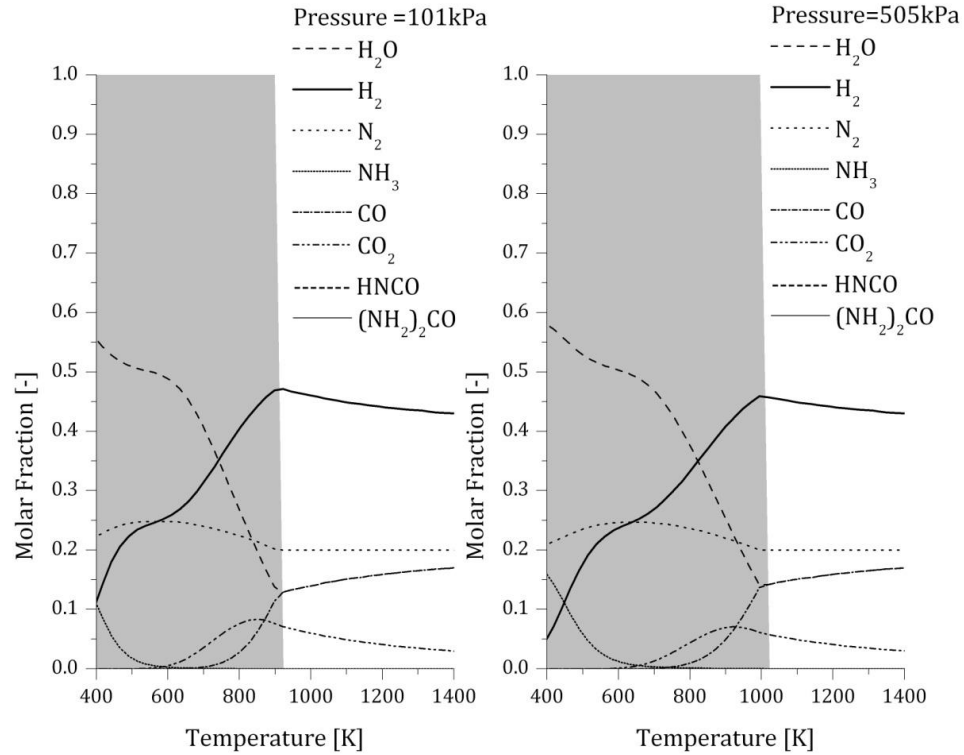


Figure 6.3: Thermodynamic equilibrium of urea (SUR=1).

The fact that urea and isocyanic acid do not appear clearly on the graph is an indication of the spontaneity of the thermohydrolysis reaction which results in negligible concentration of both compounds across all temperatures. Furthermore, the hydrogen dissociation decreases while the carbon formation boundary shifts to the right as the pressure of the system increases. This response is expected since the system is attempting to alleviate the pressure resulting from the production of higher number of gaseous molecules. Another factor that can influence the carbon formation boundary is the steam-to-urea ratio (SUR). Figure 6.4 depicts the

equilibrium of urea thermohydrolysis with SUR of 1:2 and 2:1 respectively. When SUR is low, the carbon boundary increases and shifts to higher temperatures while the molar fraction of hydrogen increases to 0.46-0.50.

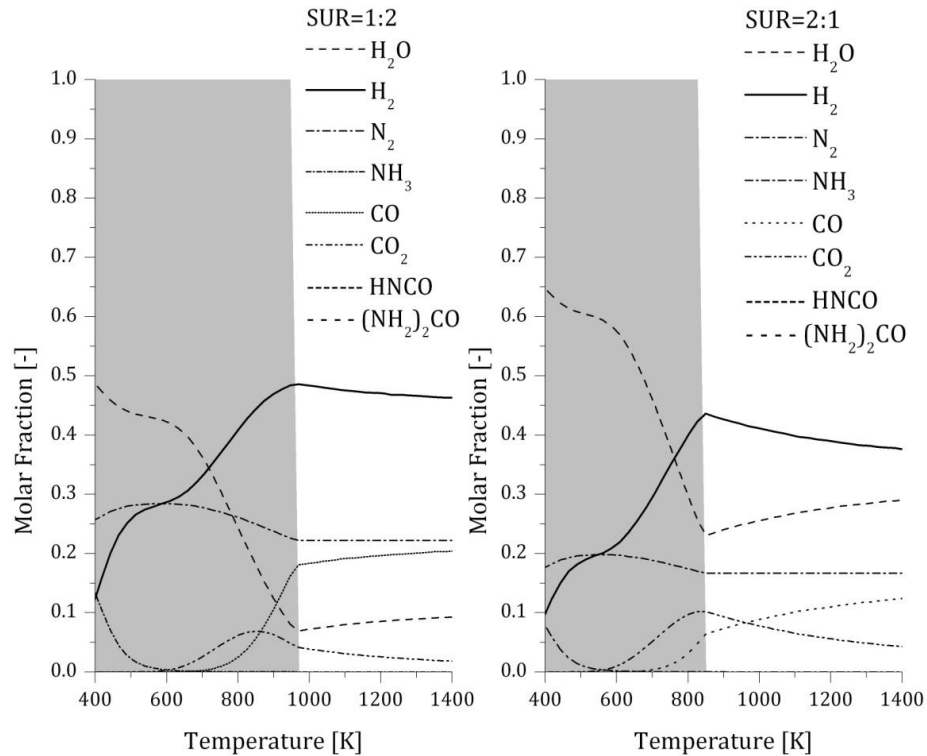


Figure 6.4: Thermodynamic equilibrium of urea (Pressure=101 kPa).

The opposite is true when SUR is high resulting in lower carbon formation boundary with reduction of the molar fraction of hydrogen to 0.37-0.43. As discussed earlier, several investigations have reported that the thermohydrolysis reaction of urea is rapid and complete; however, their narrow parametric ranges are often confined to specific applications like automotive DeNOx systems. Therefore, their results and findings cannot be directly compared to theoretical predictions made in this study.

Furthermore, the open literature lacks information regarding the kinetics of the thermohydrolysis of urea at higher temperatures ($>700\text{K}$). It is necessary to determine the kinetics of the reaction at conditions exhibited in SOFC in order to provide better understanding of the cell performance and the extent of carbon formation at the anode.

6.2 Reversible Cell Potential (Open Cell Voltage)

In the case of DA-SOFC, the variation of the molar fraction of hydrogen as a function of the ammonia utilization is illustrated in Figure 6.5. For DU-SOFC, equimolar amounts of steam and urea ($\text{SUR}=1$) is used for comparison.

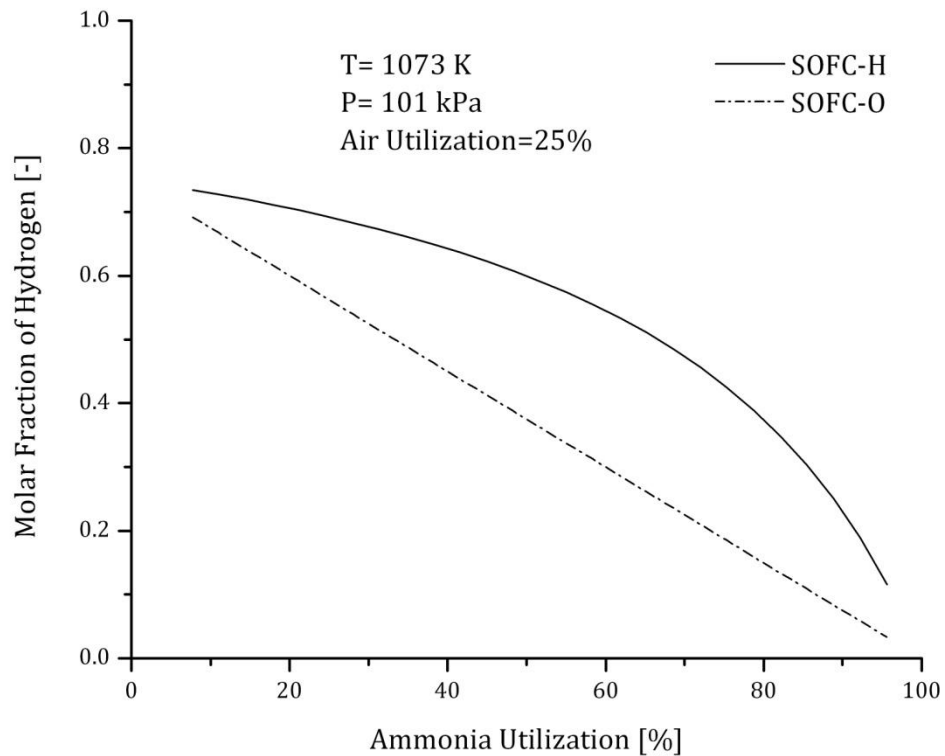


Figure 6.5: Molar fraction of hydrogen in DA-SOFC.

Hydrogen in SOFC-O anode is balanced by the equimolar formation of water vapour due the electrochemical reaction resulting in a linear profile of the molar hydrogen molar fraction. For proton-conducting DA-SOFC, a non-linear profile is observed mainly due to the decomposition of ammonia and consumption of hydrogen. In the case of proton-conducting DU-SOFC, the reverse water-gas shift reaction also contributes to the overall profile of hydrogen molar fraction as shown in Figure 6.6.

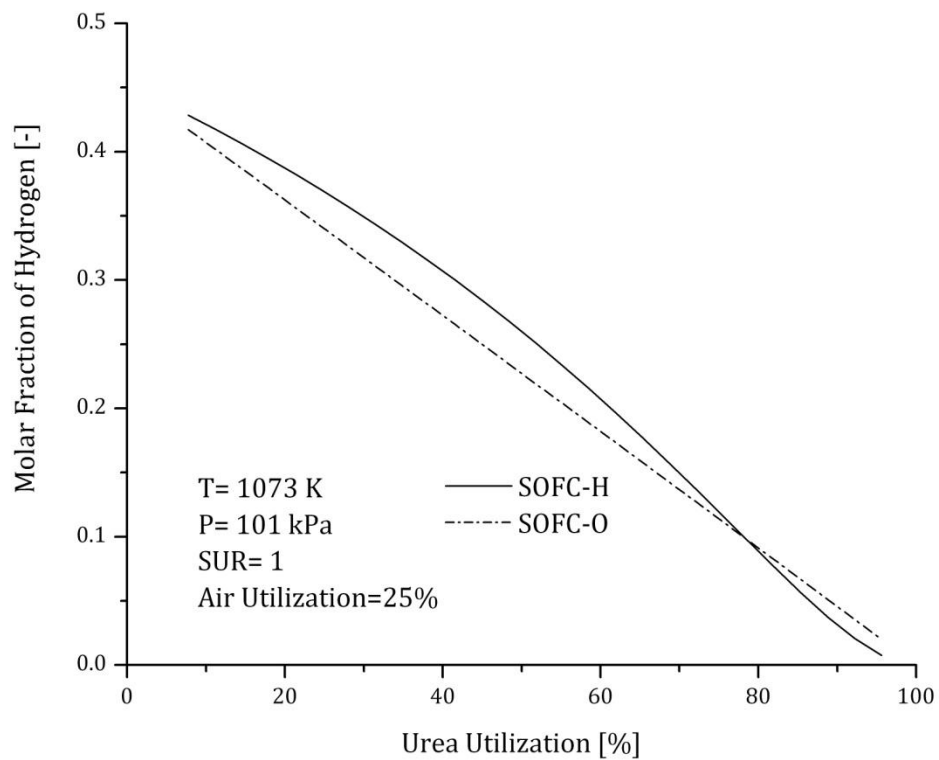


Figure 6.6: Molar fraction of hydrogen in DU-SOFC.

Figures 6.7 and 6.8 show that the molar fraction of water vapour at the cathode of SOFC-H is less than that at the anode of SOFC-O and the difference becomes larger at high fuel utilization. For SOFC-H, the constant molar fraction of water vapour is dependent on the invariant oxidant utilization.

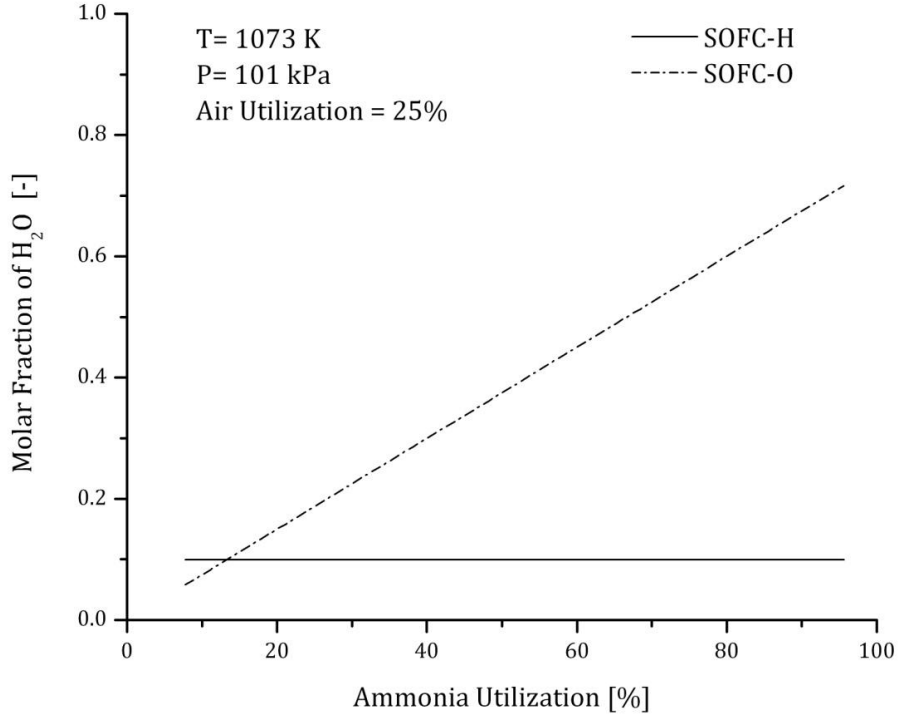


Figure 6.7: Molar fraction of water vapour in DA-SOFC.

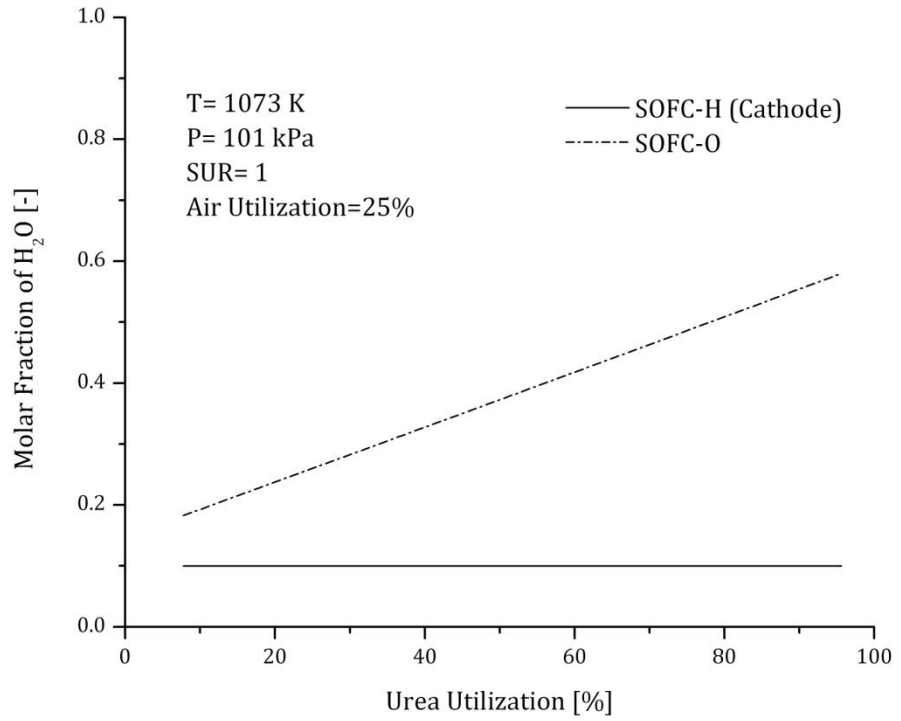


Figure 6.8: Molar fraction of water vapour in DU-SOFC.

Conversely, water vapour is produced in amounts equal to the hydrogen consumption at the anode of SOFC-O leading to an increase in its molar fraction at high fuel utilization. Figure 6.9 shows the OCV of the DA-SOFC as a function of fuel utilization. It is always desirable to have a high fuel utilization to maximize the system efficiency and avoid fuel combustion and its emissions in combustion chambers and after-burners. However, higher OCV value is a competing objective which tends to decline as the fuel utilization is increased. As a general trend, the OCV of SOFC-O is lower than that of SOFC-H and the difference becomes more pronounced at higher fuel utilizations due to the high rate of oxidation reaction and water vapour formation.

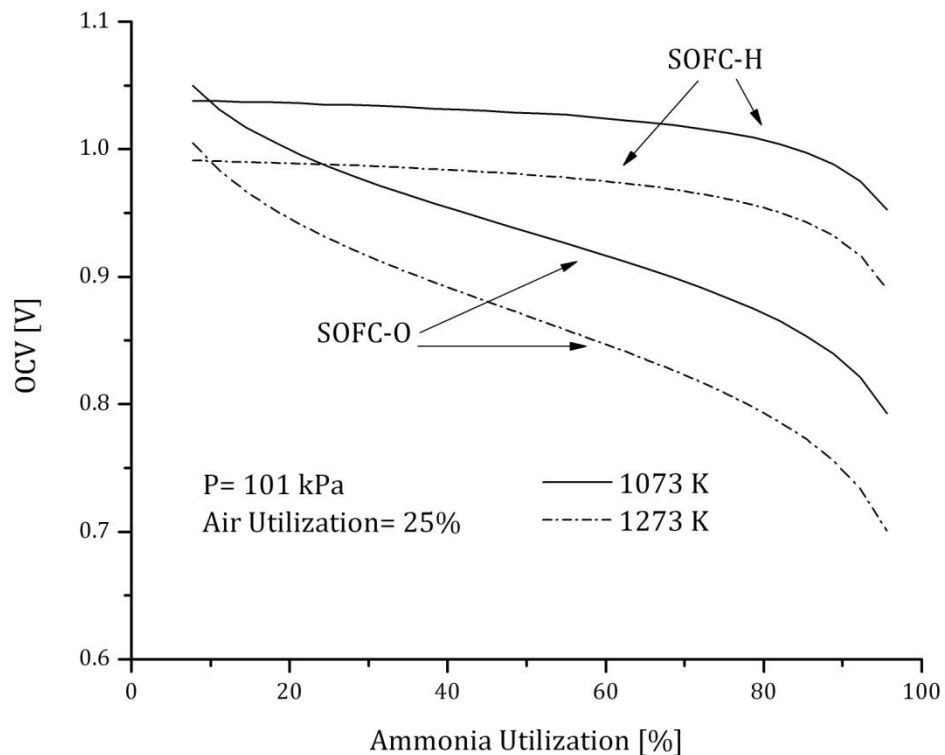


Figure 6.9: Open cell voltage of DA-SOFC at different temperatures.

As reflected in Figure 6.10, the results are consistent with the experimental findings for the SOFC fuelled with hydrogen or ammonia which show a decrease in OCV as the operating temperature of fuel cell increases.

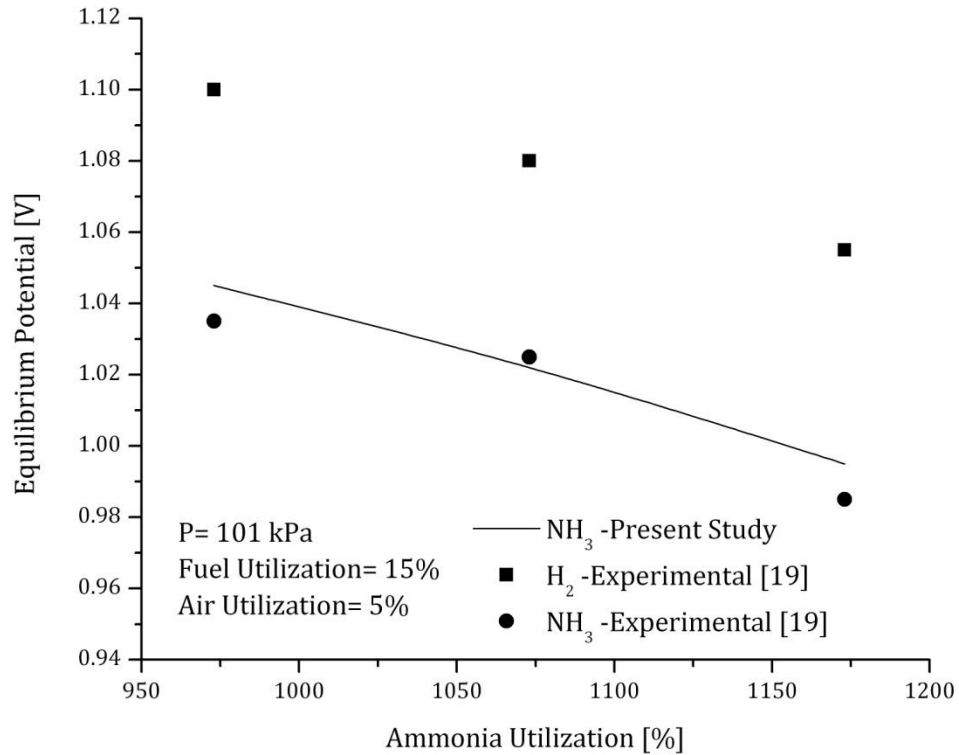


Figure 6.10: Comparison of predicted open cell voltage with experimental data (SOFC-O).

The OCV value of DU-SOFC is usually lower than that of DA-SOFC mainly due to the presence of additional chemical species like carbon dioxide and carbon monoxide which reduce the partial pressure of hydrogen. This is shown in Figure 6.11.

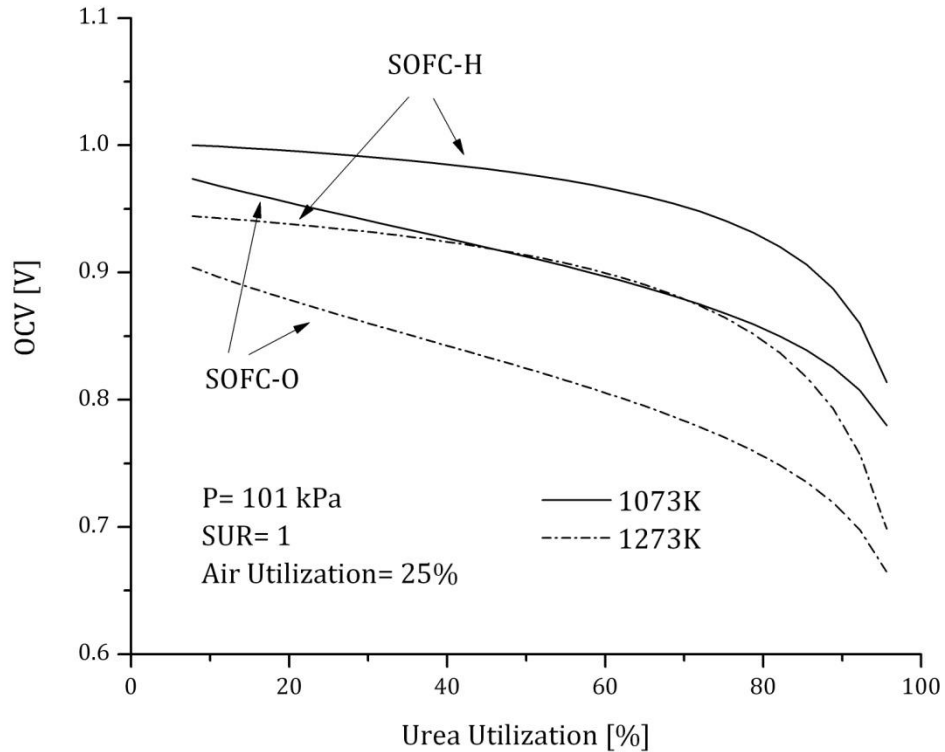


Figure 6.11: Open cell voltage of DU-SOFC at different temperatures.

Figures 6.12 and 6.13 indicate that the OCV of the respective types of SOFC can be improved by 5-6% when the operating pressure is increased by five times the atmospheric pressure. This modest enhancement is of particular benefit when SOFC is used in an integrated pressurized system. In addition, increasing the air utilization reduces the OCV of SOFC as shown in Figures 6.14 and 6.15. The deterioration is more pronounced in proton-conducting DA-SOFC and DU-SOFC due to higher partial pressure of water vapour and low partial pressure of oxygen at the cathode.

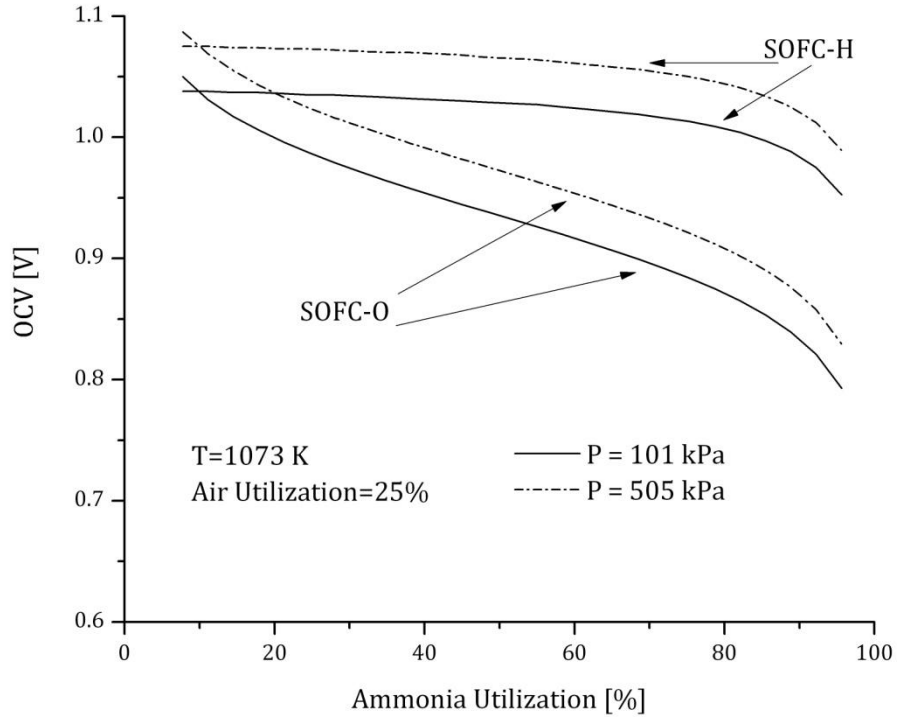


Figure 6.12: Effect of pressure on the open cell voltage of DA-SOFC.

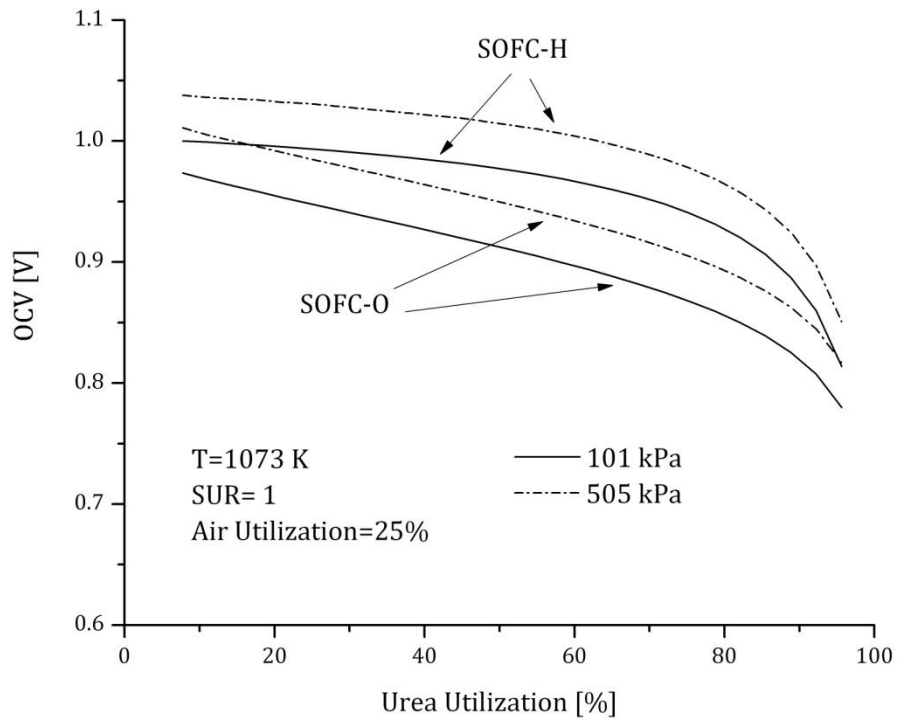


Figure 6.13: Effect of pressure on the open cell voltage of DU-SOFC.

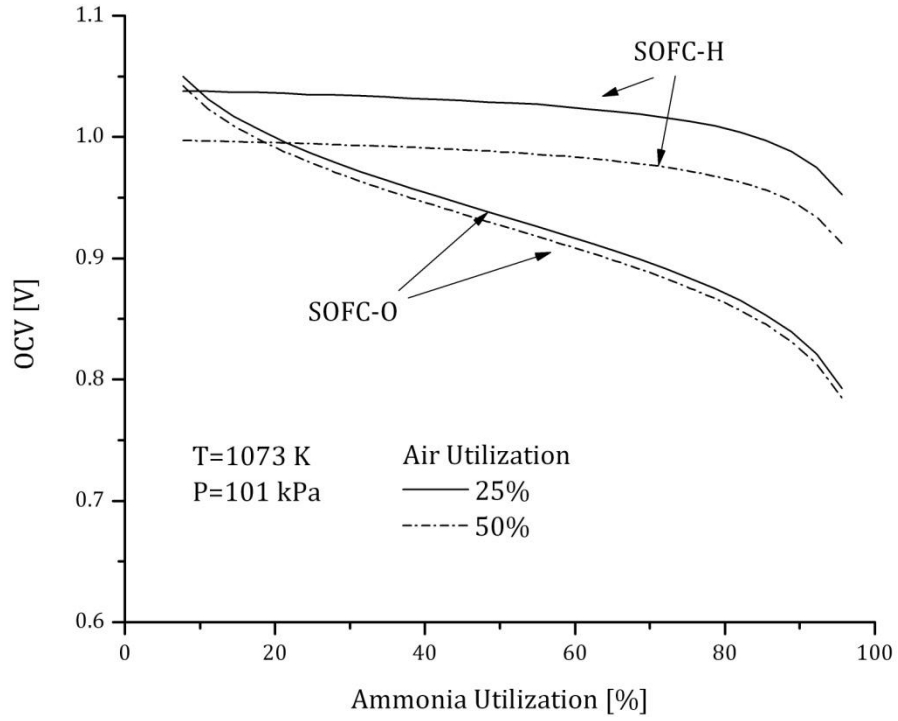


Figure 6.14: Effect of oxidant (air) utilization on the open cell voltage of DA-SOFC.

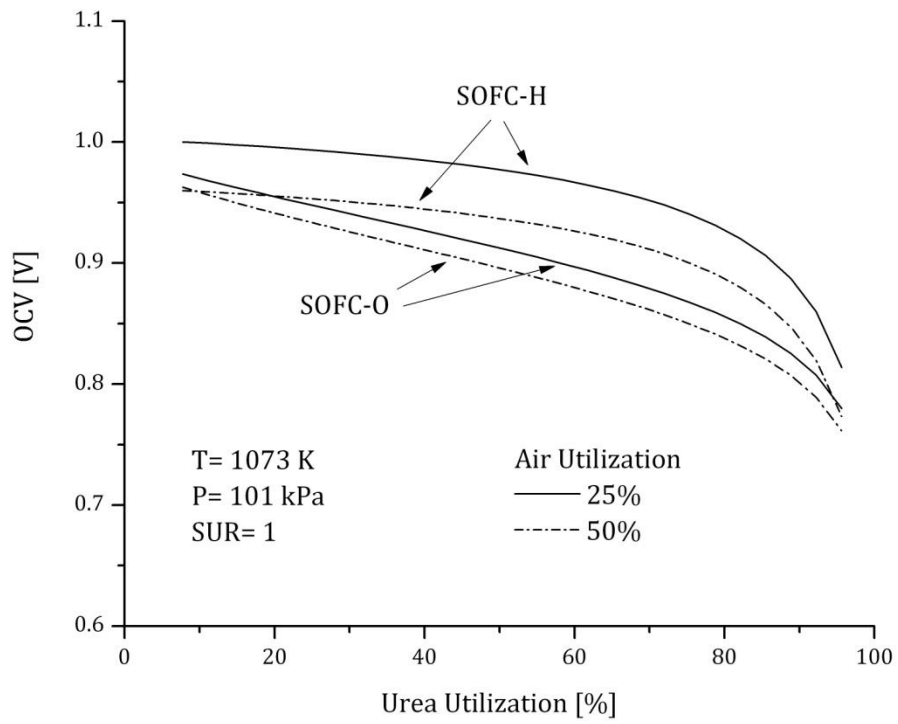


Figure 6.15: Effect of oxidant (air) utilization on the open cell voltage of DU-SOFC.

Finally, it is desirable to reduce the amount of water vapour used for the hydrolysis of urea. However, this is governed by several factors, most importantly is the extent of carbon formation and deposition. Figure 6.16 reports the effect of changing SUR on the OCV of proton-conducting DU-SOFC. Increasing SUR by two times has small negative effect on OCV; however, it is interesting to see a positive gain at higher fuel utilization (>70%) mainly because of RWGS reaction which tends to combine excess water vapour with carbon monoxide to produce hydrogen and carbon dioxide.

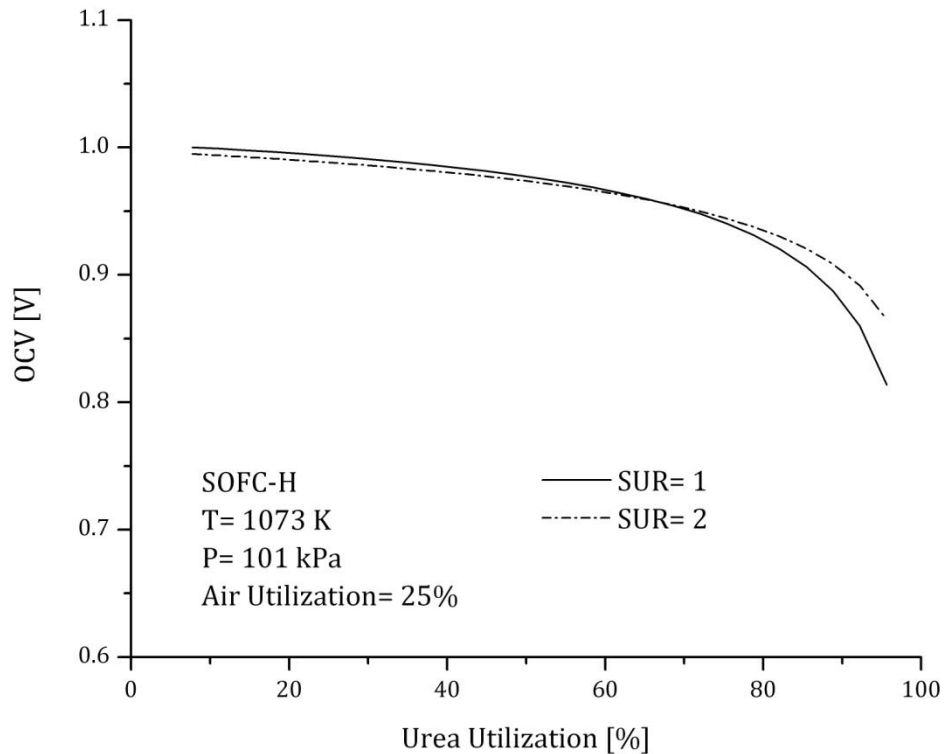


Figure 6.16: Effect of SUR on the open cell voltage of proton-conducting DU-SOFC.

Similarly, increasing SUR results in OCV drop for ion-conducting DU-SOFC as depicted in Figure 6.17. Nonetheless, this type of SOFC may benefit from reducing the water vapour content entering the anode by employing gradual internal

reforming similar to that employed for the internal reforming of methane [85,86]. With this method, a fraction of the water vapour generated from the electrochemical reaction at anode can be used in the hydrolysis process in a progressive manner along the length of the fuel cell resulting in OCV improvement. Careful implementation of this method is important to avoid localized carbon deposition on anode surface.

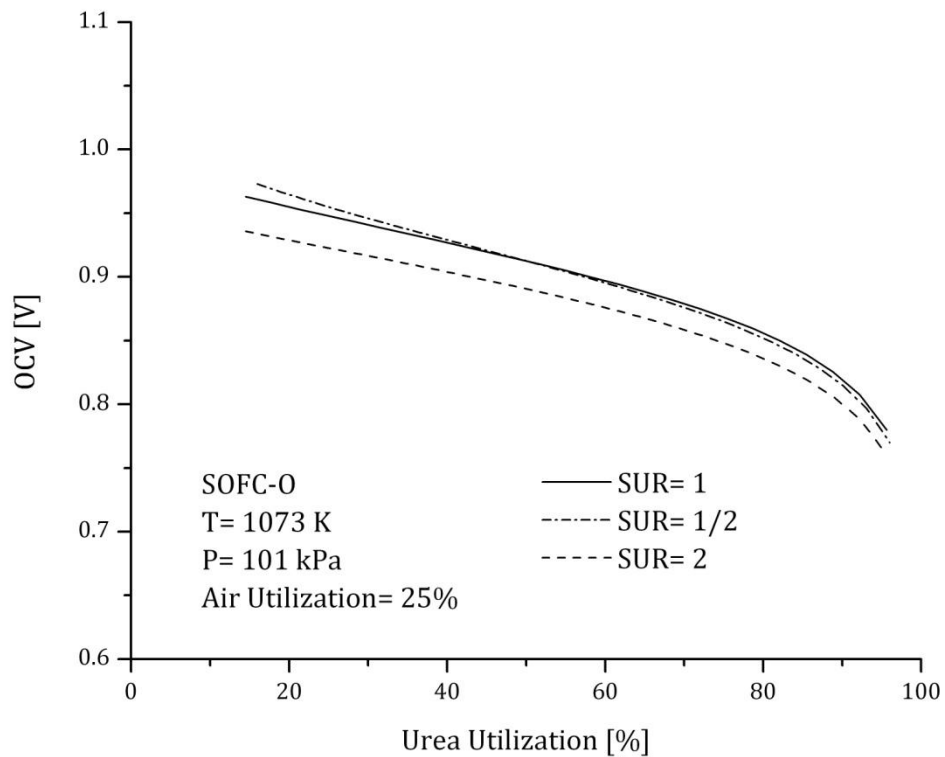


Figure 6.17: Effect of SUR on the open cell voltage of ion-conducting DU-SOFC.

6.3 Maximum Electrochemical Efficiency

Figures 6.18 and 6.19 show the maximum electrochemical efficiency of the respective fuel cells for a given fuel utilization. In general, the maximum efficiency of SOFC-H is higher than that of SOFC-O due to higher OCV over the range of fuel utilizations. Moreover, DA-SOFC is more efficient than DU-SOFC by 3-8% at high fuel utilization due to higher average molar fraction of hydrogen under most conditions. From the figures, it can also be seen that operating SOFC at higher pressure improves the OCV which in turn offers slight enhancement to the maximum electrochemical efficiency. The vertical dashed lines represent the maximum fuel utilization at which the maximum electrochemical efficiency can be achieved.

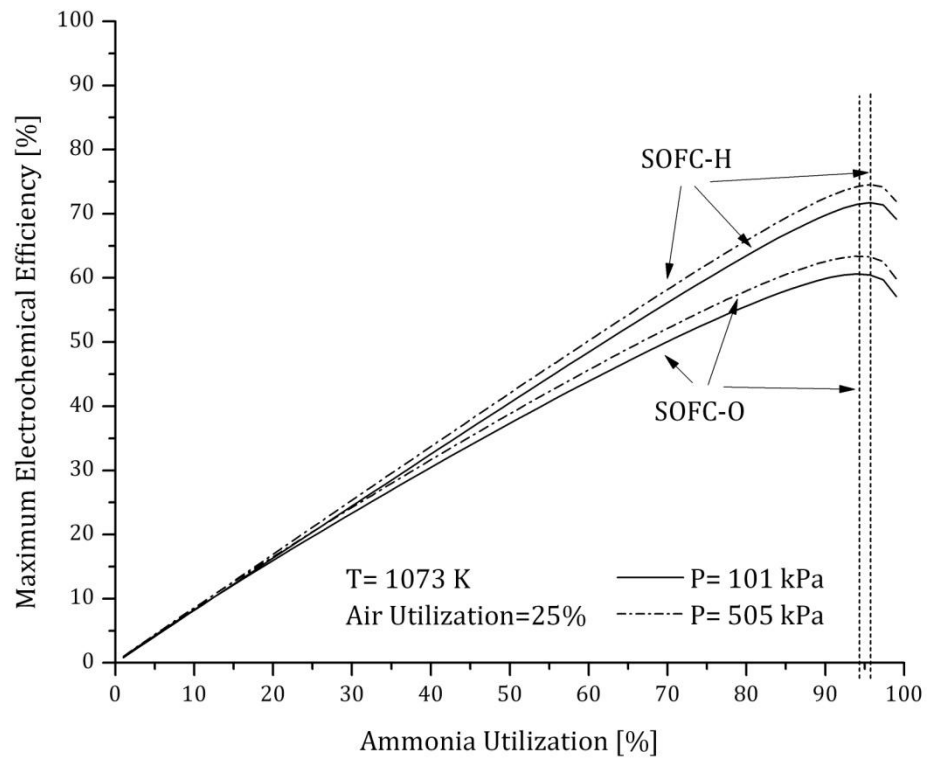


Figure 6.18: Maximum electrochemical efficiency of DA-SOFC.

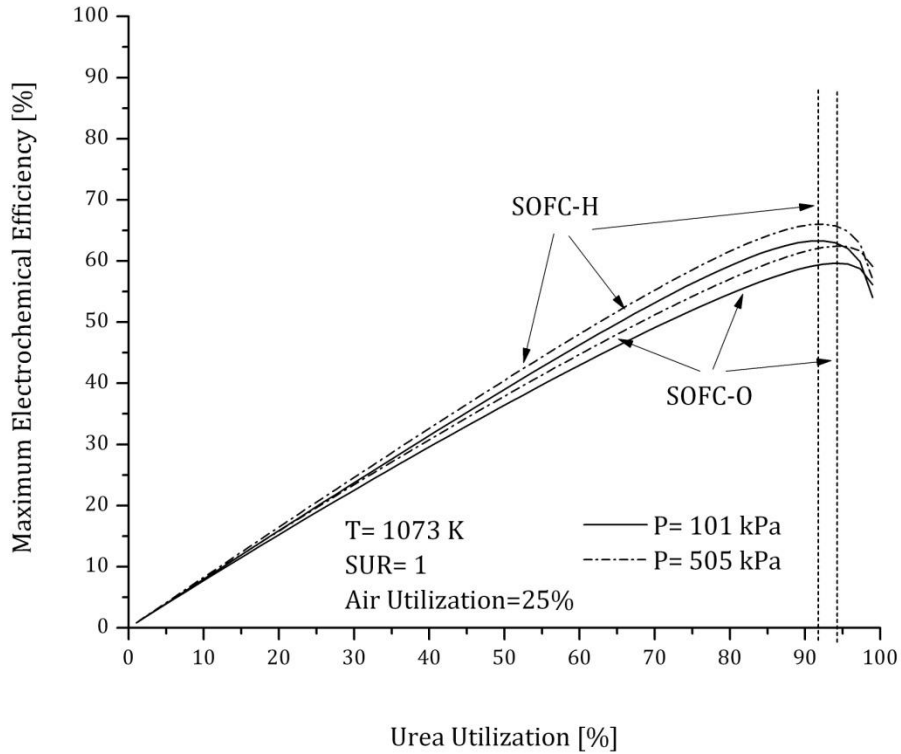


Figure 6.19: Maximum electrochemical efficiency of DU-SOFC.

6.4 Operational Voltage and Performance

6.4.1 Model Validation

In the open literature, experimental investigations on ammonia-fed solid oxide fuel cells are scarce and rarely contain all the necessary information and parameters for model evaluation. Therefore, certain assumptions were made and some model parameters were adjusted to be in agreement with the experimental data. In an experiment conducted by Ma et al. [8], ammonia was used as a fuel in anode-supported SOFC-O with the arrangement of Ni-YSZ|YSZ|LSM-YSZ. The cell was tested at atmospheric pressure and different temperatures of 923 - 1123K.

Table 6.1: Parameters used in the validation of ion-conducting DA-SOFC.

Parameters	Values
Operating temperature, T (K)	1123
Operating pressure, P (kPa)	101
Fuel Utilization, U_f (%)	5
Oxidant (air) Utilization, U_o (%)	5
Exchange current density of anode, J_{an} (A/m ²)	$7 \times 10^9 \left(\frac{P_{H_2}}{P^0}\right) \left(\frac{P_{H_2O}}{P^0}\right) \exp\left(-\frac{100000}{RT}\right)$
Exchange current density of cathode, J_{ca} (A/m ²)	$7 \times 10^9 \left(\frac{P_{O_2}}{P^0}\right)^{0.25} \exp\left(-\frac{130000}{RT}\right)$
Electrode porosity, ϵ	0.4
Electrode tortuosity, τ	4.25
Average pore radius of electrode, r_p (μm)	0.5
Resistivity of electrolyte, R_Ω ($\Omega\cdot\text{m}$)	0.735
Anode thickness, (μm)	500
Electrolyte thickness, (μm)	30
Cathode thickness, (μm)	10

Sources: [8,30,87,88].

The result in Figure 6.20 shows excellent agreement between the numerical simulation and the experimental data. As discussed by Ma et al., the performance of the cell is characterized by the high interfacial resistance which accounts for about 50% of the total resistance of the cell. The resistance of the electrolyte was also higher than expected at the same temperature as reported elsewhere [80,89]. In part, this can be attributed to the poor contact between the electrodes and the electrolyte as well as the microstructural properties of the cell components which are highly dependent on the processing method as discussed by Ringuede et al. [90].

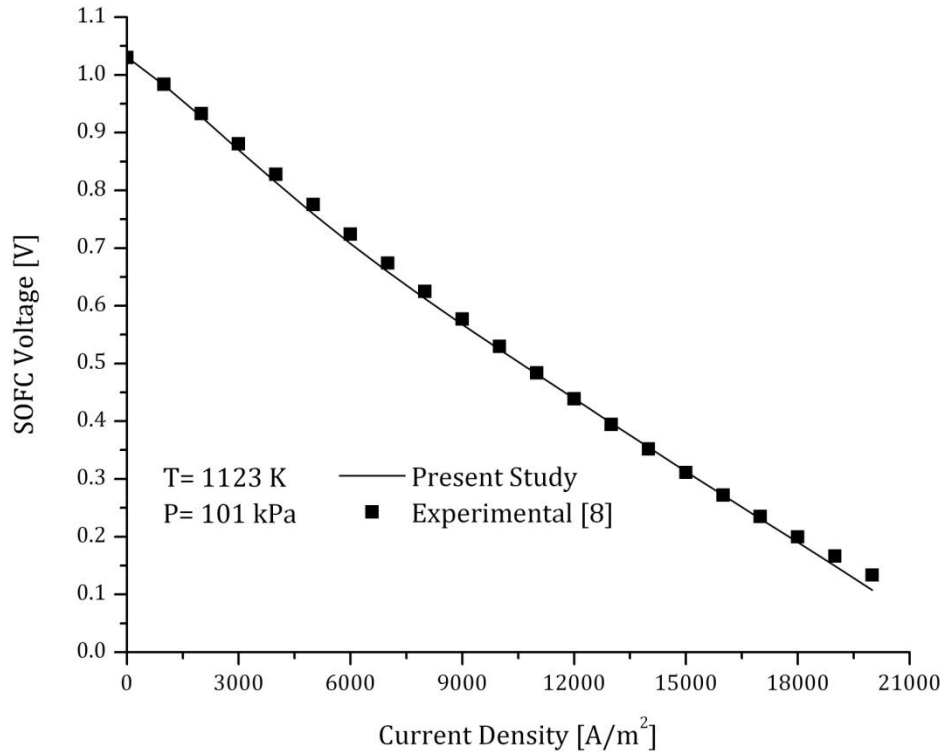


Figure 6.20: Comparison of simulation and experimental results of ammonia-fed SOFC-O.

There is a greater difficulty in obtaining sufficient experimental data to validate the numerical simulation for proton-conducting DA-SOFC. It should also be noted that, to the best knowledge of the author, there are no previous experimental investigations on urea-fed solid oxide fuel cells. Consequently, the model used for DA-SOFC and validated against available experimental data, will be extended to demonstrate the performance of DU-SOFC technology.

6.4.2 Ion and Proton-Conducting DA-SOFC

Certain modelling parameters have been fixed to establish a common basis of comparison. The parameters for ion and proton-conducting DA-SOFC are tabulated below.

Table 6.2: Parameters used in modelling the polarization curve of DA-SOFC.

Parameters	Values
Fuel utilization, U_f (%)	5
Oxidant utilization, U_o (%)	5
Exchange current density of anode SOFC-O, J_{an} (A/m ²)	$7 \times 10^9 \left(\frac{P_{H_2}}{P^0}\right) \left(\frac{P_{H_2O}}{P^0}\right) \exp\left(-\frac{100000}{RT}\right)$
Exchange current density of cathode SOFC-O, J_{ca} (A/m ²)	$7 \times 10^9 \left(\frac{P_{O_2}}{P^0}\right)^{0.25} \exp\left(-\frac{130000}{RT}\right)$
Exchange current density of anode SOFC-H, J_{an} (A/m ²)	2500@1073K 5000@1273K
Exchange current density of cathode SOFC-H, J_{ca} (A/m ²)	1700@1073K 3400@1273K
Electrode porosity, ϵ	0.4
Electrode tortuosity, τ	4.25
Average pore radius of electrode, r_p (μm)	0.5
Resistivity of electrolyte SOFC-O, R_Ω ($\Omega\cdot\text{m}$)	$2.94 \times 10^{-5} \exp\left(\frac{10350}{T}\right)$
Resistivity of electrolyte SOFC-H, R_Ω ($\Omega\cdot\text{m}$)	0.37@1073K 0.21@1273K
Anode thickness, (μm)	500
Electrolyte thickness, (μm)	30
Cathode thickness, (μm)	30

Sources: [8,21,30,87,88,89,91].

Figure 6.21 shows the polarization curve of DA-SOFC operating at 1073K and atmospheric pressure. It can be seen that a high current density can be achieved by employing an anode-supported arrangement of the fuel cell. This can effectively

decrease the ohmic overpotential by reducing the electrolyte thickness down to few microns. The peak power density of proton-conducting fuel cell is about 21% higher than that of the ion-conducting one. In addition, the voltage decreases rapidly for both types of fuel cells at high current densities due to the low concentrations of reactants at TPB.

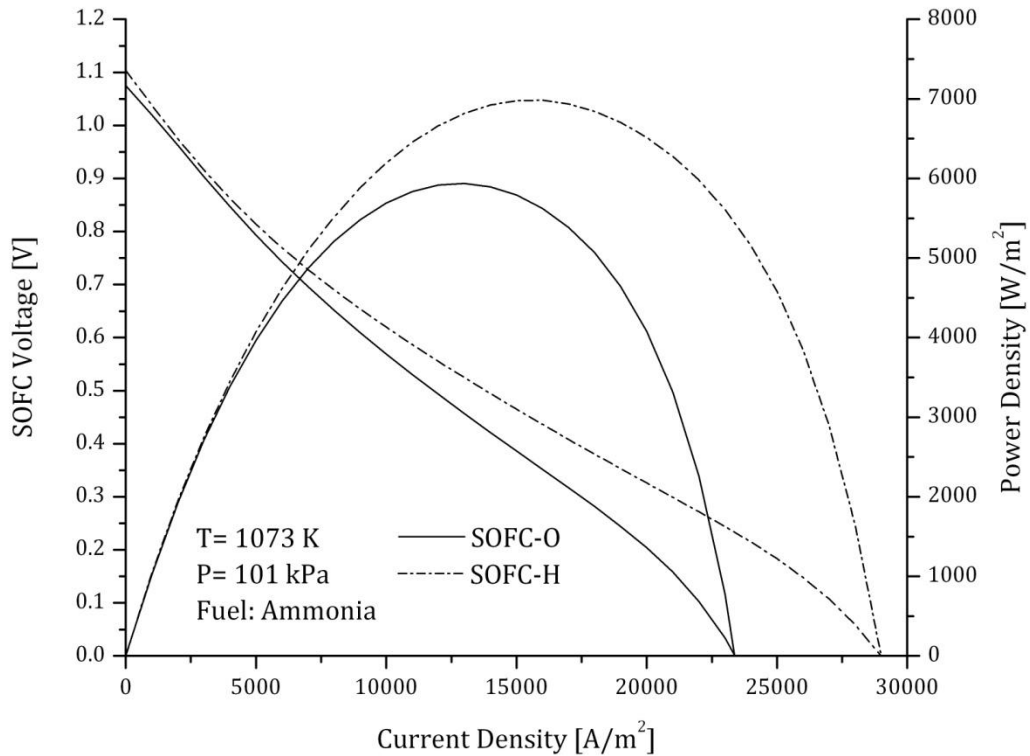


Figure 6.21: Polarization curve of DA-SOFC at 1073 K and atmospheric pressure.

As depicted in Figure 6.22, the activation overpotential of SOFC-O and SOFC-H anodes is comparable; however, it is rather higher at the cathode of SOFC-H in comparison to that at the cathode of SOFC-O. This is caused by the difference in

exchange current which is estimated to be about 2200 A/m² and 1700 A/m² for SOFC-O and SOFC-H respectively.

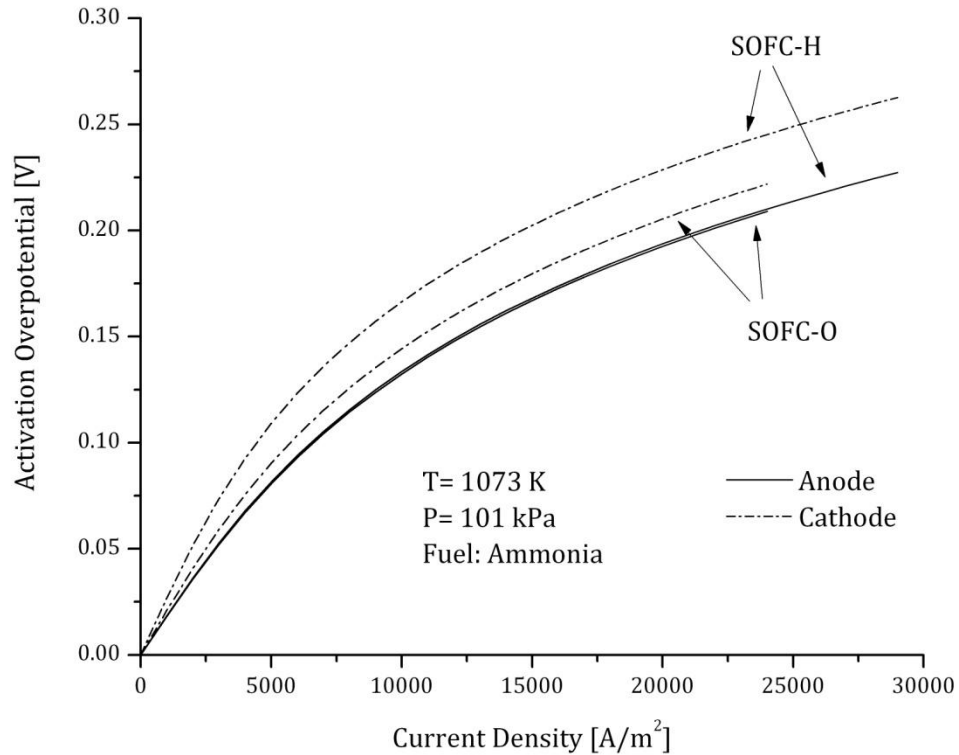


Figure 6.22: Activation overpotential of anode-supported DA-SOFC.

The effect of higher activation overpotential in SOFC-H is compensated by the low ohmic overpotential as shown in Figure 6.23. The resistivity (or ionic conductivity) of electrolyte is highly influenced by the chemical composition, processing method and sintering temperature [90,92]. The resistivity values used in this numerical study are 0.455Ω.m for ion-conducting electrolyte (YSZ) and 0.370Ω.m for proton-conducting (BCNO) electrolyte at 1073K and represent average values of what is found in the open literature.

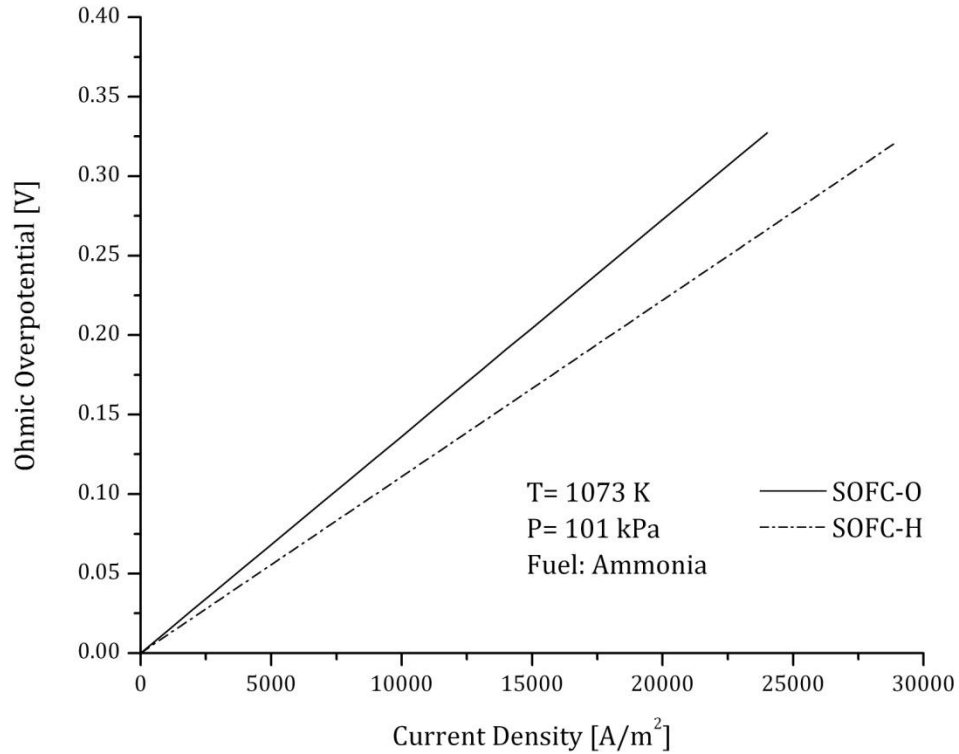


Figure 6.23: Ohmic overpotential of anode-supported DA-SOFC.

Figure 6.24 reflects the effect of concentration overpotential on the performance of anode-supported DA-SOFC. Due to the thickness of the anode, its concentration overpotential is significantly higher than that of the cathode. Moreover, the overpotential is more pronounced at the anode of SOFC-O due to the formation of water vapour at the anode-electrolyte interface and its diffusion through the porous anode into the gas channel.

The operating temperature has a major impact on the performance of the fuel cell. Figure 6.25 demonstrates the increase in power density despite the slight decrease in OCV as a result of increasing the temperature of DA-SOFC from 1073 to 1273K.

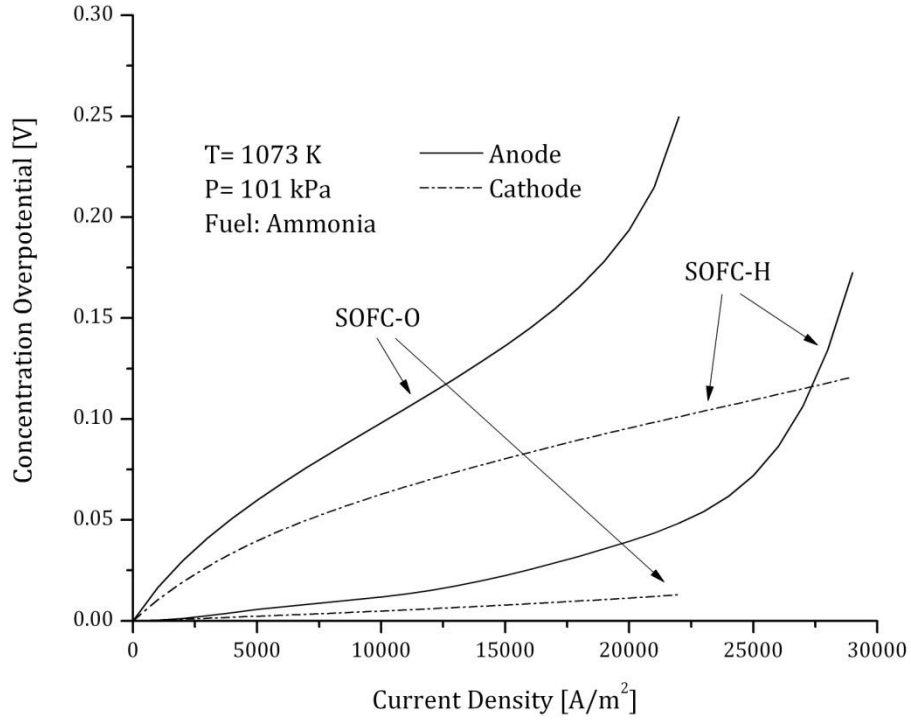


Figure 6.24: Concentration overpotential of anode-supported DA-SOFC.

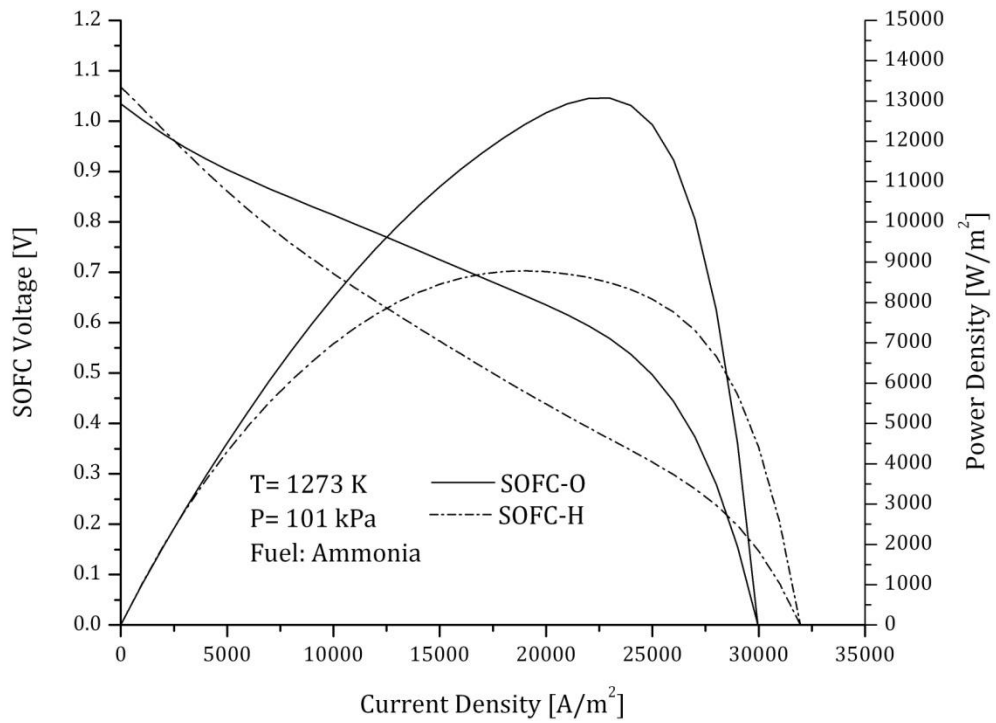


Figure 6.25: Polarization curve of DA-SOFC at 1273K and atmospheric pressure.

The higher operating voltage and current density is a result of lower overpotentials at high temperatures. The peak power density of SOFC-O is about 50% higher than that of SOFC-H. This is mainly due to the uncertainty in estimating the exchange current density of SOFC-H in contrast to the rate expression used for SOFC-O counterpart. Furthermore, this difference obtained here can be further justified by recognizing that the performance of proton-conducting solid oxide fuel cells deteriorates at elevated temperatures due to the high electronic conductivity of the electrolyte which is consistent with the information provided in the literature (e.g. [20,21]). Finally, increasing the operating pressure contributes to the improvement of the performance of DA-SOFC mainly by enhancing the permeation of gaseous species to and from reaction sites as shown in Figure 6.26.

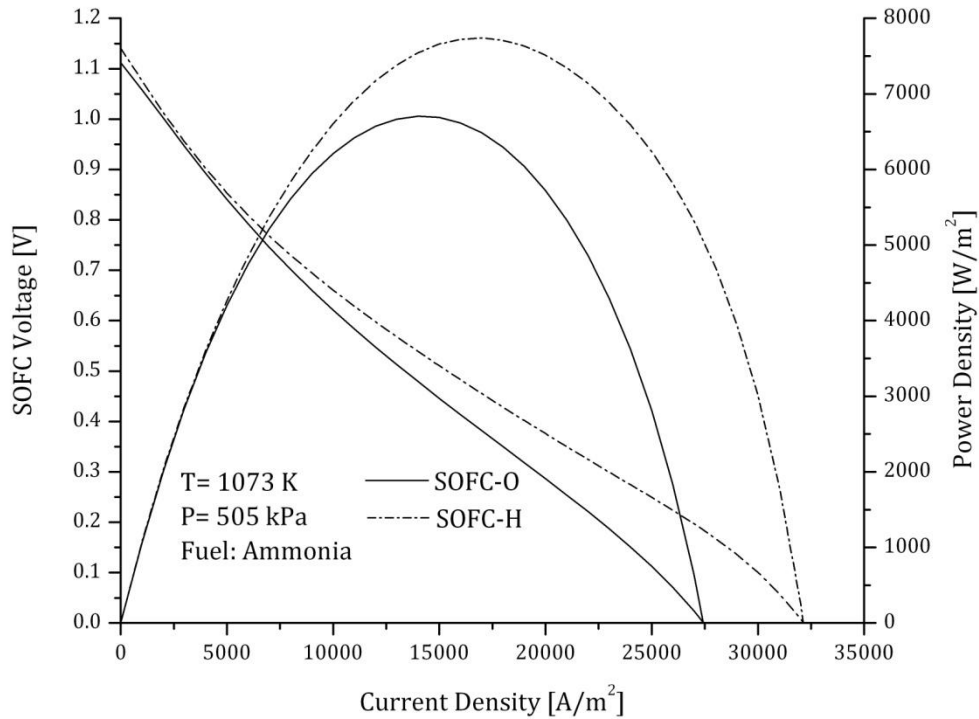


Figure 6.26: Polarization curve of DA-SOFC at 1073K and pressure of 505 kPa.

6.4.3 Ion and Proton-Conducting DU-SOFC

Similar to DA-SOFC, the parameters used for modelling the ion and proton-conducting DU-SOFC are tabulated below.

Table 6.3: Parameters used in modelling the polarization curve of DU-SOFC.

Parameters	Values
Fuel utilization, U_f (%)	5
Oxidant utilization, U_o (%)	5
Exchange current density of anode SOFC-O, J_{an} (A/m ²)	$7 \times 10^9 \left(\frac{P_{H_2}}{P^0}\right) \left(\frac{P_{H_2O}}{P^0}\right) \exp\left(-\frac{100000}{RT}\right)$
Exchange current density of cathode SOFC-O, J_{ca} (A/m ²)	$7 \times 10^9 \left(\frac{P_{O_2}}{P^0}\right)^{0.25} \exp\left(-\frac{130000}{RT}\right)$
Exchange current density of anode SOFC-H, J_{an} (A/m ²)	2500@1073K 5000@1273K
Exchange current density of cathode SOFC-H, J_{ca} (A/m ²)	1700@1073K 3400@1273K
Electrode porosity, ϵ	0.4
Electrode tortuosity, τ	4.25
Average pore radius of electrode, r_p (μm)	0.5
Resistivity of electrolyte (YSZ) SOFC-O, R_Ω ($\Omega\cdot\text{m}$)	$2.94 \times 10^{-5} \exp\left(\frac{10350}{T}\right)$
Resistivity of electrolyte (BCNO) SOFC-H, R_Ω ($\Omega\cdot\text{m}$)	0.37@1073K 0.21@1273K
Anode thickness, (μm)	500
Electrolyte thickness, (μm)	30
Cathode thickness, (μm)	30

Sources: [8,21,30,87,88,89,91].

A temperature of 1073K, atmospheric pressure and SUR of one are chosen for the base case shown in Figure 6.27. It is evident that SOFC-H still offers superior performance in comparison to SOFC-O at intermediate temperatures even when urea is used as a fuel. Comparing the figures of performance of DU-SOFC to that of

DA-SOFC shows a decrease of 10% in the case of SOFC-O and 20% in the case of SOFC-H. This can be explained by the lower concentration of hydrogen at the anode and manifested as high concentration overpotential as depicted in the same figure.

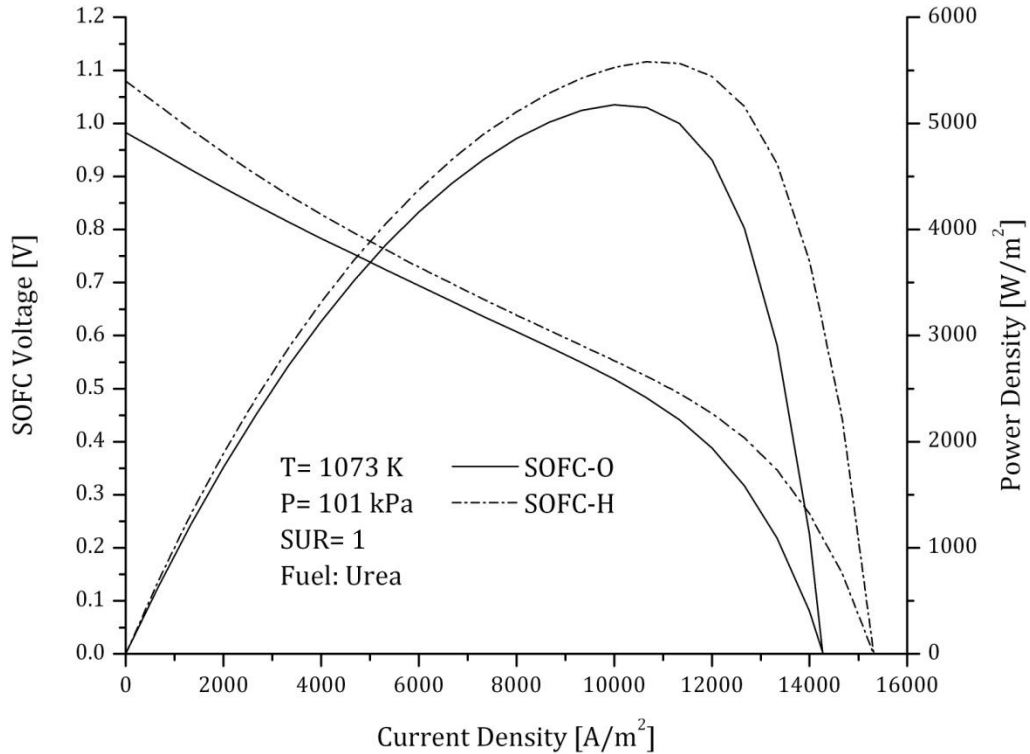


Figure 6.27: Polarization curve of DU-SOFC at 1073K and atmospheric pressure.

As shown in Figure 6.28, the activation overpotential of SOFC-H is higher than that of the SOFC-O due to the difference in the values of exchange current density. The ohmic overpotential shown in Figure 6.29 reflects the higher ionic conductivity of BCNO electrolyte in comparison to that of YSZ electrolyte at 1073 K. The negative effects of ohmic overpotential on the cell performance can be alleviated by altering the chemical composition and properties of the electrolyte.

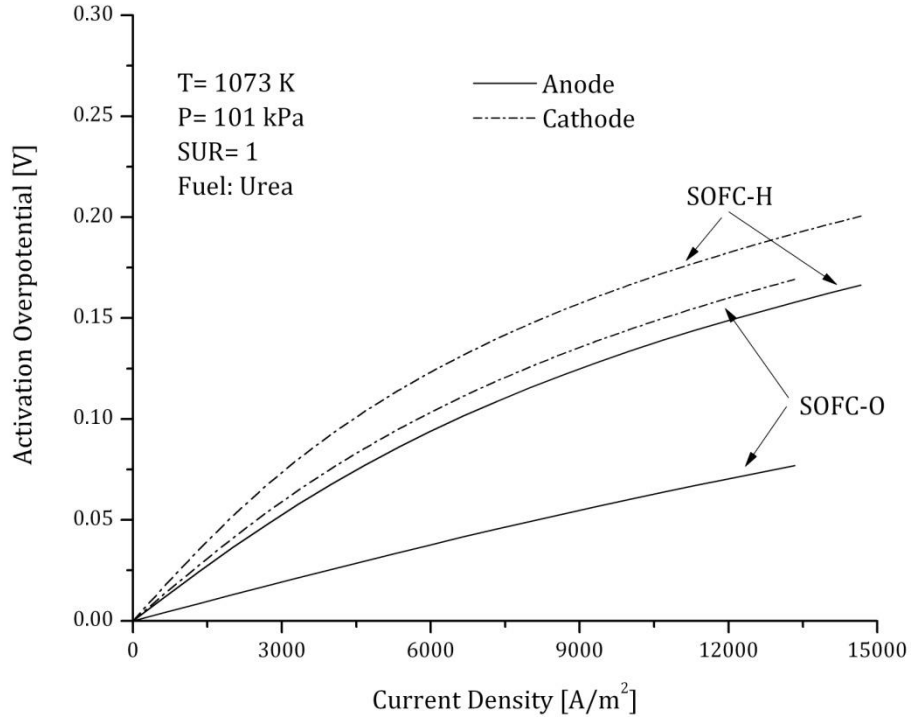


Figure 6.28: Activation overpotential of anode-supported DU-SOFC.

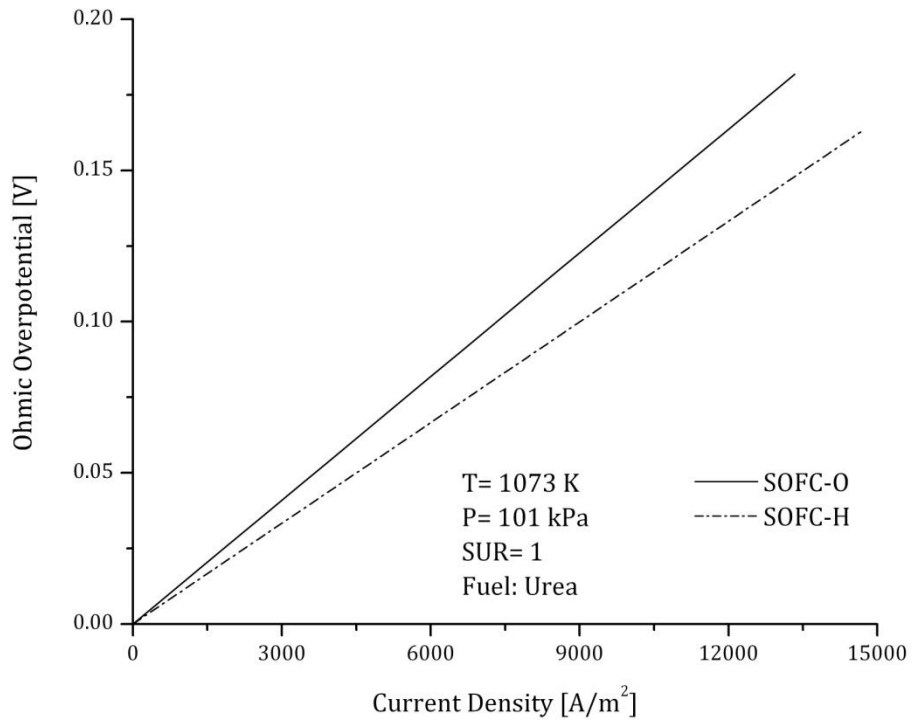


Figure 6.29: Ohmic overpotential of anode-supported DU-SOFC.

The performance of DU-SOFC is dominated by concentration overpotential as shown in Figure 6.30. The high overpotential at the anodes of SOFC-O and SOFC-H signifies the dilute concentration of hydrogen due to the presence of other chemical species such as carbon dioxide, carbon monoxide, nitrogen and water vapour. The diluents may be actively removed from the anode during operation; however, such provision can potentially add to the design complexity and cost of DU-SOFC.

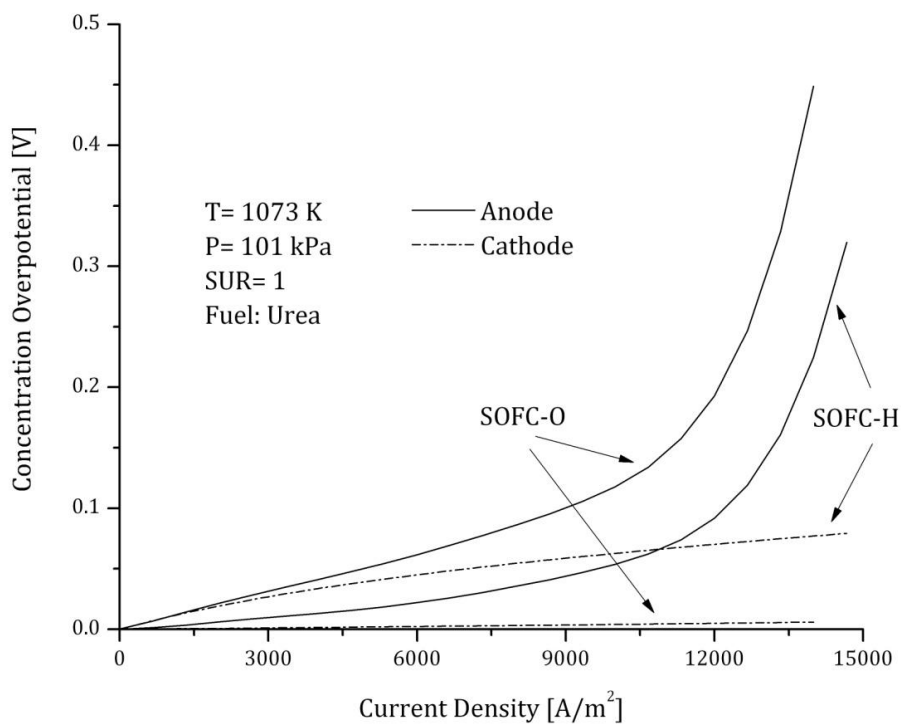


Figure 6.30: Concentration overpotential of anode-supported DU-SOFC.

Similar to DA-SOFC, increasing the operating temperature offers significant improvement of the performance of DU-SOFC as demonstrated in Figure 6.31. Although the activation and ohmic overpotentials are drastically reduced, the

polarization curves of SOFC-O and SOFC-H are still dominated by the concentration overpotential at high current densities.

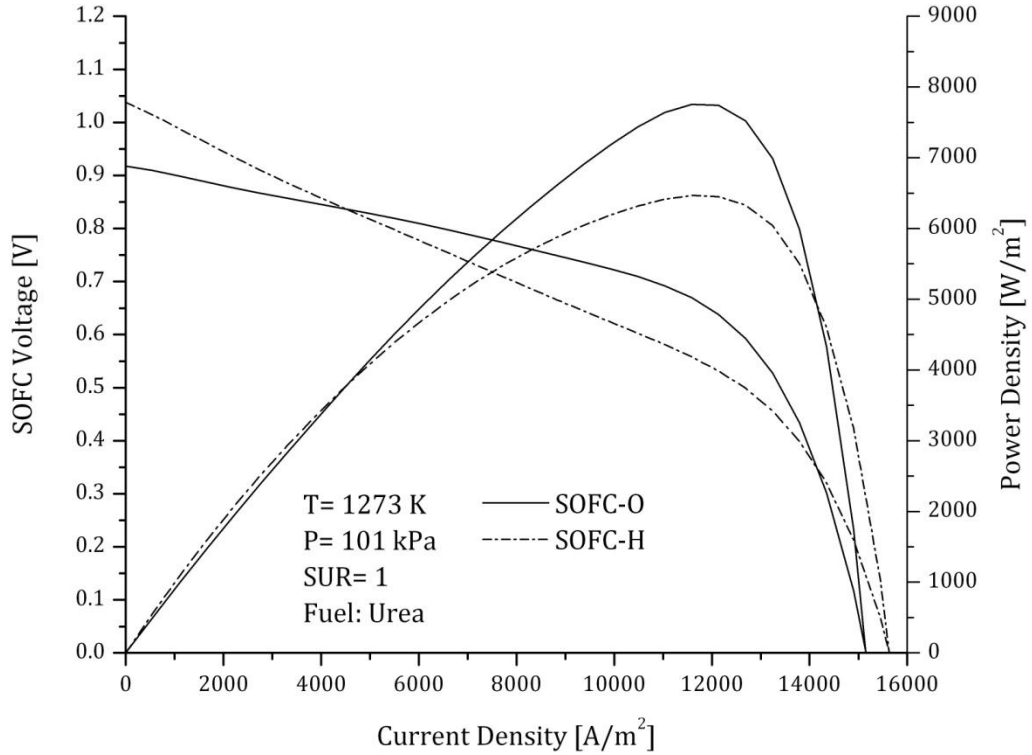


Figure 6.31: Polarization curve of DU-SOFC at 1273K and atmospheric pressure.

Furthermore, the performance can also be improved by increasing the operating pressure of DU-SOFC as shown in Figure 6.32. The enhancement is mainly manifested in increasing the open cell voltage and reducing the concentration overpotential and represents about 13-15% increase at peak power density in comparison to the base case.

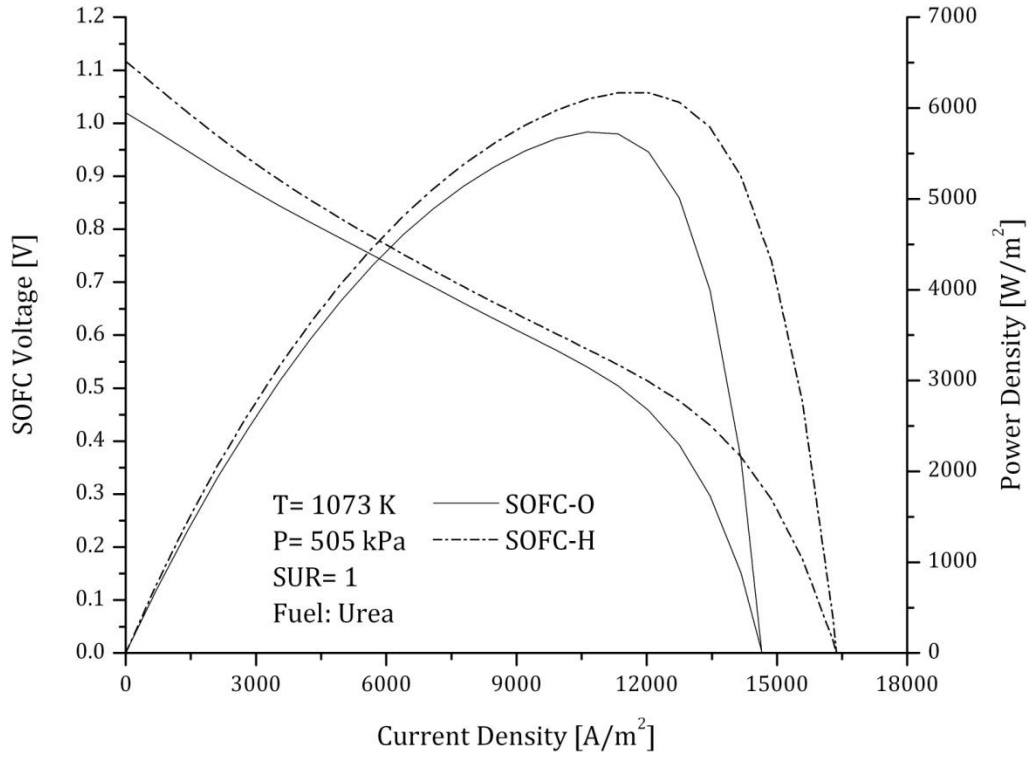


Figure 6.32: Polarization curve of DU-SOFC at 1073K and pressure of 505 kPa.

From the foregoing discussion, it can be concluded that the performance of DA-SOFC is superior to that of DU-SOFC under all operating conditions examined in this study. However, further analysis and modelling are required to provide better understanding of the thermodynamic and electrochemical processes of DA-SOFC and especially DU-SOFC as well as ways to improve their performance.

6.5 Integrated Systems

6.5.1 Ammonia-fed SOFC/GT system

The analysis which was presented in the previous sections assumed low utilization factor of reactants. For practical systems, it is desired to operate at the highest possible utilization factor while maintaining reasonable concentration of reactants and performance of the fuel cell. This value may vary between 80-95% for fuels and 20-35% for oxidants. Table 6.4 reflects the parameters used for the analysis of the base case study.

Table 6.4: Main parameters used for the base case study of DA-SOFC/GT system.

Fuel utilization factor, U_f [%]	85
Oxidant utilization factor, U_o [%]	25
Stack temperature, T_{FC} [K]	1073
Stack Pressure, P_{FC} [kPa]	505
Pressure Ratio, PR	5
Cumulative cell area, A_{FC} [m ²]	250
Compressor efficiency, $\eta_{s,c}$ [%]	85
Turbine efficiency, $\eta_{s,t}$ [%]	90
Heat exchanger effectiveness, ξ [%]	90
AC generator efficiency, η_G [%]	95
DC/AC inverter, η_{INV} [%]	98
Ambient temperature, T_{amb} [K]	298
Ambient pressure, P_{amb} [kPa]	101.3
Molar composition of oxygen in air, [%]	21
Molar composition of nitrogen in air, [%]	79

The polarization curve of DA-SOFC is shown in Figure 6.33. The peak power densities are 1875 W/m² at 0.67 V for SOFC-O and 4507 W/m² at 0.58 V for SOFC-H.

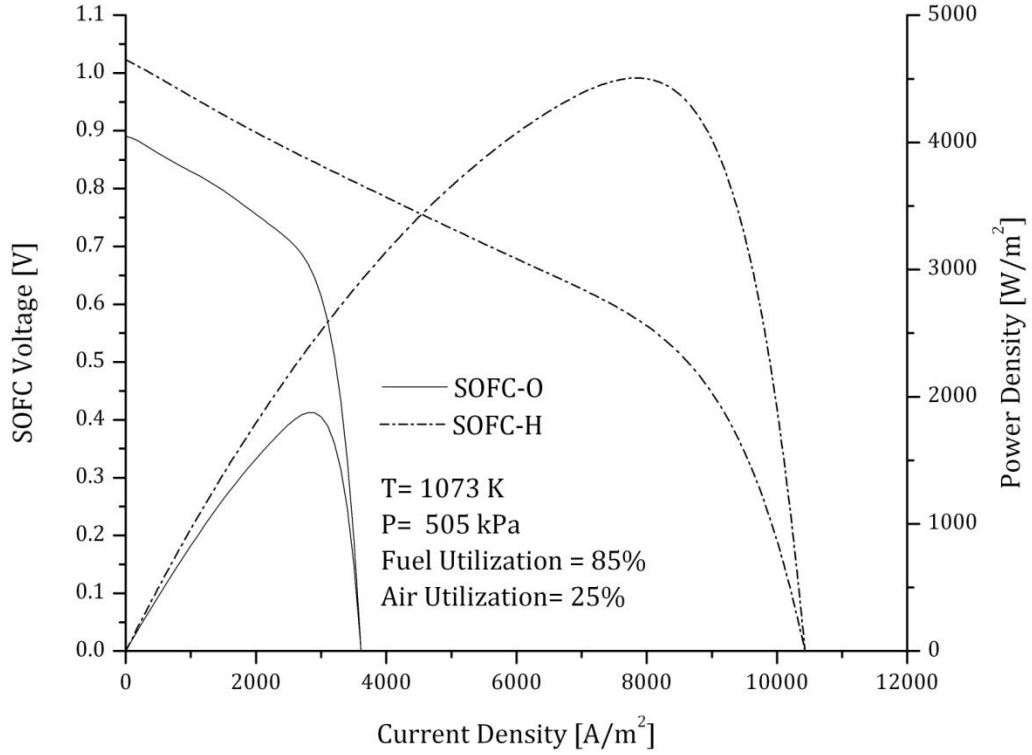


Figure 6.33: Polarization curve of ion and proton-conducting DA-SOFC (base case).

The significant difference of 144% (based on peak power density) is mainly due to the higher concentration of hydrogen at the anode of SOFC-H compared to that at the anode SOFC-O. This is reflected by the difference in the open cell voltage as well as the detrimental impact of the concentration polarization which is most pronounced in the case of SOFC-O. Moreover, the overall arrangement of system components, the heating requirements for the reactants and the thermolysis of ammonia prevented the operation of the respective fuel cell at any voltage equal or higher than that corresponding to the peak power density. In order to satisfy such requirements, the respective fuel cell is operated at a reduced voltage as shown in Table 6.5. The temperature distribution of the system is depicted in Figure 6.34.

Table 6.5: Operating voltage and current density of DA-SOFC/GT system at different conditions.

Fuel Cell	SOFC-O		SOFC-H	
Parameters	V [V]	J [A/m ²]	V [V]	J [A/m ²]
Base Case	0.52	3185	0.59	7640
T _{FC} = 1173K	0.44	3545	0.52	7935
T _{FC} = 1273K	0.36	3440	0.45	8200
U _f = 0.90	0.48	2190	0.55	6325
U _f = 0.95	0.43	1075	0.51	3670
PR= 2.5	0.69	2500	0.76	4110
PR= 7.5	0.44	3300	0.51	8650

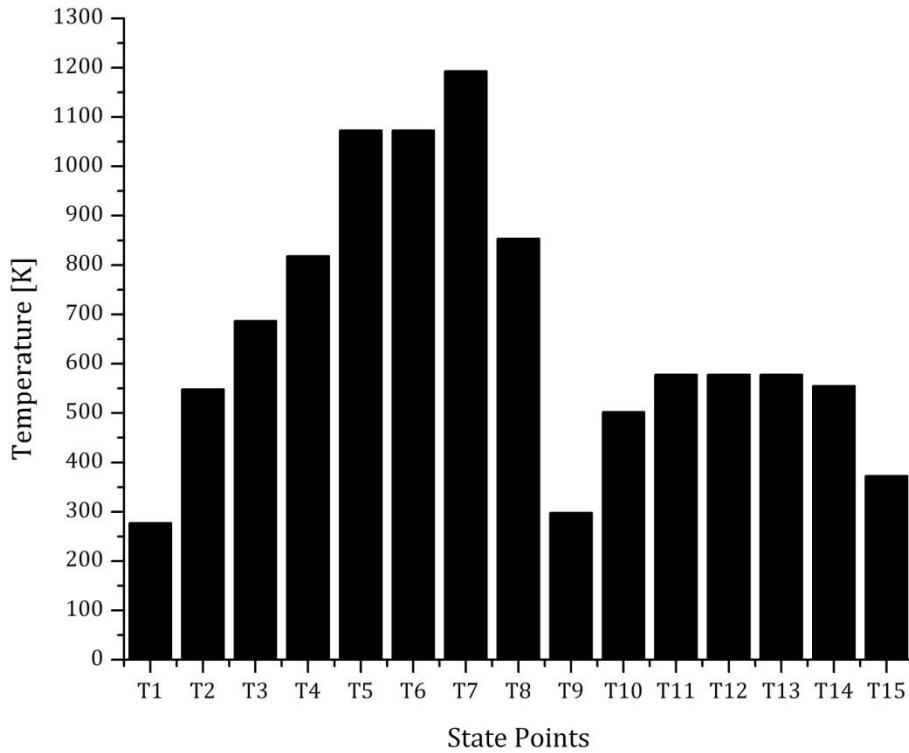


Figure 6.34: Temperature distribution of ion and proton-conducting DA-SOFC/GT system (base case).

The state points shown in Figure 6.34 correspond to those in Figure 4.5. For the base case study, the temperature of the fuel cell effluents is 1073K (T5 and T6) and increases to 1193K (T7) in the combustion chamber during the adiabatic

combustion of the unused hydrogen. The hot exhaust gases enter the turbine and expand to produce mechanical work and exits the turbine at 853K (T8). At that point, the exhaust manifold splits to two branches to deliver heating gas steams to the fuel and air heat exchangers. The difference of 130K between the temperature of the anode (T3) and the cathode (T4) inlets may potentially cause mechanical stresses which can lead to problems with sealing, leakage and cracking of ceramic components. The temperature mismatch can be explained by realizing that 95% of the turbine exhaust volume is diverted to heat exchanger (HX3) through branch (8a) in order to satisfy the high requirements for heating the incoming air. This also results in a low heat transfer rate in (HX2) which cannot raise the temperature of the fuel to match that of the air entering the cell.

In order to maintain the pressure of ammonia exiting the tank at 505kPa (with a saturation temperature of 277.3K), heat is rejected from the closed-loop coil located in the tank at a rate of 46.7 kJ/mol of ammonia which produces a cooling effect in the fluid passing through the coil. The effectiveness of this process is about 14.7% based on the LHV of ammonia.

In addition, the total specific electric power generated by the system with SOFC-H option is about 8% higher than that of the system with SOFC-O as given in Table 6.6. The difference corresponds to the lower exergy destruction in the system with SOFC-H option due to reduced thermodynamic irreversibilities. The tabulated data also reveal that more than 62% of the total power is delivered by the fuel cell stacks.

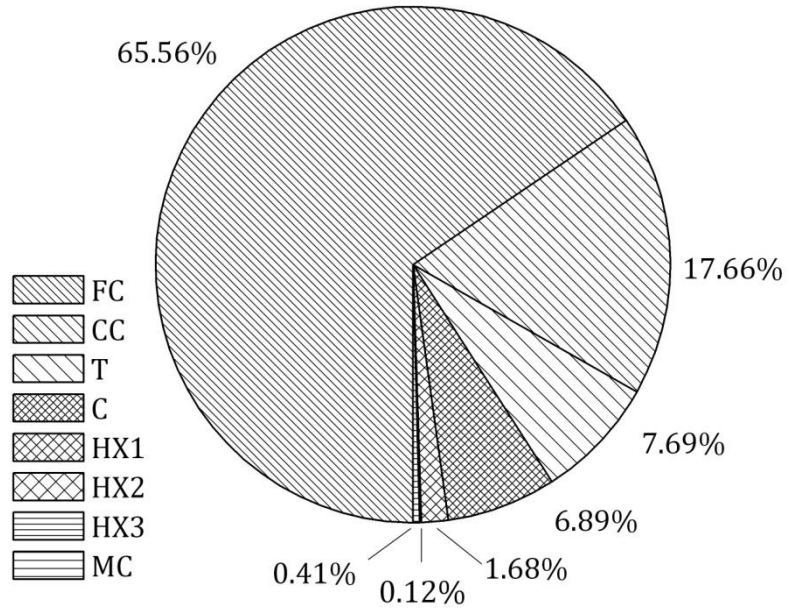
This reasonable performance can be further improved by reducing the exergy destruction in the fuel cell.

Table 6.6: Specific power and exergy destruction in kJ/mol of fuel for DA-SOFC/GT system (base case).

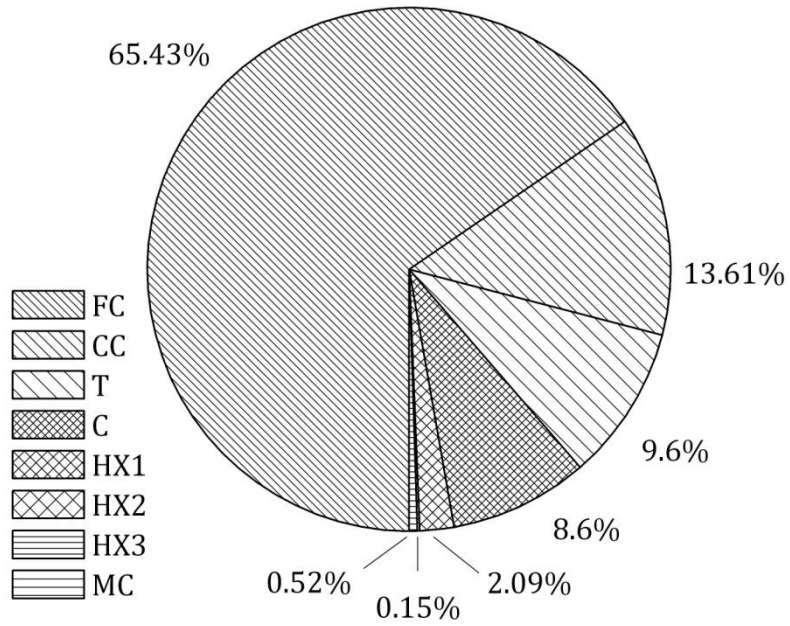
Type of Fuel Cell		SOFC-O	SOFC-H
Overall System	Total specific power [kJ/mol]	203.6	219.5
	Total exergy destruction [kJ/mol]	100.0	83.5
Components	Specific power of fuel cell [kJ/mol]	126.0	141.9
	Specific power of electric generator [kJ/mol]	77.6	77.6

Figure 6.35 shows the exergy destruction within a component as a percentage of the total exergy destruction of the plant. It can be seen that the distribution of exergy destruction is similar both systems. The largest exergy destruction takes place in the fuel cell stacks due to the internal losses manifested as voltage overpotentials as well as external losses due to the large temperature difference between the stacks and its surroundings. Thus, the figure reiterates that efforts should be focused on high exergy destruction sites like the fuel cell module to minimize its thermodynamic irreversibilities and achieve maximum performance. Furthermore, good agreement between the temperatures at branches 11 and 12 results in negligible exergy destruction in the mixing chamber.

The first and second law efficiencies of the base case study are listed in Table 6.7. The data reveals the superiority of the system with SOFC-H option mainly due to the higher exergy efficiency of SOFC-H when compared to that of SOFC-O. This difference is expected since SOFC-H is characterized by its lower ohmic and concentration polarizations as discussed earlier.



(a) SOFC-O



(b) SOFC-H

Figure 6.35: The distribution of exergy destruction of DA-SOFC/GT system by component (base case).

Table 6.7: Energy and exergy efficiency of DA-SOFC/GT system (base case).

Type of Fuel Cell		SOFC-O	SOFC-H
Overall System	η_{total}	76.7	81.1
	ψ_{total}	69.9	74.3
	η_e	64.3	69.3
	ψ_e	60.2	65.0
Components	ψ_{FC}	66.7	76.6
	ψ_{CC}	93.6	96.0
	ψ_T	95.1	95.1
	ψ_C	90.2	90.2
	ψ_{HX1}	61.2	61.2
	ψ_{HX2}	96.4	96.4
	ψ_{HX3}	99.3	99.3

- **Effect of Reference State**

Exergy is a property of the system and its environment. Figure 6.36 depicts the effect of changing the reference temperature on the exergy efficiency of the integrated systems. While the effect is negligible on the exergy efficiency based on electric power production, the total exergy efficiency suffers minor drop over the studied range. The decrease of efficiency is proportional to the decrease in exergy associated with the heat recovered at the recuperator. This exergy is governed by a factor that corresponds to efficiency of a Carnot engine operating between the temperature of the gaseous stream and the reference temperature. Hence, increasing the reference temperature reduced the amount of useful work obtained from the heat recovery process and leads to lower total exergy efficiency.

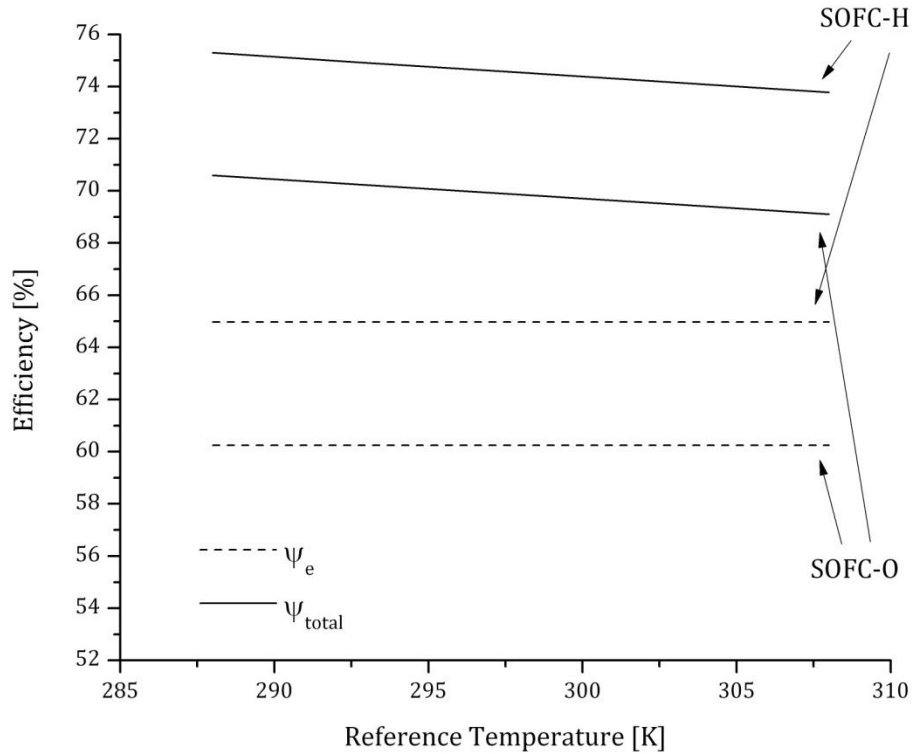


Figure 6.36: Effect of reference temperature on the exergy efficiency of DA-SOFC/GT system (base case).

▪ Effect of Ammonia Utilization

As mentioned earlier, it is desirable to achieve the highest possible fuel utilization in the fuel cell. Figure 6.37 reflects the effect of increasing the ammonia utilization in the fuel cell module on the total specific power of the plant and the back work ratio of the gas turbine-compressor assembly. Although the system with SOFC-H benefits from higher specific power in comparison to the one with SOFC-O, both systems experience considerable drop in specific power as the fuel utilization increases. The contributing factors include lower open cell voltage and higher concentration overpotential at high fuel utilizations. For reference, selected values are listed in Table 6.5 that shows the impact of increasing the fuel utilization on the operational

voltage and current densities of the fuel cells. The back work ratio is identical for both systems. Increasing the fuel utilization lowers the molar flow rate of the gaseous mixture entering the gas turbine and reduces its power production. However, the required compressor power is also reduced in different proportion leading to a slight increase in the back work ratio.

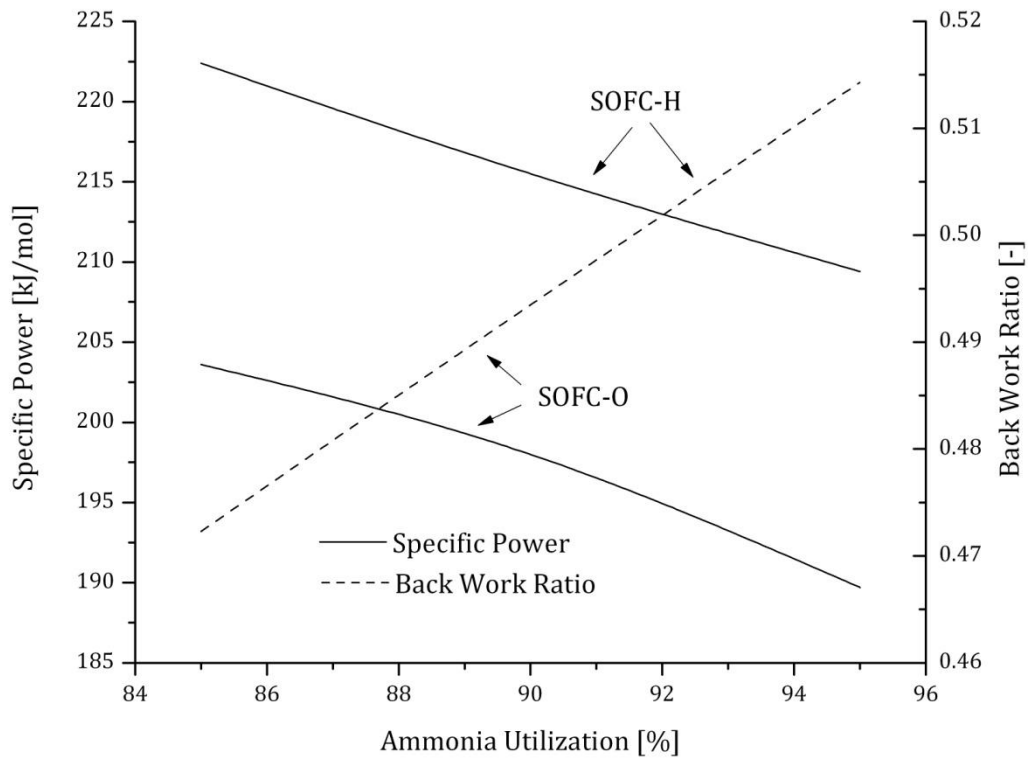
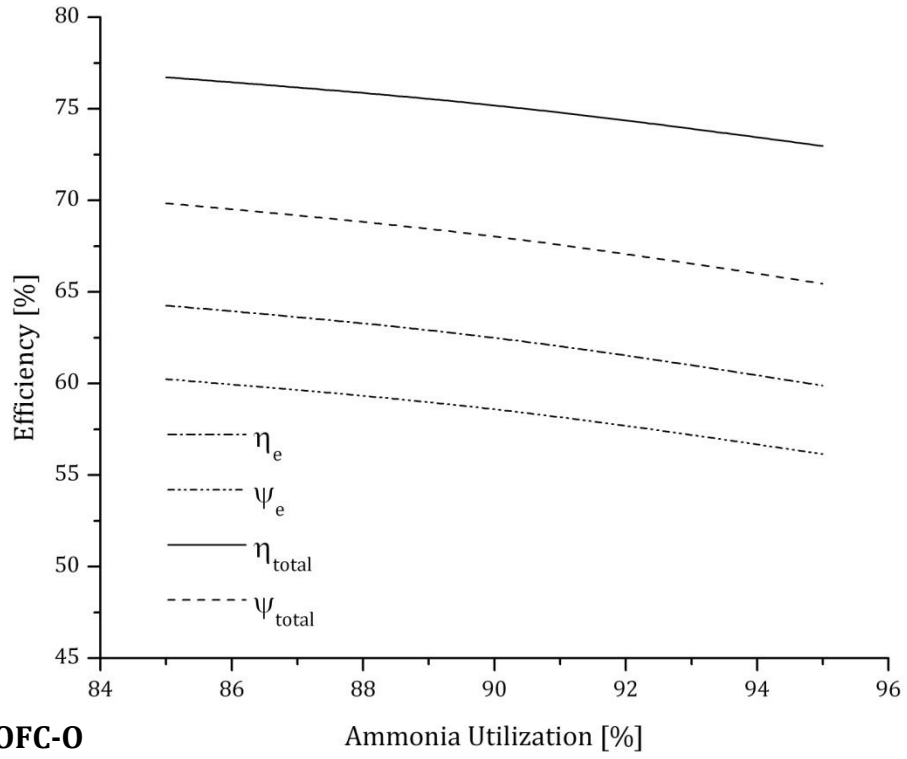
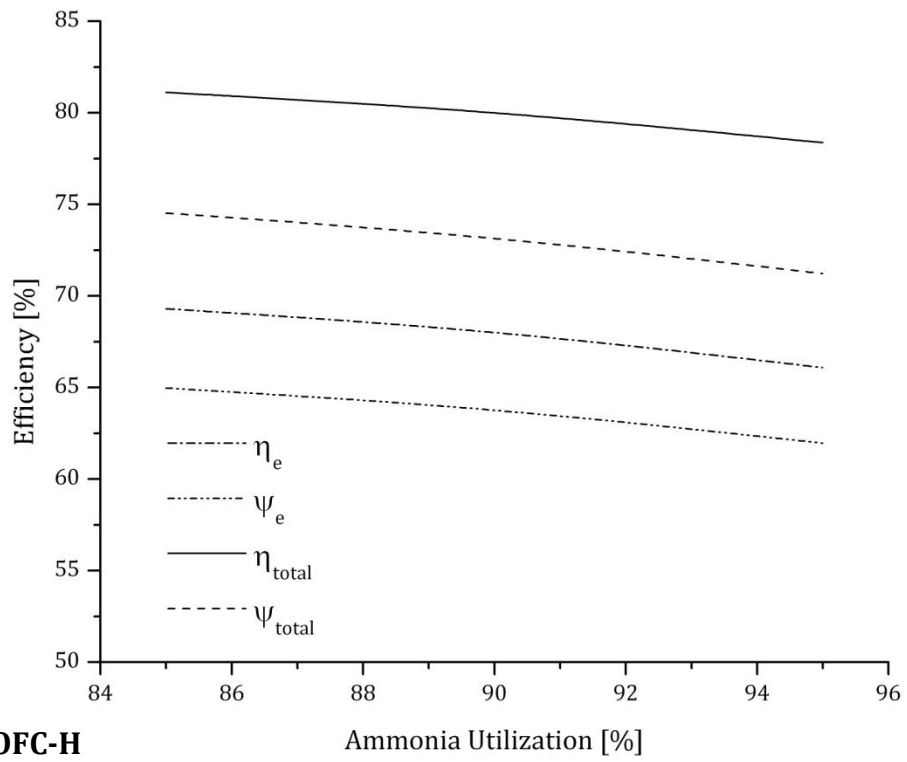


Figure 6.37: Effect of ammonia utilization on the total specific power and back work ratio.

As depicted in Figure 6.38, the energy and exergy efficiencies of the system with SOFC-H option remain higher than those of the system with SOFC-O across all fuel utilization values. In addition, increasing the utilization of ammonia negatively impacts the efficiencies of both systems by operating at reduced voltage, specific power and molar flow rates of ammonia and air.



(a) SOFC-O



(b) SOFC-H

Figure 6.38: Effect of ammonia utilization on the efficiency of the system.

- **Effect of Fuel Cell Temperature**

Increasing the operating temperature of the fuel cell incorporated in this system results in appreciable decline in specific power as revealed by Figure 6.39. At such elevated temperatures, the operating voltage is reduced to a level that permits the heat generated from the thermodynamic irreversibilities of the respective fuel cell to satisfy the heating requirements of the incoming reactants. Conversely, the higher temperature of the gaseous products increases the power production of the turbine hence the lower back work ratio.

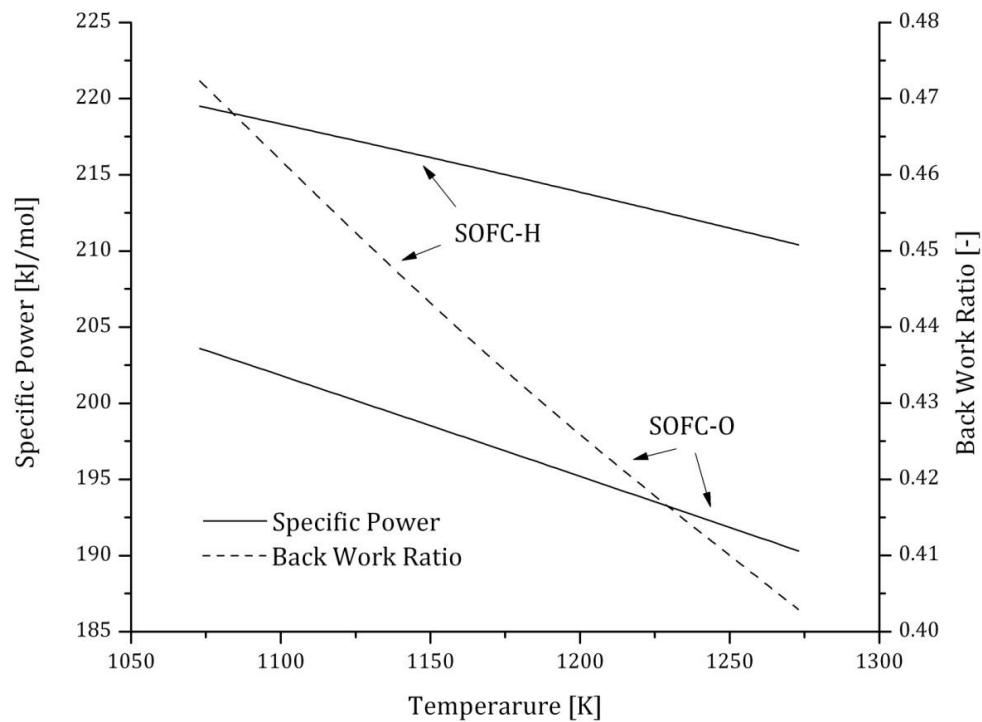
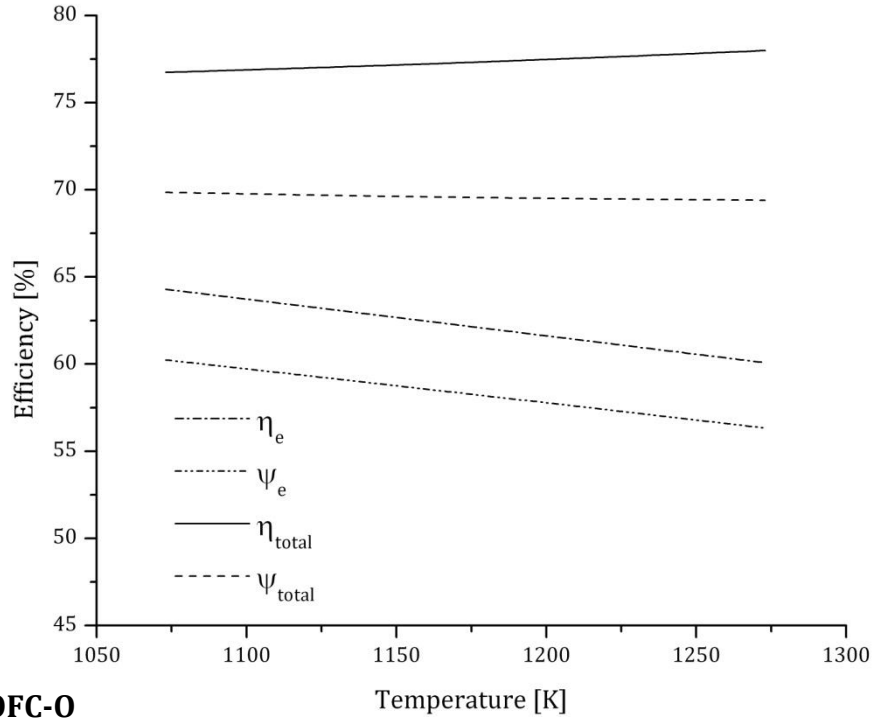
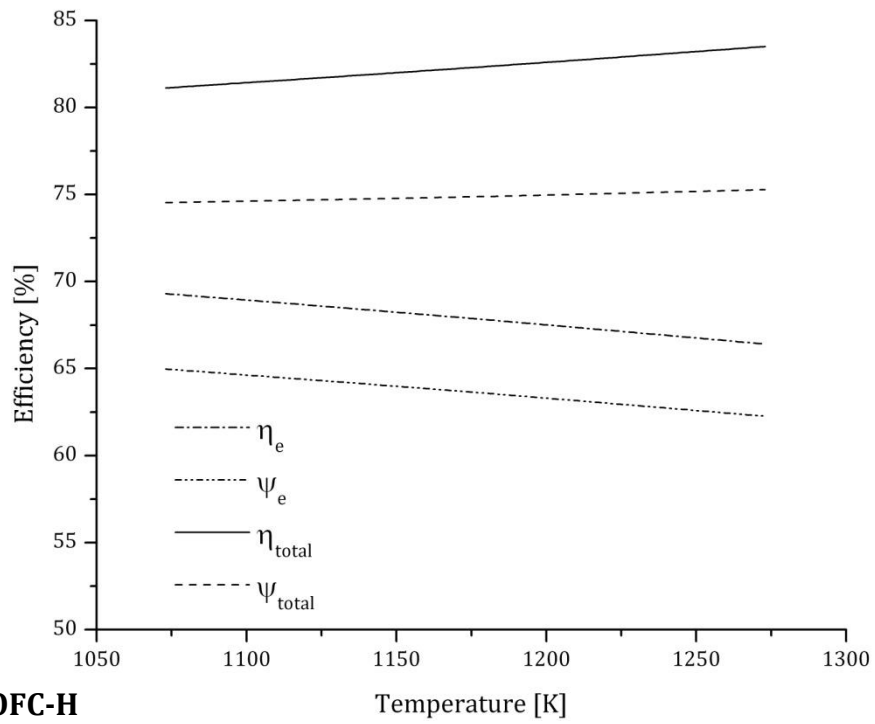


Figure 6.39: Effect of the fuel cell temperature on the total specific power and back work ratio.

The effect of the fuel cell temperature on the efficiency of the systems is shown in Figure 6.40. It is evident that the system integrated with SOFC-H option continues



(a) SOFC-O



(b) SOFC-H

Figure 6.40: Effect of fuel cell temperature on the efficiency of the system.

to show superior performance and efficiency in comparison to those integrated with SOFC-O. It can be observed that the electrical energy and exergy efficiency degrade as the temperature of the fuel cell decreases in consequence of lower specific power. In spite of that, the higher temperature of the gaseous products boosts the amount of recoverable heat and associated exergy leading to an overall increase in the total energy and exergy efficiency of the respective integrated system.

- **Effect of Pressure Ratio**

Figure 6.41 reveals that it is advantageous to operate the studied systems at low pressure ratio. The inspection of the data in Table 6.5 shows that the respective fuel

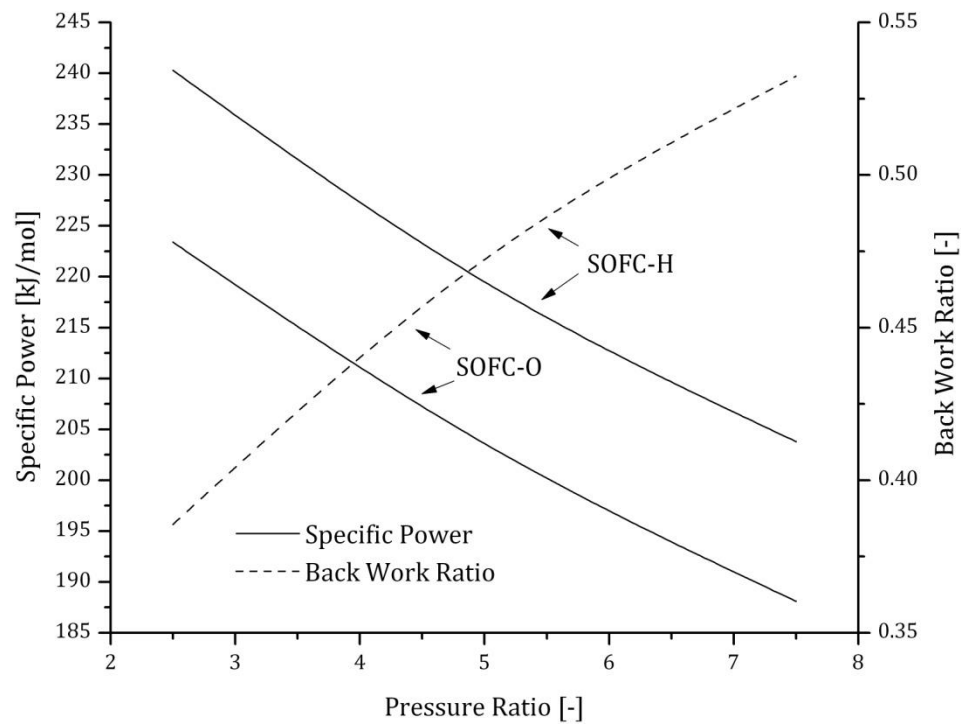


Figure 6.41: Effect of pressure ratio on the total specific power and back work ratio.

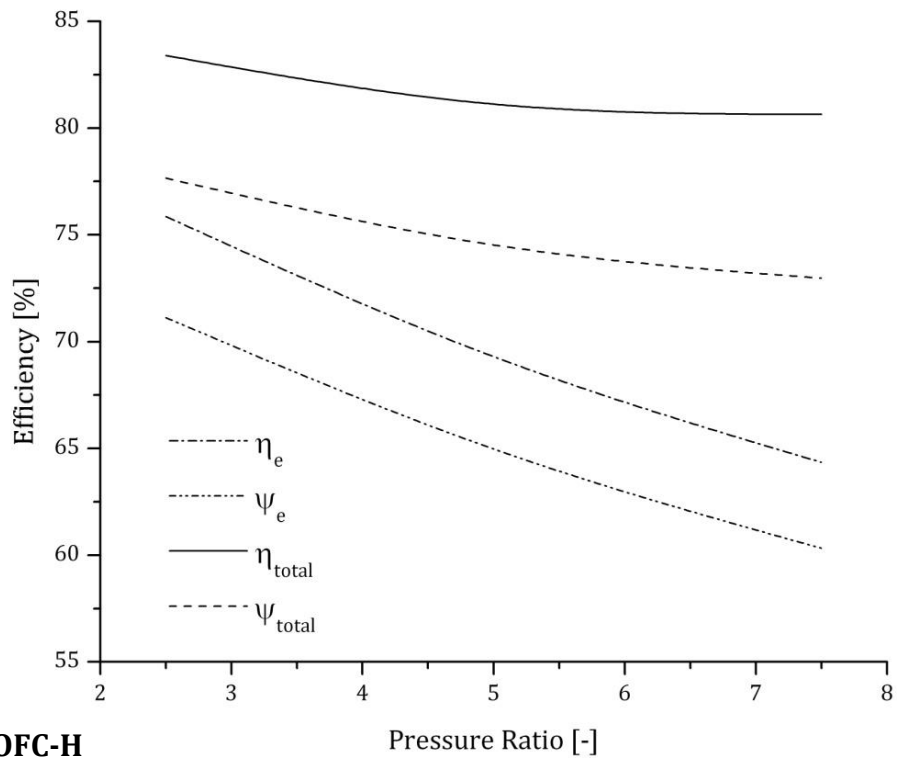
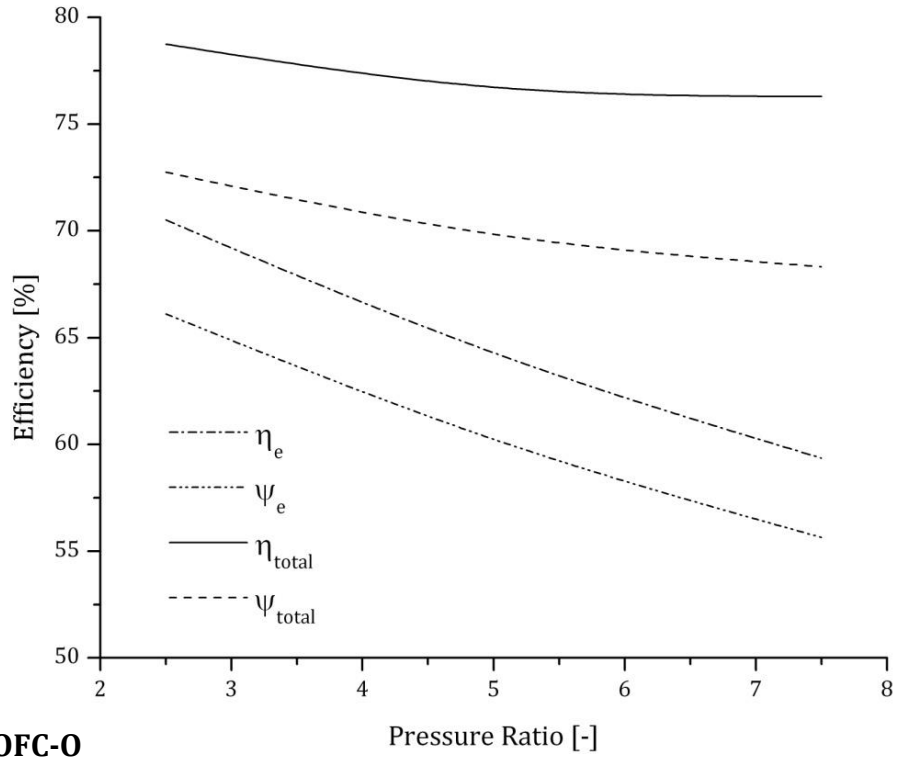


Figure 6.42: Effect of pressure ratio on the efficiency of the system.

cell operates at reduced voltage to meet the constraints of heating the reactants as discussed earlier. In addition, more power is drawn by the air compressor as the difference between the atmospheric pressure and the pressure of the fuel cell increases. As a result, the specific power decreases while the back work ratio increases. This also leads to a sharp decrease of the electrical energy and exergy efficiency within the studied range as shown in Figure 6.42. However, the ratio of recoverable heat at the recuperator to the heat input to the ammonia tank increases proportionally with the increase of the pressure ratio. In this manner, the decline in the overall energy and exergy efficiency is less pronounced at higher pressure ratios. It is also worth noting that refrigeration or cooling effect of ammonia in the tank is influenced by the pressure ratio as demonstrated in Table 6.8. It can be observed that the increase of the saturation temperature of ammonia at the corresponding pressure is diminishing the cooling effect and the effectiveness of the process. This offers another reason to operate the integrated DA-SOFC/GT system at lower pressures.

Table 6.8: Effect of pressure ratio on the cooling performance of ammonia in DA-SOFC/GT system.

Pressure Ratio	2.5	5.0	7.5
Temperature at T1 [K]	259.5	277.3	289
Cooling Load [kJ/mol]	47.3	46.7	46.3
Effectiveness [%]	14.9	14.7	14.6

6.5.2 Urea-fed SOFC/GT system

Although efforts were made to maintain the similarity between the DA-SOFC/GT and DU-SOFC/GT systems, apparent differences exist like the use of heat exchanger-mixer (HXM) unit to provide heat while mixing the solid urea with water. Most importantly, heat exchanger (HX2) was removed from the DU-SOFC/GT system as it was found, during the course of simulation, that second law of thermodynamics was violated by means of negative exergy destruction which rendered the component to be physically impractical. This can be explained by fact that the heat capacity rate of the heat donor was less than that of the heat receiver.

Furthermore, the integrated system with SOFC-H option could not operate at fuel utilization factors higher than 75%. The deficient performance is due to the detrimental effect of the reverse water gas shift reaction which essentially diminished the concentration of hydrogen at the anode of the fuel cell. Table 6.9 reflects the parameters used for the analysis of the systems with SOFC-O and SOFC-H options.

Figure 6.43 depicts the polarization curve of the ion-conducting DU-SOFC with a peak power density of 1100 W/m^2 at 0.67 V . The polarization curve of the proton-conducting DU-SOFC is shown in Figure 6.44 with a peak power density of 1973 W/m^2 at 0.68 V . However, the graphs cannot be directly compared due to the difference in the fuel utilizations as reflected in the same figures.

Table 6.9: Main parameters used for the base case study of DU-SOFC/GT system.

Fuel utilization factor (SOFC-O), U_f [%]	85
Oxidant utilization factor (SOFC-O), U_o [%]	25
Fuel utilization factor (SOFC-H), U_f [%]	75
Oxidant utilization factor (SOFC-H), U_o [%]	20
Stack temperature, T_{FC} [K]	1073
Pressure ratio, PR	5
Pinch temperature difference, D_p [K]	20
Cumulative cell area, A_{FC} [m ²]	250
Compressor efficiency, $\eta_{s,c}$ [%]	85
Turbine efficiency, $\eta_{s,t}$ [%]	90
Heat exchanger effectiveness, ξ [%]	90
AC generator efficiency, η_G [%]	95
DC/AC inverter, η_{INV} [%]	98
Ambient temperature, T_{amb} [K]	298
Ambient pressure, P_{amb} [kPa]	101.3
Molar composition of oxygen in air, [%]	21
Molar composition of nitrogen in air, [%]	79

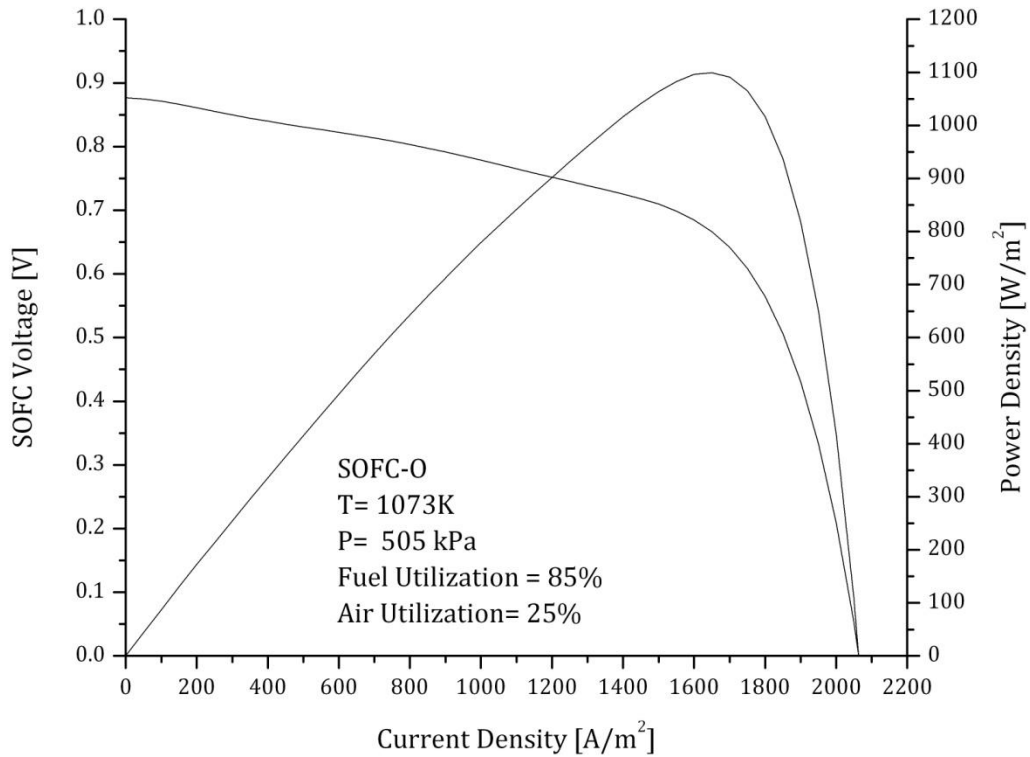


Figure 6.43: Polarization curve of ion-conducting DU-SOFC (base case).

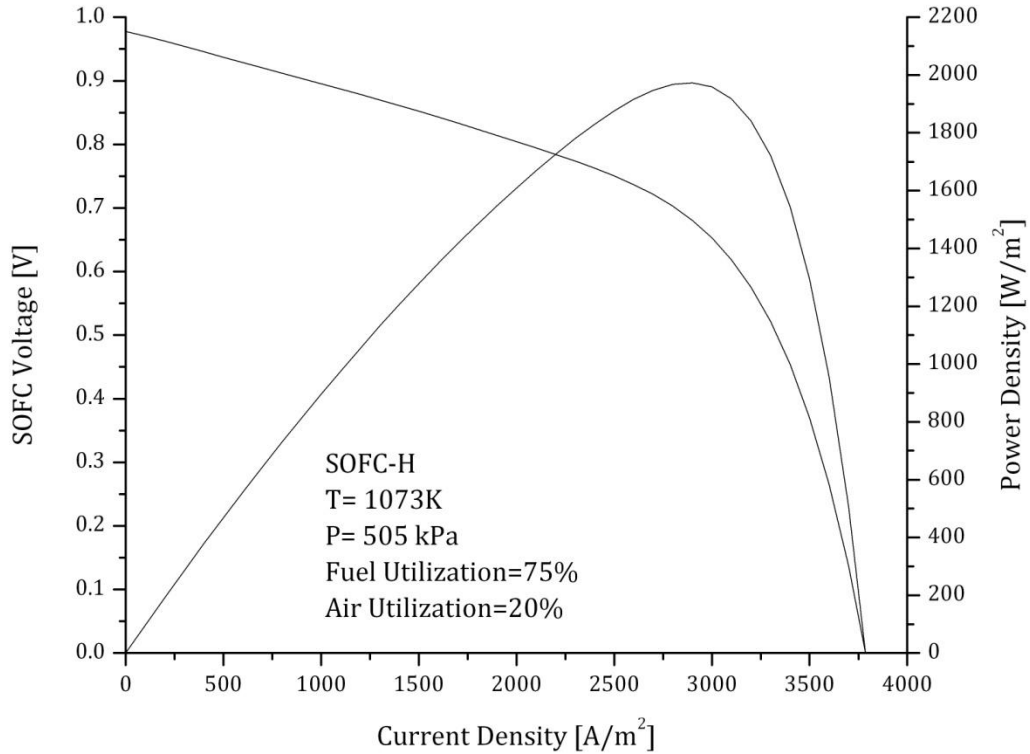


Figure 6.44: Polarization curve of proton-conducting DU-SOFC (base case).

Similar to the integrated systems fuelled with ammonia, those fuelled with urea cannot operate at any voltage equal or higher than that corresponding to the peak power density. Instead, the system efficiency is sacrificed by operating at much lower voltage to provide the reactants with sufficient heat to reach the required operating temperature. The operating voltages and current densities are listed in Table 6.10 which clearly reveals the restricted performance of the proton-conducting SOFC/GT system for the same reasons discussed earlier.

The temperature distribution of the ion-conducting SOFC/GT system is illustrated in Figure 6.45 while the state points correspond to those shown in Figure 4.6. It can be seen that the temperature of the anode inlet is about 250K lower than that of the

cathode inlet. This is owing to fact that 82.5% of thermal energy transferred at the heat exchanger-mixer (HXM) is utilized for the heating and vaporization of the aqueous urea while the remainder is used for the sensible heating of the anode feed gas stream.

Table 6.10: Operating voltage and current density of DU-SOFC/GT system at different conditions.

Fuel Cell	SOFC-O		SOFC-H	
	V [V]	J [A/m ²]	V [V]	J [A/m ²]
Base Case	0.38	1930	0.28	3585
T _{FC} = 1173K	0.29	2050		
T _{FC} = 1273K	0.21	2110		
U _f = 0.90	0.32	1650		
U _f = 0.95	0.25	795		
PR= 2.5	0.56	1925	0.57	3165
PR= 7.5	0.31	2060		

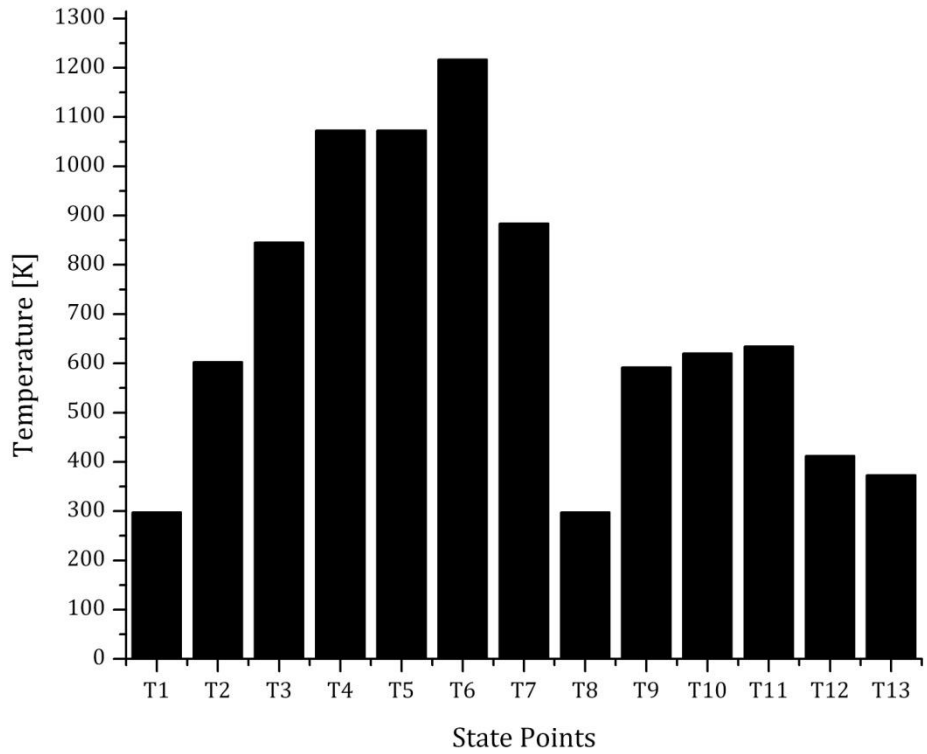


Figure 6.45: Temperature distribution of ion-conducting DU-SOFC/GT system (base case).

From the same figure, it can be deduced that high exergy destruction occurs at the mixer (M) due to mixing of gas streams (7a and 10) of different temperatures. This is also reflected in Figure 6.46 which shows that 0.19% of the total exergy destruction in the system occurs at the mixer. The fuel cell is the largest single contributor to the exergy destruction in the system due high overpotential losses. This is followed by the heat exchanger-mixer (HXM) which account for 13.1% of the total exergy destruction due to the difference in heat capacity rate between the heat donor and the receiver.

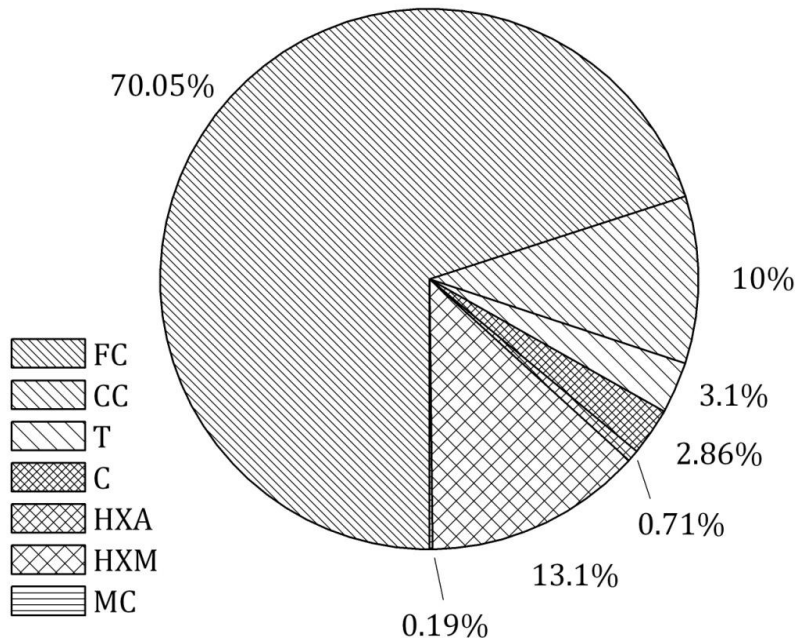


Figure 6.46: Exergy destruction of ion-conducting DU-SOFC/GT system by component (base case).

Figure 6.47 reflects the temperature distribution of proton-conducting DU-SOFC/GT system. The state points correspond to those shown in Figure 4.6. A number of observations can be made from the figure. There is a difference of 470K between

the anode (T2) and the cathode (T3) inlet temperatures. Such substantial difference can be a precursor for thermally-induced stresses in the fuel cell assembly leading to problems concerning gas sealing and cracking of ceramic components. The operation of the fuel cell with 75% fuel utilization means that high amount of unconsumed hydrogen is burned in the combustion chamber where the temperature rise is as high as 1509K. Similar to the ion-conducting DU-SOFC/GT system, considerable exergy destruction takes place in the mixer due to the large difference between the temperatures of the mixing gas steams (T7 and T10).

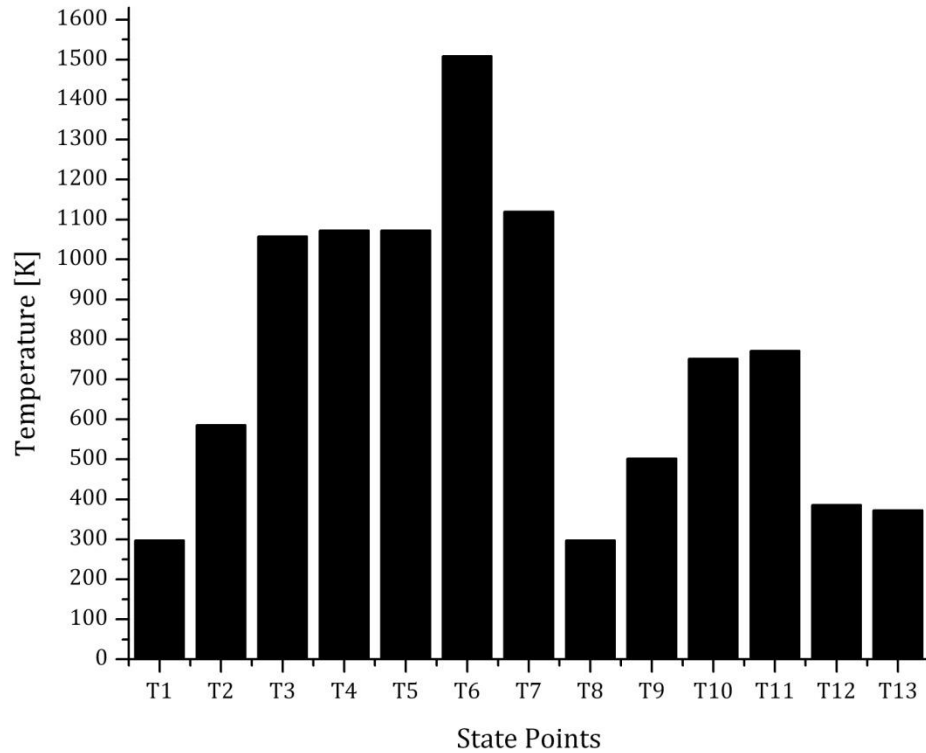


Figure 6.47: Temperature distribution of proton-conducting DU-SOFC/GT system (base case).

Despite that, it only accounts for 0.11% of the total exergy destruction of the system as depicted in Figure 6.48. The exergy destruction in the fuel cell is excessively high due to operating at low voltage (high overpotential losses).

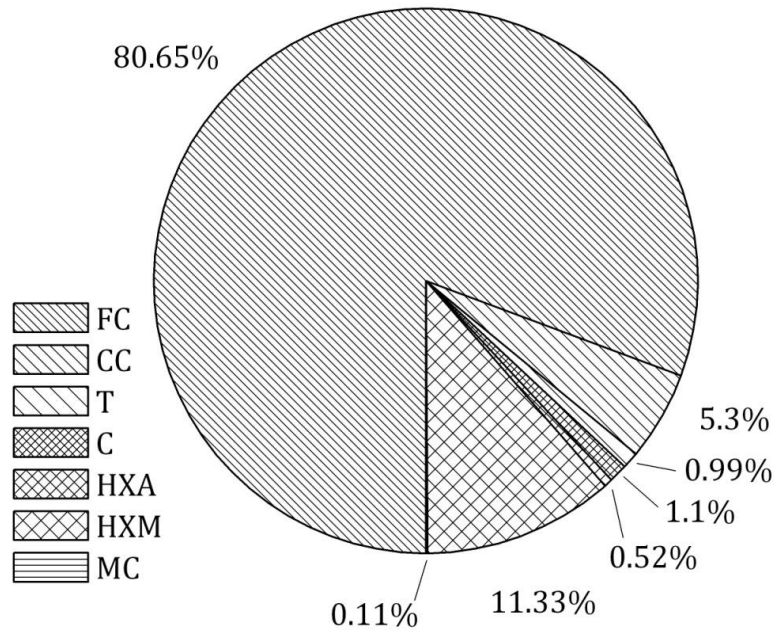


Figure 6.48: Exergy destruction of proton-conducting DU-SOFC/GT system by component (base case).

Table 6.11 lists the specific power produced and the exergy destruction per mole of aqueous urea. Although direct comparison between the two types of system cannot be made, it can be observed that the system with SOFC-O enjoys much higher performance than that with SOFC-H option. However, both DU-SOFC/GT systems display lower performance and higher losses when compared to the DA-SOFC/GT systems as reflect in Table 6.12.

Table 6.11: Specific power and exergy destruction in kJ/mol of fuel for DU-SOFC/GT system (base case).

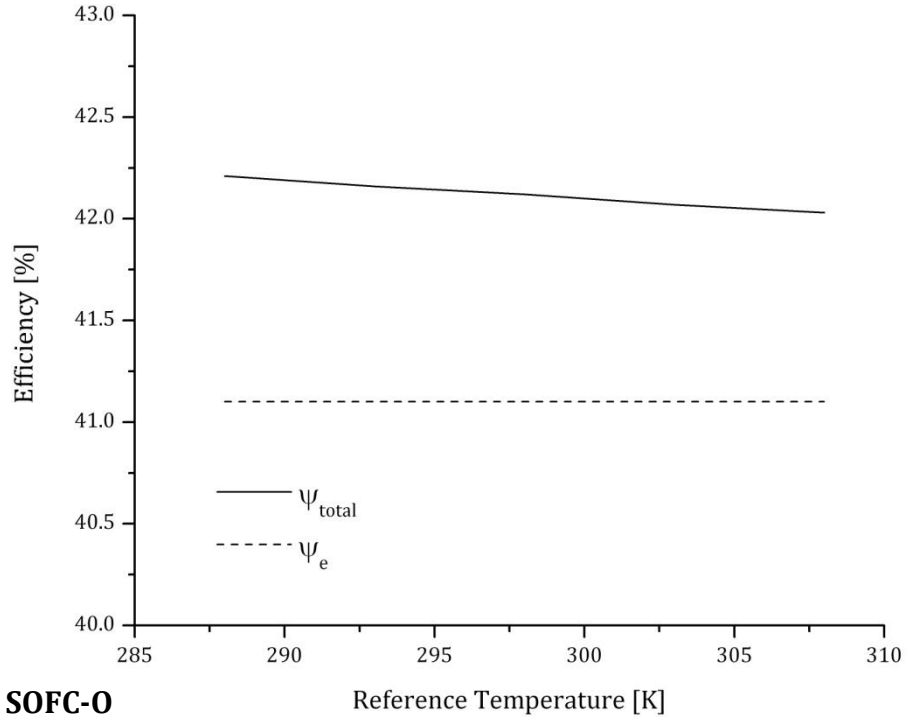
Type of Fuel Cell		SOFC-O	SOFC-H
Overall System	Total specific power [kJ/mol]	141.6	86.0
	Total exergy destruction [kJ/mol]	190.8	252.0
Components	Specific power of fuel cell [kJ/mol]	68.8	26.1
	Specific power of electric generator [kJ/mol]	72.8	59.9

Table 6.12: Energy and exergy efficiency of DA-SOFC/GT system (base case).

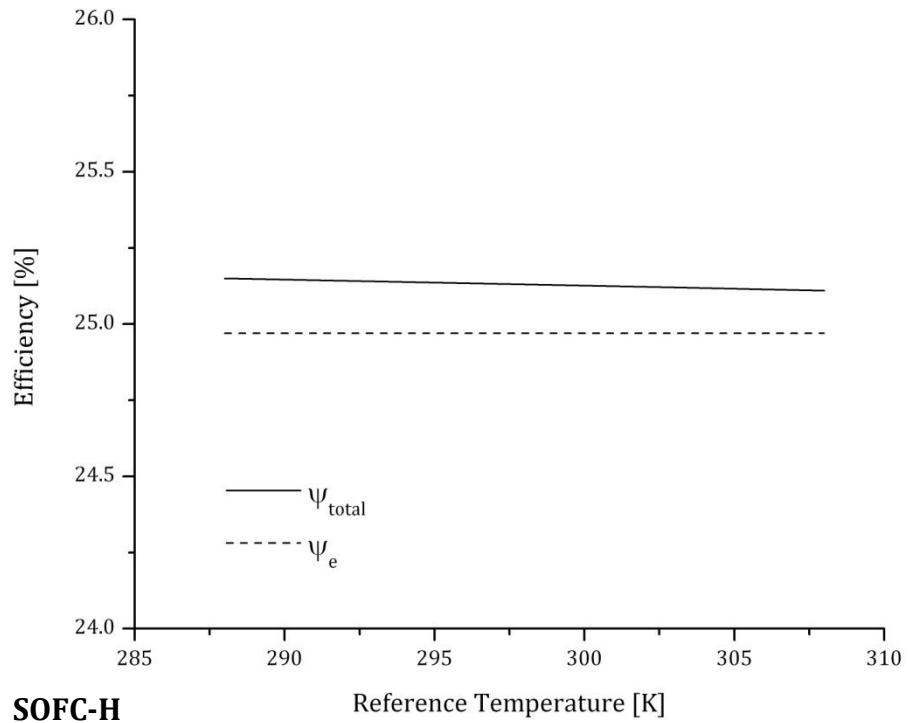
Type of Fuel Cell		SOFC-O	SOFC-H
Overall System	η_{total}	56.8	32.5
	ψ_{total}	42.1	25.1
	η_e	52.1	31.7
	ψ_e	41.1	25.0
Components	ψ_{FC}	34.4	11.6
	ψ_{CC}	92.7	93.5
	ψ_T	95.7	97.3
	ψ_C	90.2	90.2
	ψ_{HXA}	97.6	97.5
	ψ_{HXM}	93.6	92.7

- **Effect of Reference State**

The effect of changing the reference temperature on the exergy efficiency is shown in Figure 6.49. For the case of SOFC-O, the temperature of exhaust gases at the inlet of the recuperator is about 413K while the outlet temperature is controlled at 373K. Similarly, the temperature of exhaust gases at the inlet of the recuperator is about 387K while the outlet temperature is controlled at 373K for the case of SOFC-H. Therefore, small quantity of heat is recovered from the respective system which contributes to the narrow difference between the total and electrical exergy efficiencies.



(a) SOFC-O



(b) SOFC-H

Figure 6.49: Effect of reference temperature on the exergy efficiency of DU-SOFC/GT system (base case).

- **Effect of Urea Utilization**

Figure 6.50 shows the effect of the urea utilization on the total specific power and back work ratio. Although the system exhibits low performance, it can be seen that the overall behaviour of this system is rather similar to that of the ion-conducting DA-SOFC/GT. Operating at higher urea utilization demands more oxidant to satisfy the electrochemical reaction which in turn increases the thermal requirements of heating the reactants. Therefore, the system seeks the operation at a lower working voltage. The combination of the aforementioned reasons leads to the behaviour shown in the figure.

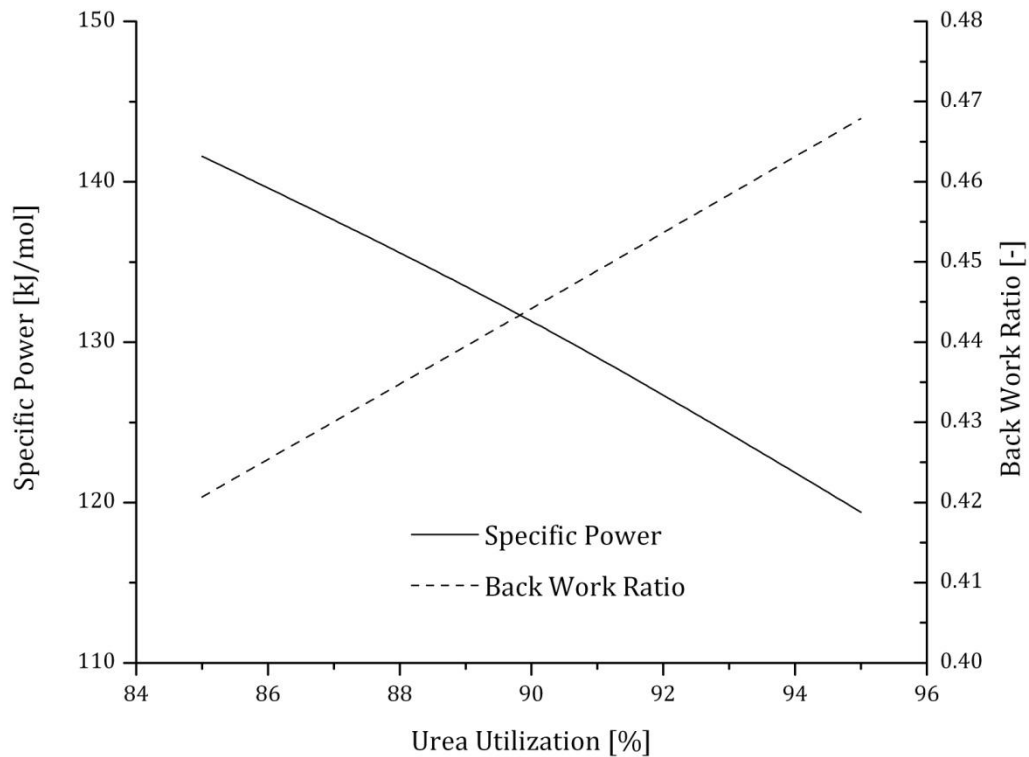


Figure 6.50: Effect of urea utilization on the specific power and back work ratio of ion-conducting DU-SOFC/GT system.

The efficiency of the system also decreases when the urea utilization is increased as depicted in Figure 6.51. This can be related to the lower total specific power and higher back work ratio as described earlier.

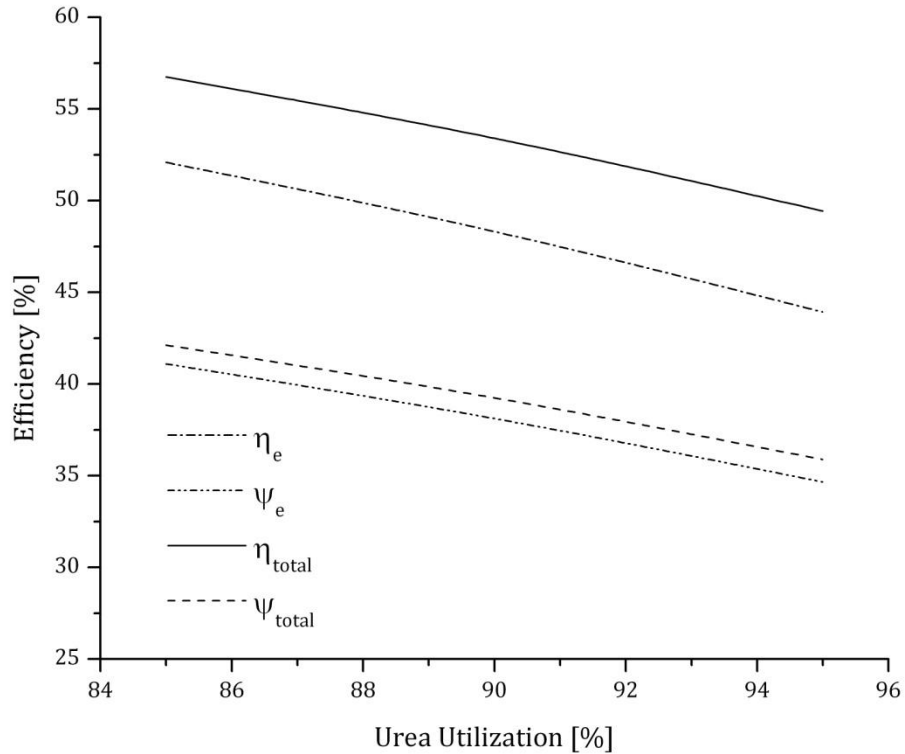


Figure 6.51: Effect of urea utilization on the efficiency of ion-conducting DU-SOFC/GT system.

▪ Effect of Fuel Cell Temperature

The total specific power of the ion-conducting DU-SOFC/GT system decreases when the operating temperature of the fuel cell increases as illustrated in Figure 6.52. The behaviour of the system is justified by recalling that additional heat is required to raise the operating temperature which forces the fuel cell to run at a lower voltage. The back work ratio is reduced given the higher power produced by the gas turbine

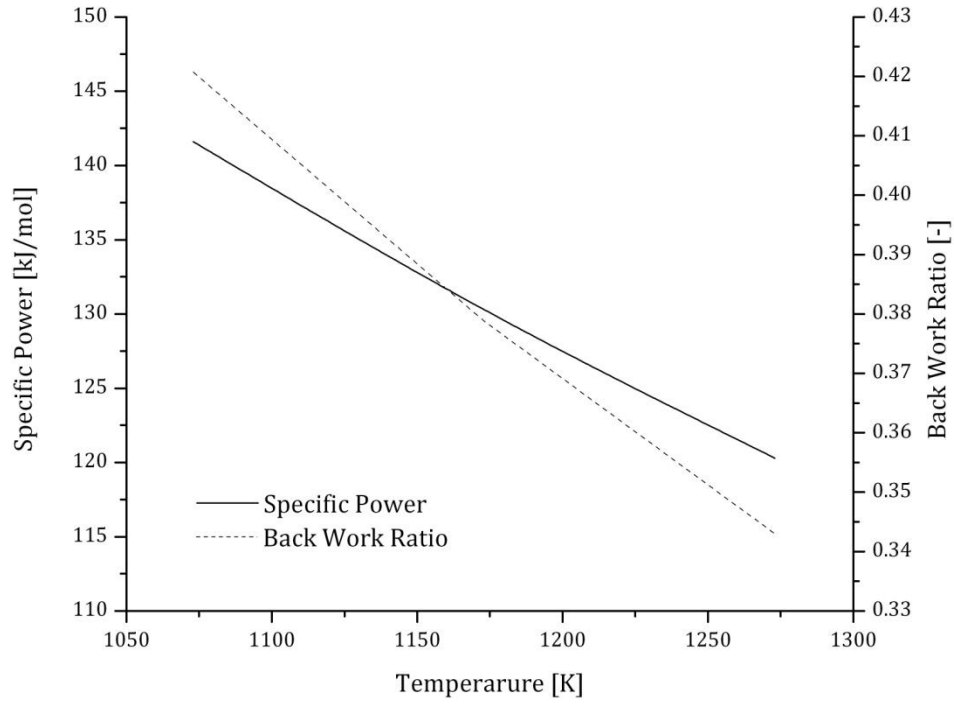


Figure 6.52: Effect of the fuel cell temperature on the total specific power and back work ratio of ion-conducting DU-SOFC/GT system.

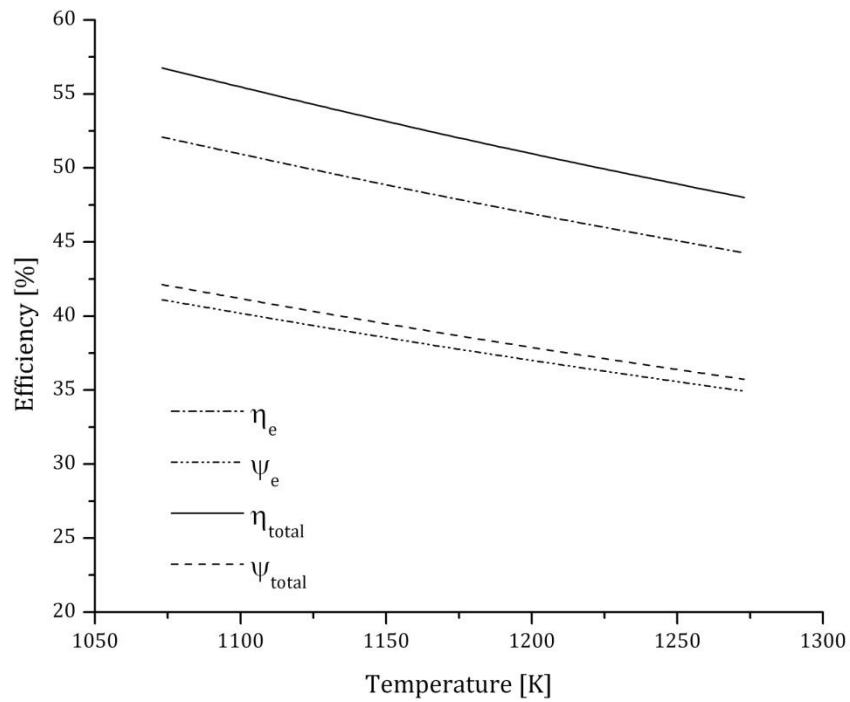


Figure 6.53: Effect of the fuel cell temperature on the efficiency of ion-conducting DU-SOFC/GT system.

despite the higher stoichiometric air requirements when the operating temperature is increased. However, this gain is not sufficient to overcome the significant loss of efficiency in the fuel cell as shown in Figure 6.53. Unlike the performance of ion-conducting DA-SOFC/GT system, the overall energy and exergy efficiencies of the current system cannot compensate for the loss of electrical energy and exergy efficiencies at higher operating temperatures. This can be explained by noting that the heat recovery temperature at the recuperator remained in the range of 409-413K across all operating temperatures.

- **Effect of Pressure Ratio**

As Figure 6.54 suggests, the response of the system to the increase in pressure ratio is similar to that of the DA-SOFC/GT system. At lower pressure ratio, the outlet temperature of the gas turbine is sufficiently high to increase the temperature of the incoming air through the heat exchanger (HXA) such that the constraint of sensible heating inside the fuel cell stack is considerably reduced. In turn, this allows the fuel cell to operate at a higher voltage hence the higher specific power. Moreover, the process of air compression requires additional power input as the pressure ratio increases which results in higher back work ratio. Figure 6.55 affirms that the efficiency of the system is higher at lower pressure ratio due to higher specific power. Therefore, it is advantageous to operate the ion-conducting SOFC/GT system at the lowest pressure ratio within the studied range.

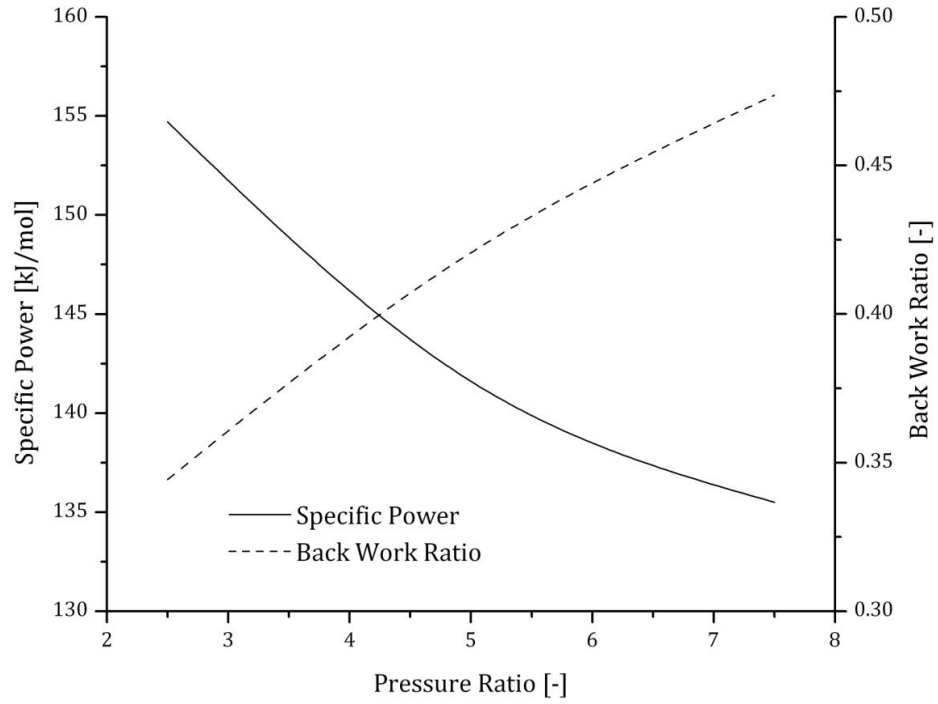


Figure 6.54: Effect of pressure ratio on the total specific power and back work ratio of ion-conducting DU-SOFC/GT system.

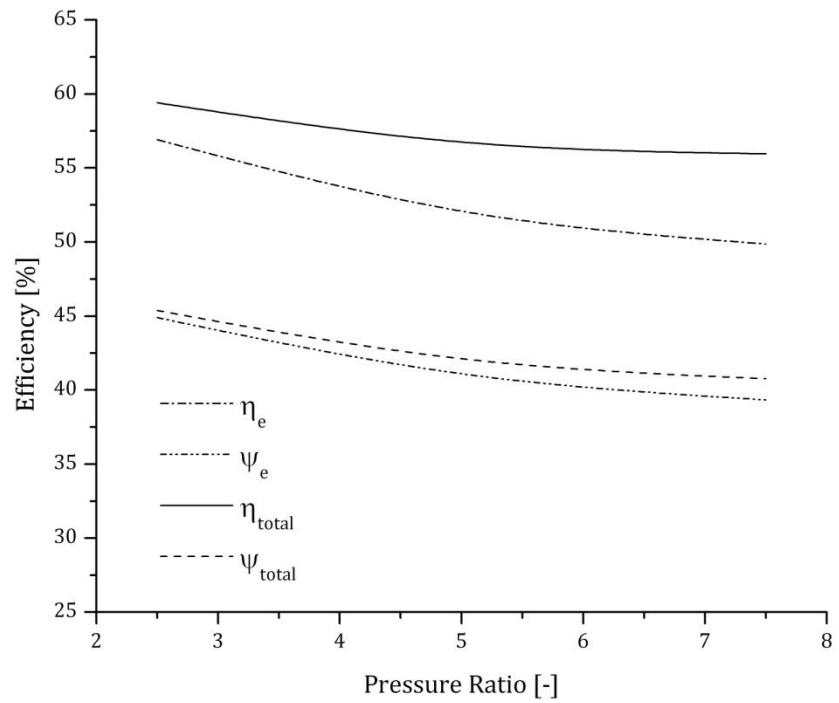


Figure 6.55: Effect of pressure ratio on the efficiency of ion-conducting DU-SOFC/GT system.

The same rationale can be applied to explain the response of proton-conducting SOFC/GT system to the change in pressure ratio which is shown in Figures 6.56 and 6.57. However, the investigated range was limited to a pressure ratio of five as discussed at the beginning of this section.

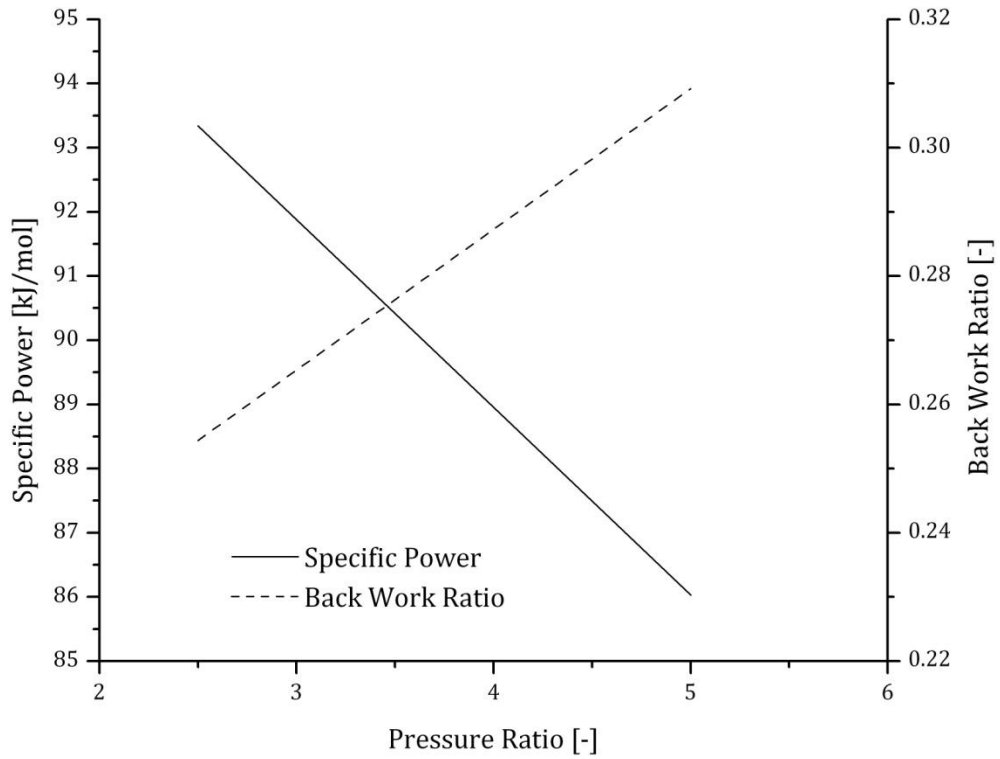


Figure 6.56: Effect of pressure ratio on the total specific power and back work ratio of proton-conducting DU-SOFC/GT system.

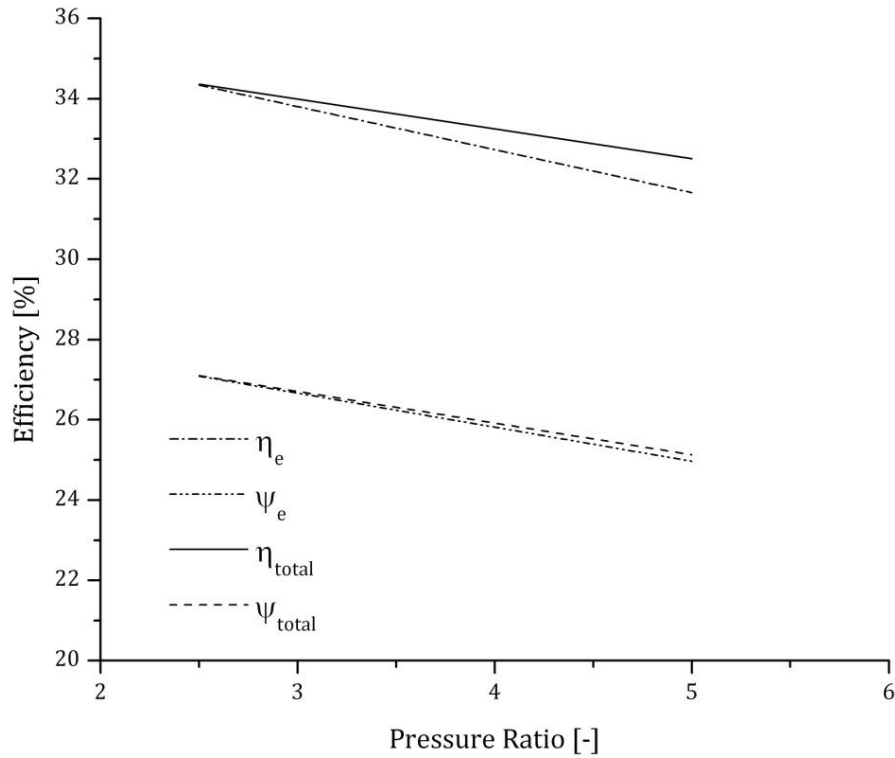


Figure 6.57: of pressure ratio on the efficiency of proton-conducting DU-SOFC/GT system.

- **Additional Remarks**

The water vapour of the exhaust gas of the DU-SOFC/GT system can be recovered by passing the gas through a condensing unit. Using the base case study of ion-conducting DU-SOFC/GT as an example, 3.87 moles of water vapour in the exhaust gas can be condensed and partially utilized to hydrolyze 1.29 moles of urea which only requires an equimolar amount of water to complete the hydrolysis. The remaining amount of water can be further used for low-grade heating if needed.

It is also interesting to mention that some amount of urea can be added to the water in the storage tank to lower its freezing temperature. For example, the freezing

temperature of a solution of water containing 32% urea (by weight) is 262K [93]. This can be very convenient in cold temperature applications.

From the forgoing discussions, it can be clearly concluded that the performance of the DA-SOFC/GT is higher than that of the DU-SOFC/GT across all parametric conditions. However, both systems can be possibly improved by using multi-stage heating of reactants. In the particular case of DU-SOFC/GT, water vapour in the exhaust gas can be condensed and recovered for the hydrolysis of urea which can significantly reduce the amount of make-up water and the associated requirements for sensible heating.

Chapter Seven : Conclusions and Recommendations

This study examined the thermodynamic performance of ion and proton-conducting solid oxide fuel cells fuelled with ammonia as well urea.

7.1 Conclusions

The following conclusions can be drawn from this work:

1. The proton-conducting ammonia fed SOFC maintained the highest reversible cell potential under all open-circuit conditions followed by the ion-conducting counterpart. The ion and proton-conducting urea fed fuel cells attained lower cell potentials due to higher overpotentials
2. Under closed-circuit conditions, the proton-conducting ammonia fed SOFC demonstrated the best performance due to higher partial pressure of hydrogen at the anode in comparison to the ion-conducting counterpart. In addition, intermediate and side reactions at the anode of ion and proton-conducting urea fed SOFC resulted in a drastic reduction of the hydrogen partial pressure hence the lower performance.
3. The reverse water gas shift reaction has a detrimental effect on the partial pressure of hydrogen at the anode of urea fed SOFC. In particular, the effect is most pronounced in the proton-conducting SOFC mainly due to the absence of sufficient water vapour at the anode of the cell.
4. The overall thermal and exergy efficiencies of the ion and proton-conducting DA-SOFC/GT were in the range of 70-85% depending on the operating conditions indicating suitable arrangement of components of the systems.

5. The poor performance and efficiencies demonstrated by the ion and proton-conducting DU-SOFC/GT systems are mainly due to low hydrogen partial pressure at the anode of the fuel cell and the substantial heat requirements of the thermohydrolysis process.
6. High rates of exergy destruction were manifested in components where chemical or electrochemical reactions occurred (i.e. fuel cell, combustion chamber and mixers)

7.2 Recommendations

Despite the successful experimental demonstration of ion and proton-conducting ammonia fed solid oxide fuel cells under steady state conditions, it is still necessary to perform dimensional analysis and transient studies to further characterize the decomposition of ammonia inside the fuel cell anode under such conditions. In addition, experiments must be first conducted in order to determine the reaction series and kinetics of the thermohydrolysis of urea and its applicability to power production using solid oxide fuel cells. Further theoretical studies can include dimensional analysis under steady-state and transient conditions as well. The process of active CO₂ removal from the products of the thermohydrolysis of urea may also be worth exploring. Finally, a comprehensive cost analysis is required to establish the actual cost of electricity produced using such systems.

References

- [1] A. Klerke, C.H. Christensen, J.K. Norskov, and T. Vegge, "Ammonia for hydrogen storage: challenges and opportunities," *Journal of Materials Chemistry*, vol. 18, pp. 2304-2310, 2008.
- [2] B. Sakintuna, F. Lamari-Darkrim, and M. Hirscher, "Metal hydride materials for solid hydrogen storage: A review," *International Journal of Hydrogen Energy*, vol. 32, pp. 1121-1140, 2007.
- [3] T.B. Marder, "Will We Soon Be Fueling our Automobiles with Ammonia-Borane," *Angewandte Chemie International Edition*, vol. 46, no. 43, pp. 8116-8118, 2007.
- [4] Chemical Industry News & Intelligence, "Ammonia Uses and Market Data," [Online].
<http://www.icis.com/v2/chemicals/9075154/ammonia/uses.html>
(Accessed: November 2010).
- [5] G. Thomas and G. Parks, "Potential Roles of Ammonia in a Hydrogen Economy," U.S. Department of Energy, 2006.
- [6] European Fertilizer Manufacturers' Association, "Production Of Ammonia," European Fertilizer Manufacturers' Association, BAT Booklet 2000.
- [7] NIST, "Thermophysical Properties of Hydrogen," [Online].
<http://webbook.nist.gov/cgi/fluid.cgi?ID=C1333740&Action=Page>
(Accessed: March 2011).
- [8] Q. Ma, J. Ma, S. Zhou, R. Yan, J. Gao, and G. Meng, "A high-performance ammonia-fueled SOFC based on a YSZ thin-film electrolyte," *Journal of Power Sources*, vol. 164, pp. 86-89, 2007.
- [9] E.P. Egan and B.B. Luff, "Heat of Solution, Heat Capacity and Density of Aqueous Urea Solutions at 25C," *Journal of Chemical and Engineering Data*, vol. 11, no. 2, pp. 192-194, April 1966.
- [10] Canadian Centre for Occupational Health and Safety, "Health Effects of Ammonia Gas," [Online].
http://www.ccohs.ca/oshanswers/chemicals/chem_profiles/ammonia/health_ammonia.html (Accessed: March 2011).
- [11] C.H. Christensen, R.Z. Sorensen, T. Johannessen, and U.J. Quaade, "Metal ammine complexes for hydrogen storage," *Journal of Materials Chemistry*, vol. 15, pp. 4106-4108, 2005.

- [12] D.F. Putnam, "Composition and Concentrative Properties of Human Urine," NASA, Washington, Technical Report NASA CR-1802, 1971.
- [13] Chemical Industry News & Intelligence, "Urea Uses and Market Data," [Online]. <http://www.icis.com/v2/chemicals/9076559/urea/uses.html> (Accessed: December 2010).
- [14] C. Sigala and C. G. Vayenas, "Ammonia oxidation to nitric oxide in a solid electrolyte fuel cell," *Solid State Ionics*, vol. 5, pp. 567-570, 1981.
- [15] R. D. Farr and C. G. Vayenas, "Ammonia High Temperature Solid Electrolyte Fuel Cell," *Journal of the Electrochemical Society*, vol. 127, no. 7, pp. 1478-1483, 1980.
- [16] A. Wojcik, H. Middleton, I. Damopoulos, and J. Van Herle, "Ammonia as a fuel in solid oxide fuel cells," *Journal of Power Sources*, vol. 118, no. 1-2, pp. 342-348, 2003.
- [17] Q. Ma, R. Peng, L. Tian, and G. Meng, "Direct utilization of ammonia in intermediate-temperature solid oxide fuel cells," *Electrochemistry Communications*, vol. 8, pp. 1791-1795, 2006.
- [18] G. Meng, C. Jiang, J. Ma, Q. Ma, and X. Liu, "Comparative study on the performance of a SDC-based SOFC fueled by ammonia and hydrogen," *Journal of Power Sources*, vol. 173, pp. 189-193, 2007.
- [19] A. Fuerte, R.X.Valenzuela, M.J. Escudero, and L. Daza, "Ammonia as efficient fuel for SOFC," *Journal of Power Sources*, vol. 192, pp. 170-174, 2009.
- [20] L. Zhang and Y. Weishen, "Direct ammonia solid oxide fuel cell based on thin proton-conducting electrolyte," *Journal of Power Sources*, vol. 179, pp. 92-95, 2008.
- [21] K. Xie, Q. Ma, B. Lin, Y. Jiang, J. Gao, X. Liu, and G. Meng, "An ammonia fuelled SOFC with a BaCe_{0.9}Nd_{0.1}O_{3-δ} thin electrolyte prepared with a suspension spray," *Journal of Power Sources*, vol. 170, pp. 38-41, 2007.
- [22] Y. Lin, R. Ran, Y. Guo, W. Zhou, R. Cai, J. Wang, and Z. Shao, "Proton-conducting fuel cells operating on hydrogen, ammonia and hydrazine at intermediate temperatures," *International Journal of Hydrogen Energy*, vol. 35, pp. 2637-2642, 2010.
- [23] M. Ni, D.Y.C. Leung, and M.K.H. Leung, "Thermodynamic analysis of ammonia fed solid oxide fuel cells: Comparison between proton-conducting electrolyte and oxygen ion-conducting electrolyte," *Journal of Power Sources*, vol. 183,

pp. 682-686, 2008.

- [24] V. Mas, R. Kipreos, N. Amadeo, and M. Laborde, "Thermodynamic analysis of ethanol/water system with the stoichiometric method," *International Journal of Hydrogen Energy*, vol. 31, pp. 21-28, 2006.
- [25] M. Dieuzeide and N. Amadeo, "Thermodynamic Analysis of Glycerol Steam Reforming," *Chemical Engineering Technology*, vol. 33, no. 1, pp. 89-96, 2010.
- [26] A. Demin and P. Tsiakaras, "Thermodynamic analysis of a hydrogen fed solid oxide fuel cell based on a proton conductor," *International journal of hydrogen energy*, vol. 26, no. 10, pp. 1103-1108, 2001.
- [27] M. Ni, D.Y.C. Leung, and M.K.H. Leung, "Mathematical modeling of ammonia-fed solid oxide fuel cells with different electrolyte," *International Journal of Hydrogen Energy*, vol. 33, pp. 5765-5772, 2008.
- [28] S. Assabumrungrat, W. Sangtongkitcharoen, and N. Laosiripojan, "Effects of electrolyte type and flow pattern on performance of methanol-fuelled solid oxide fuel cells," *Journal of power sources*, vol. 148, no. 1-2, pp. 18-23, 2005.
- [29] P.M. Biesheuvel and J.J.C. Geerlings, "Thermodynamic analysis of direct internal reforming of methane and butane in proton and oxygen conducting fuel cells," *Journal of power sources*, vol. 185, no. 2, pp. 1162-1167, 2008.
- [30] M. Ni, D.Y.C. Leung, and M.K.H. Leung, "Electrochemical modeling of ammonia-fed solid oxide fuel cells based on proton conducting electrolyte," *Journal of Power Sources*, vol. 183, no. 2, pp. 687-692, 2008.
- [31] M. Ni, D.Y.C. Leung, and M.K.H. Leung, "An improved electrochemical model for the NH₃ fed proton conducting solid oxide fuel cells at intermediate temperatures," *Journal of Power Sources*, vol. 185, pp. 233-240, 2008.
- [32] A.S. Chellappa, C. M. Fischer, and W.J. Thomson, "Ammonia decomposition kinetics over Ni-Pt/Al₂O₃ for PEM fuel cell applications," *Applied catalysis. A, General*, vol. 227, no. 1-2, pp. 231-240, 2002.
- [33] X. Zhang, S.H. Chan, G. Li, H.K. Ho, J. Li, and Z. Feng, "A review of integration strategies for solid oxide fuel cells," *Journal of Power Sources*, vol. 195, pp. 685-702, 2010.
- [34] C. Zamfirescu and I. Dincer, "Thermodynamic performance analysis and optimization of a SOFC-H system," *Thermochimica Acta*, vol. 486, pp. 32-40, 2009.
- [35] I. Dincer, M.A. Rosen, and C. Zamfirescu, "Exergetic Performance Analysis of

a Gas Turbine Cycle Integrated With Solid Oxide Fuel Cells," *Journal of Energy Resources Technology*, vol. 131, pp. 1-11, September 2009.

- [36] B.K. Boggs, R.L. King, and G.G. Botte, "Urea electrolysis: Direct hydrogen production from urine," *Chemical Communications*, vol. 32, pp. 4859-4861, 2009.
- [37] R.L. King and G.G. Botte, "Hydrogen production via urea electrolysis using a gel electrolyte," *Journal of Power Sources*, vol. 196, no. 5, pp. 2773-2778, 2011.
- [38] M. Koebel and E.O. Strutz, "Thermal and Hydrolytic Decomposition of Urea for Automotive Selective Catalytic Reduction Systems: Thermochemical and Practical Aspects," *Industrial and Engineering Chemistry Research*, vol. 42, pp. 2093-2100, 2003.
- [39] M. Koebel, M. Elsener, and M. Kleemann, "Urea-SCR: a promising technique to reduce NO_x emissions for automotive diesel engines," *Catalysis Today*, vol. 59, pp. 335-345, 2000.
- [40] P. Hauck, A. Jentys, and J.A. Lercher, "Surface chemistry and kinetics of the hydrolysis of isocyanic acid on anatase," *Applied Catalysis B: Environmental*, vol. 70, pp. 91-99, 2007.
- [41] A. Lundstrom, B. Andersson, and L. Olsson, "Urea thermolysis studied under flow reactor conditions using DSC and FT-IR," *Chemical Engineering Journal*, vol. 150, pp. 544-550, 2009.
- [42] A.M.G. Gentemann and J. Caton, "Decomposition and oxidation of a urea-water solution as used in selective non-catalytic removal (SNCR) processes," in *2nd Joint Meeting of The United States Sections of the Combustion Institute*, Oakland, CA., 2001.
- [43] S.D. Yim, S.J. Kim, J.H. Baik, and I. Nam, "Decomposition of Urea into NH₃ for the SCR Process," *Industrial and Engineering Chemistry Research*, vol. 43, pp. 4856-4863, 2004.
- [44] F. Birkhold, M. Ulrich, P. Wassermann, and O. Deutschmann, "Modeling and simulation of the injection of urea-water-solution for automotive SCR DeNO_x-systems," *Applied Catalysis B: Environmental*, vol. 70, pp. 119-127, 2007.
- [45] M.J.L. Gines, A.J. Marchi, and C.R. Apesteguia, "Kinetic study of the reverse water-gas shift reaction over CuO/ZnO/Al₂O₃ Catalysts," *Applied Catalysis A: General*, vol. 154, pp. 155-171, 1997.

- [46] S. C. Singhal and K. Kendall, *High Temperature Solid Oxide Fuel Cells*. Oxford, UK: Elsevier Advanced Technology, 2003.
- [47] Y. Matsuzaki and I. Yasuda, "Electrochemical oxidation of H₂ and CO in a H₂-H₂O-CO-CO₂ system at the interface of a Ni-YSZ cermet electrode and YSZ electrolyte," *Journal of Electrochemical Society*, vol. 147, no. 5, pp. 1630-1635, 2000.
- [48] R. Suwanwarangkul, E. Croiset, M.W. Fowler, P.L. Douglas, E. Entchev, and M.A. Douglas, "Modeling of anode-supported SOFCs operating with H₂ and CO feed mixtures," in *Electrochemical Society Proceedings Volume 2003-07*, 2003, pp. 1348-1357.
- [49] N. F. Bessette, W. J. Wepfer, and J. Winnick, "Mathematical model of a solid oxide fuel cell," *Journal of Electrochemical Society*, vol. 142, no. 11, pp. 3792-3800, 1995.
- [50] B.A. Haberman and J.B. Young, "Three-dimensional simulation of chemically reacting gas flows in the porous support structure of an integrated-planar solid oxide fuel cell," *International Journal of Heat and Mass Transfer*, vol. 47, no. 17-18, pp. 3617-3629, 2004.
- [51] M. Ni, D.Y.C. Leung, and M.K.H. Leung, "Electrochemical modeling and parametric study of methane fed solid oxide fuel cells," *Energy Conversion and Management*, vol. 50, pp. 268-278, 2009.
- [52] M. Karcz, "Performance of a tubular fuel cell with internal methane reforming," *Chemical and Process Engineering*, vol. 28, no. 2, pp. 307-321, 2007.
- [53] L. Andreassi, C. Toro, and S. Ubertini, "Modeling carbon monoxide direct oxidation in solid oxide fuel cells," *Journal of Fuel Cell Science and Technology*, vol. 6, no. 2, pp. 0213071-02130715, 2009.
- [54] X-F. Ye, S.R. Wang, J. Zhou, F.R. Zeng, H.W. Nie, and T.L. Wen, "Assessment of the performance of Ni-yttria-stabilized zirconia anodes in anode-supported Solid Oxide Fuel Cells operating on H₂-CO syngas fuels," *Journal of Power Sources*, vol. 195, pp. 7264-7267, 2010.
- [55] S. Assabumrungrat and N. Laosiripojana, "Catalytic steam reforming of methane, methanol, and ethanol over Ni/YSZ: The possible use of these fuels in internal reforming SOFC," *Journal of Power Sources*, vol. 163, pp. 943-951, 2007.
- [56] Institute Of Energy And Climate Research (IEK) - Jülich Forschungszentrum. "Basic terms and operating principle of a fuel cell electricity generation

- system," [Online]. http://www.fz-juelich.de/ief/ief-3/fuel_cells/principles (Accessed: December 2010).
- [57] J. Larminie and A. Dicks, *Fuel Cell Systems Explained*, 2nd ed. London, UK: John Wiley & Sons Ltd., 2003.
- [58] EG&G Technical Services, *Fuel Cell Handbook*, 7th ed. Morgantown, USA, 2004.
- [59] V. Hacker and K. Kordesch, "Ammonia Crackers," in *Handbook of Fuel Cells - Fundamentals, Technology and Applications*, W. Vielstich, A. Lamm, and H. Gasteiger, Eds. Chichester: John Wiley & Sons Ltd., 2003, ch. Volume 3, Part 2, pp. 121-127.
- [60] F. Barbir, *PEM Fuel Cells Theory and Practice*. Burlington, USA: Elsevier Academic Press, 2005.
- [61] M. Mench, *Fuel Cell Engines*. New York, USA: John Wiley & Sons Inc., 2008.
- [62] V. Hacker, P. Enzinger, and M. Muhr, "Advantages Of Alkaline Fuel Cell Systems For Mobile Applications," [Online]. http://www.electricauto.com/_pdfs/Portland%20Paper%20A.pdf (Accessed: October 2010).
- [63] A. Arpornwichanop, Y. Patcharavorachot, and S. Assabumrungrat, "Analysis of a proton-conducting SOFC with direct internal reforming," *Chemical Engineering Science*, vol. 65, no. 1, pp. 581-589, 2010.
- [64] K. Faungnawakij, R. Kikuchi, and K. Eguchi, "Thermodynamic analysis of carbon formation boundary and reforming performance for steam reforming of dimethyl ether," *Journal of Power Sources*, vol. 164, no. 1, pp. 73-79, 2007.
- [65] J-H. Koh, B-S. Kang, H. C. Lim, and Y-S. Yoo, "Thermodynamic Analysis of Carbon Deposition and Electrochemical Oxidation of Methane for SOFC Anodes," *Electrochemical and Solid-State Letters*, vol. 4, no. 2, pp. A12-A15, 2001.
- [66] J. M. Smith and H. C. Van Ness, *Introduction to Chemical Engineering Thermodynamics*, 3rd ed. New York, USA: McGraw-Hill, 1975.
- [67] M. W. Chase, *NIST-JANAF Thermochemical Tables*, 4th ed. Washington, USA: American Chemical Society, 1998.
- [68] MathWorks Inc., *MATLAB version 7.5*. Natick, Massachusetts, USA, 2007.
- [69] X. Li, *Principles of Fuel Cells*. New York, USA: Taylor & Francis Group, 2006.

- [70] R-Y. Chein, Y-C. Chen, C-S. Chang, and J-N. Chung, "Numerical modeling of hydrogen production from ammonia decomposition for fuel cell applications," *Intl Journal of Hydrogen Energy*, vol. 35, pp. 589-597, 2010.
- [71] S.H. Chan, C.F. Low, and O.L. Ding, "Energy and exergy analysis of simple solid-oxide fuel-cell power systems," *Journal of Power Sources*, vol. 103, pp. 188-200, 2002.
- [72] S. W. Webb, *Gas Transport In Porous Media*, Clifford K. Ho and S. W Webb, Eds. Netherlands: Springer, 2006.
- [73] R. Suwanwarangkul, E. Croiset, M.W. Fowler, P.L. Douglas, E. Entchev, M.A. Douglas, "Performance comparison of Fick's, dusty-gas and Stefan-Maxwell models to predict the concentration overpotential of the a SOFC anode," *Journal of Power Sources*, vol. 122, pp. 9-18, 2003.
- [74] V. Janardhanan, "A detailed approach to model transport, heterogeneous chemistry, and electrochemistry inside solid-oxide fuel cells," Universität Karlsruhe, Karlsruhe, PhD Thesis ISBN: 978-3-86644-184-2, 2007.
- [75] R.B. Bird, W.E. Stewart, and E.N. Lightfoot, *Transport Phenomena*, 2nd ed. New York: John Wiley & Sons Inc., 2002.
- [76] R.C. Reid, J.M. Prausnitz, and B.E. Poling, *The properties of gases and liquids*, 5th ed. New York: McGraw-Hill Company, 2004.
- [77] H. Zhu, R.J. Kee, V.M. Janardhanan, O. Deutschmann, and D.G. Goodwin, "Modeling elementary heterogeneous chemistry and electrochemistry in solid-oxide fuel cells," *Journal of Electrochemical Society*, vol. 152, no. 12, pp. A2427-A2440, 2005.
- [78] N.J. Themelis, *Transport and Chemical Rate Phenomena*, 1st ed.: Gordon and Breach Publishers, 2005.
- [79] H. Zhu and R.J. Kee, "A general mathematical model for analyzing the performance of fuel-cell membrane-electrode assemblies," *Journal of Power Sources*, vol. 117, no. 1-2, pp. 61-74, 2003.
- [80] Y. Patcharavorachot, W. Paengjuntuek, S. Assabumrungrat, and A. Arpornwichanop, "Performance evaluation of combined solid oxide fuel cells with different electrolytes," *International Journal of Hydrogen Energy*, vol. 35, pp. 4301-4310, 2010.
- [81] J. de Swaan Arons, H. van der Kooi, and K. Sankaranarayanan, *Efficiency and Sustainability in the Energy and Chemical Industries*, 1st ed.: CRC Press, 2004.

- [82] F-Chart Software, *Engineering Equation Solver V8.629*. USA, 2010.
- [83] F. Krieth and M.S. Bohn, *Principles of Heat Transfer*, 6th ed. Pacific Grove, USA: Brooks/Cole, 2001.
- [84] *Ullmann's Encyclopedia of Industrial Chemistry*.: Wiley-VCH, 2007.
- [85] P. Vernoux, J. Guindet, and M. Kleitz, "Gradual Internal Methane Reforming in Intermediate-Temperature Solid-Oxide Fuel Cells," *Journal of Electrochemical Society*, vol. 145, no. 10, pp. 3487-3492, October 1998.
- [86] J.M. Klein, Y. Bultel, S. Georges, and M. Pons, "Modeling of a SOFC fuelled by methane: From direct internal reforming to gradual reforming," *Chemical Engineering Science*, vol. 62, pp. 1636-1649, 2007.
- [87] A.V. Akkaya, "Electrochemical model for performance analysis of a tubular SOFC," *International Journal of Energy Research*, vol. 31, pp. 79-98, 2007.
- [88] C. Bo, C. Yuan, X. Zhao, C-B. Wu, and M-Q. Li, "Parametric analysis of solid oxide fuel cell," *Clean Technologies and Environmental Policy*, vol. 11, pp. 391-399, 2009.
- [89] P.W. Li and M.K. Chyu, "Electrochemical and Transport Phenomena in Solid Oxide Fuel Cells," *Journal of Heat Transfer*, vol. 127, no. 12, pp. 1344-1362, 2005.
- [90] A. Ringuede, D. Bronine, and J.R. Frade, "Assessment of Ni/YSZ anodes prepared by combustion synthesis," *Solid State Ionics*, vol. 146, pp. 219-224, 2002.
- [91] F. Chen, P. Wang, O.T. Sørensen, G. Meng, and D. Penga, "Preparation of Nd-doped BaCeO₃ proton-conducting ceramics by homogeneous oxalate coprecipitation," *Journal of Materials Chemistry*, vol. 7, no. 8, pp. 1533-1539, 1997.
- [92] X.J. Chen, K.A. Khor, S.H. Chan, and L.G. Yu, "Influence of microstructure on the ionic conductivity of yttria-stabilized zirconia electrolyte," *Materials Science and Engineering*, vol. A335, pp. 246-252, 2002.
- [93] British Petroleum, "Guide to Adblue," [Online].
http://www.bp.com/liveassets/bp_internet/bp_efs/bp_efs_uk/STAGING/local_assets/downloads_pdfs/g/Guide_to_AdBlue.pdf (Accessed: November 2010).